

Biologically Inspired PRINT Particles:
Design, Fabrication, in vitro and in vivo Evaluations of Extremely Soft Particles

Timothy James Merkel

A dissertation submitted to the faculty of the University of North Carolina at Chapel Hill in
partial fulfillment of the requirements for the degree of Doctor of Philosophy in the
Department of Chemistry (Polymers and Materials).

Chapel Hill
2011

Approved by

Joseph M. DeSimone

Wei You

Ed Samulski

William Zamboni

Moo Cho

© 2011
Timothy James Merkel
ALL RIGHTS RESERVED

Abstract
Timothy James Merkel
Biologically Inspired PRINT Particles:
Design, Fabrication, *in vitro* and *in vivo* Evaluations of Extremely Soft Particles
(Under the direction of Joseph M. DeSimone)

This work utilized PRINT (particle replication in non-wetting templates) technology to fabricate extremely soft, biologically inspired particles. Using soft biological systems like cancer cells and red blood cells as an inspiration, hydrogels were designed with cell-like deformability. Preliminary studies, which utilized porogens added to otherwise highly crosslinked hydrogels, resulted in deformable, but rapidly cleared particles due to insufficient particle flexibility.

A loosely crosslinked hydrogel system was developed and evaluated in bulk samples to determine the elastic modulus, and to closely match it to that of RBCs. Microfluidic models of vascular constriction were designed and fabricated in order to test *in vitro* the ability of particles to deform. RBC-sized particles (RBCMs) were fabricated from hydrogels having a range of modulus similar to that of RBCs. An intravital imaging technique allowed for direct observation of particles in the peripheral vasculature. Pharmacokinetic analysis of particle elimination showed an 8-fold decrease in particle modulus resulted in an over 30-fold increase in the elimination phase half-life for these particles. More deformable particles bypassed filtration in the lungs and elsewhere, resulting in extended circulation times. Novel hydrogel monomers were synthesized and used to fabricate low modulus particles with varying sizes to further probe the role of modulus on *in vivo* behavior. These particles

avoided physical filtration in the circulation as a result of their ability to deform. These results demonstrated the critical nature of modulus as a design parameter for microparticles.

As an application for such porous and long-circulating microgels, low modulus cationic RBCMs were tested for their ability to bind to, and affect the triggered release of, small nucleic acids. These particles may be able to capture and protect transiently available microRNA (miRNA) biomarkers for cancer from the circulation, potentiating the identification of novel biomarkers and early detection of the disease.

To my parents, family and friends for their continuing support

Acknowledgements

There are so many people who have contributed to my work over the years in one way or another, and all deserve my heartfelt thanks. First and foremost, I would like to thank my advisor, Joseph DeSimone, for guiding me and believing in me long enough to make it work. Being a member of his research group has been a great experience full of opportunities. Few grad students will likely be interviewed and filmed as much as I have, whether for an ACC commercial touting student athletes (as an extra) or to promote our work for the media, both domestic and foreign. Serving as a teaching assistant for the entrepreneurship class with Joe and Dr. Lowry Caudill was a treat; thank you gentlemen, I will use the lessons I learned there for the rest of my life.

I owe many thanks to my collaborators in the DeSimone lab, both current and former members: Kai Chen has been a great help and will further these projects when I leave; I know he'll be a superstar. To Dr. Kevin Herlihy; thank you for showing me how it's done and supporting me in reviving our MRS chapter. Dr. Farrell Kersey and Stephen Jones were integral to my research; thank you for your help. I owe Dr. Mary Napier many thanks for her helpful discussions and crucial grant proposals! For his hard work and for letting me help him with some of his brilliant ideas, I thank Dr. Yapei Wang. I hope that we collaborate when we run our respective research labs! I thank Dr. Ji Guo, who helped me dive headfirst into the first long leg of my research and Dr. Stephanie Barrett, for providing guidance and conversation when I needed each of them. To Ryan Orgel, thank you for putting up with me as your mentor, I hope to get some free medical care out of the deal. To the rest of the lab –

Dr. Janine Nunes, Dr. Stuart Williams, Dr. Elizabeth Enlow, Dr. Matthew Parrott, Dr. Hanjin Zhang, Dr. J. Christopher Luft, Dr. Rob Petros, James Byrne, Jing Xu, William Hinson, Dr. Merve Ertas, Stuart Dunn, Dr. Doug Betts, Dr. Andy Wang, Kevin Chu, Tammy Shen, Dr. Jin Wang, Bill Wagner and others - I thank you for your support, your patience and your help and hope that I haven't forgotten anyone.

I owe many thanks to my collaborators outside of the DeSimone lab as well. I offer my thanks to Helen Zha for all of her questions. Our technologies may have been incompatible, but I learned a lot in the process of making that discovery. To Holger Mißlitz; thanks for your patience with us. I hope you have the opportunity to finish what we started. I owe thanks to Dr. Adam Shields, who taught me about microfluidics. Thanks to Jeremy Niskala for all the discussions about science; they really got my creative juices flowing. Thanks to Devin Barrett- it was a pleasure working with you. Thanks to Lloyd Frick for pointing me in the right direction for pk analysis and to Huali Wu, Dr. Bill Zamboni continuing my education in this area. Many thanks to Charlene Ross and the UNC animal handling core for enabling our research. To the officers of the UNC chapter of the materials research society; thank you all for your support and help in setting up a great organization. My thanks to Dr. Wei You for selecting me to help with the 2010 NGRP conference; it was an honor.

Finally, I would like to thank my family and friends for their support through this journey. Particular thanks go to Jeremy Niskala, Dale Wilger, Austin Smith, Jason Johnson, and Kevin Lilley. Thanks to Sam Price and Tim Martin for occasionally reminding me of the location of the SRC. I would also like to thank my brothers Andy and Ben for keeping me grounded and inspired and my sisters Cherie and Sue for joining the family. Thanks to my

parents, Ed and Carol, for their support and understanding. Thanks to Lucy, for making us laugh. Lastly and most importantly, I thank my fiancé and best-friend, Jennifer McGinnis, for her love and support.

Table of Contents

List of Tables.....	xiv
List of Figures.....	xvi
List of Abbreviations and symbols.....	xxiii
Chapter 1 The Biomechanics of Soft Tissues.....	1
1.1 The Mechanics of Biology.....	2
1.2 Cellular Response to Environment.....	2
1.3 Mechanics of Disease.....	4
1.4 Methods for Measuring Elasticity.....	6
1.5 Conclusions.....	8
1.6 Figures.....	8
1.7 References.....	10
Chapter 2 Towards Synthetic Red Blood Cells: Using Mechano-biological Mimicry to Extend Circulation Times of Hydrogel Microparticles.....	14
2.1 Introduction.....	15
2.2 Results and Discussion.....	19
2.2.1 Early Designs of Deformable PRINT RBC Mimic Particles.....	19
2.2.2 HEA-Based Red Blood Cell Mimics.....	26
2.2.3 Conclusions and Future Work.....	37

2.3 Materials and Methods.....	40
2.3.1 Materials.....	40
2.3.2 Fabrication of Master Templates.....	42
2.3.3 Fabrication of Thick PRINT Molds.....	44
2.3.4 Fabrication of “Thin” PRINT Molds.....	44
2.3.5 Particle Fabrication.....	45
2.3.6 Ice Harvesting of Particles.....	46
2.3.7 Particle Purification.....	47
2.3.8 Particle Characterization.....	47
2.3.9. Surface modification of particles.....	48
2.3.10 Humidity Control.....	48
2.3.11 Modulus Testing.....	49
2.3.12 Radiolabeling of Particles with I^{125}	50
2.3.13 Measuring Particle Filtration Times.....	51
2.3.14 Microfluidics.....	51
2.3.15 Intravital Microscopy.....	52
2.3.16 Compartmental Analysis.....	53
2.3.17 Biodistribution.....	56
2.3.18 Evaluation of 1% RBCMs at Long Times.....	56
2.3.19 Histology.....	57
2.3.20 Assessment of Biocompatibility and Interaction with Endothelial Cells.....	58

2.4 Figures.....	61
2.5 References.....	80
Chapter 3 Pharmacokinetics and Biodistribution of Low Modulus Hydrogel Particles.....	84
3.1 Introduction.....	85
3.2 Results and Discussion.....	88
3.2.1 Hydroxy PEG Acrylate Monomers.....	88
3.2.2 Low Modulus HP ₃ A Hydrogels.....	90
3.2.3 Fabrication and Characterization of HP ₃ A Hydrogel PRINT particles.....	91
3.2.4 <i>In vivo</i> Studies.....	92
3.2.5 Pharmacokinetics of Particle Clearance from Blood.....	94
3.3 Conclusions and Future Work.....	96
3.4 Materials and Methods.....	98
3.4.1 Materials.....	98
3.4.2 Synthesis of Hydroxy PEG Acrylate Monomers.....	98
3.4.3 Purification of HPA Monomers.....	99
3.4.4 Modulus Testing.....	100
3.4.5 Particle Fabrication.....	101
3.4.6 Particle Harvesting and Purification.....	102
3.4.7 Particle Characterization.....	103
3.4.8 <i>In vivo</i> Studies.....	104
3.4.9 Biodistribution.....	104

3.4.10 Pharmacokinetics of Particle Clearance from Blood.....	105
3.5 Figures.....	106
3.6 References.....	112
Chapter 4 Cationic Microgel Particles for Identification of Cancer Biomarkers.....	115
4.1 Introduction to miRNA as Cancer Biomarkers.....	116
4.2 Results and Discussion.....	117
4.2.1 Low Modulus Cationic Hydrogels.....	117
4.2.2 Fabrication of Cationic Red Blood Cell Mimicking PRINT Particles.....	118
4.2.3 Binding Capacity.....	119
4.2.4 Binding and Release of miRNA from Cationic Microgels.....	120
4.3 Conclusions and Future Work.....	121
4.4 Materials and Methods.....	123
4.4.1 Materials.....	123
4.4.2 Modulus Testing.....	123
4.4.2 Particle Fabrication.....	124
4.4.3 Particle Purification.....	125
4.4.4 Surface Modification.....	125
4.4.4 Surface Modification.....	125
4.4.6 Binding and Release of miRNA.....	126
4.5 Figures.....	127
4.6 References.....	129
Chapter 5 Summary and Future Directions.....	131

5.1 Summary.....	132
5.1.1 Mechano-biological Mimicry of Red Blood Cells.....	133
5.1.2 Pharmacokinetics and Biodistribution of Low Modulus Hydrogel Particles.....	135
5.1.3 Cationic Microgel Particles for Identification of Cancer Biomarkers.....	135
5.2 Future Directions.....	136
5.2.1 Biodistribution Maps of Soft Particles.....	136
5.2.2 Methods for Determination of Particle Modulus.....	137
5.2.3 Hemoglobin Carriers for Oxygen Transport.....	139
5.2.4 Membranous Particles.....	142
5.3 Figures.....	146
5.4 References.....	151

List of Tables

Table 1.1	Young's modulus values for various cells, viral particles, tissues and soft materials, with source and testing method listed where available.....	3
Table 2.1	The composition of 7 μ m disc PRINT particles used for preliminary in vivo studies.....	22
Table 2.2	Modulus values for bulk samples of the materials used for the particles in the mouse study.....	24
Table 2.3	Mechanical properties of 2-hydroxyethyl acrylate hydrogels with varying length and weight percentage of poly (ethylene glycol) diacrylate (PEG-DA) crosslinker. Hydrogels were prepared in two cases as 25% solutions in water, increasing the flexibility of the gels. Swelling percentage represents the % increase in area of the coupons after 24 hours of soaking in water. Error represents one standard deviation, with n=3.....	28
Table 2.4	The composition of HEA hydrogels intended for <i>in vivo</i> use as RBCMs. The polymerizable dye for bulk samples was fluorescein-o-acrylate; for RBCM particles, the fluorescein-o-acrylate was replaced by Dylight ₆₈₀ maleimide.....	29
Table 2.5	Modulus values and compartmental analysis of RBCM particles from intravital microscopy experiments. Ranges given represent one standard deviation. Values were derived from scans of three mice.....	29
Table 2.6	Physical characteristics of RBCM particles and mouse RBCs. Error represents one standard deviation from the mean with n=50 for particle diameters, and n=16 for zeta potential measurements.....	30
Table 2.7	Pharmacokinetic parameters for 1% crosslinked RBCMs calculated from blood draws taken out to 5 days post-injection.....	35

Table 3.1	Properties of lightly crosslinked hydrogels composed of different acrylic monomers containing 1% of a 4,000 g/mol PEG diacrylate crosslinker and 1% of HCPK photoinitiator, hydrated for 12 hours in deionized water at room temperature. Monomers are shown with increasing PEG chain length.....	89
Table 3.2	Mechanical properties of hydroxyl PEG ₃ Acrylate (HP ₃ A) hydrogels with varying amounts of PEG ₄₀₀₀ diacrylate crosslinker and 10% of 2-carboxyethyl acrylate. Swelling ratios were determined from one bulk sample hydrated for 24 hours in PBS. Modulus and strain at break represent an average value determined from three samples cut from the bulk gel, with error representing one standard deviation.....	91
Table 3.3	The composition of hydrogel particles fabricated for <i>in vivo</i> work.....	91
Table 3.4	Characterization of particles fabricated for <i>in vivo</i> studies. Particle diameters were determined by microscopy. Error represents one standard deviation from the mean with n=50 for particle diameters.....	92
Table 3.5	Pharmacokinetic parameters for low modulus hydrogel PRINT particles with increasing diameters. Parameters were determined from particle concentration in whole blood at times 0.2 -104 hours post-dose using a standard two-compartment model according to the equation $C = Ae^{-\alpha t} + Be^{-\beta t}$ where C is the concentration of particles in blood and t is time post-dose.....	95
Table 4.1	Young's modulus values for cationic hydrogels with varied crosslink density, charge density, and amount of porogen added.....	118
Table 4.2	Zeta potential of cationic red blood cell mimicking microgels with varying PEG chain length used for surface modification.....	119

List of Figures

Figure 1.1	Schematic representations of different techniques used to measure the mechanical properties of cells. (A) Atomic force microscopy (AFM) and (B) magnetic twisting cytometry (MTC) are methods that probe local areas of cells at a force resolution of 10^{-10} and 10^{-12} N, respectively, and a displacement resolution of at least 1 nm. (C) Micropipette aspiration (MA) and (D) optical trapping deform an entire cell at a force resolution of 10^{-10} and 10^{-11} , respectively. This figure was adapted from reference 45.....	9
Figure 2.1	Scanning electron microscope images of 7 μ m disc PRINT particles made from (A) 89% PEG ₄₂₈ triacrylate, 10% mPEG ₁₀₀₀ methacrylate and 1% DEAP photoinitiator and (B) 89% PEG ₄₂₈ triacrylate, 10% mPEG ₁₀₀₀ methacrylate and 1% DEAP photoinitiator mixed 1:1, by weight, with PEG ₅₅₀ dimethyl ether as a porogen. The addition of porogen increases particle flexibility.....	61
Figure 2.2	SEM images of 7 μ m diameter, discoid PRINT particles with varying amounts of 550 g/mol molecular weight poly (ethylene glycol) added to the pre-particle solution as a porogen. The particles appear increasingly flexible, porous, and fragile as porogen content increases as follows: (A) 0 %, (B) 50 %, (C) 60 %, (D) 75 % and (E,F) 90 % porogen.....	62
Figure 2.3	Measuring particle deformability by filtration times through a track-etched membrane. (A) A graphic showing the filtration set-up, with one port directed towards mild vacuum and a second port directed to the membrane apparatus. The cut-away depicts particles passing through the membrane. (B) A bright field microscope image of rigid particles (“No porogen”) on the membrane after filtration. Particles are along the sides and bottom of the image, with the membrane and some of the 5 μ m pores visible in the center of the image. The scale bar is 20 μ m. (C) Filtration times for 5 mL of particle or control solutions through a 5 μ m nucleopore track etch membrane. Each plot represents n=4 with error bars as one standard deviation.....	63
Figure 2.4	SEM images of 7 μ m diameter, discoid PRINT particles with varying deformability used in preliminary <i>in vivo</i> studies. Rigid particles (A) contain no porogen while moderately deformable ones (B) were made with 50% (by weight) of a non reactive PEG porogen. The most deformable particles (C) were made primarily with a PEG diacrylate monomer in lieu of the triacrylate used in A and B, and included 50% porogen as in B.....	64

- Figure 2.5** Biodistribution of 7 μm diameter RBC mimic PRINT particles in mice as a function of % injected dose. Deformability of the hydrogel particles increases from A to C with the addition of a porogen in series B and replacement of triacrylate monomer with diacrylate in addition to porogen for series C. Particle accumulation in the tail is typical of tail vein injection procedures. Major accumulation occurred in the lungs in all cases along with poor persistence in the blood, suggesting that no formulation was deformable enough to navigate the narrow capillaries found in this organ.....65
- Figure 2.6** RBCM particles. (A) A graphical depiction of the PRINT process used to fabricate RBCMs. Briefly, from top to bottom, an elastomeric fluoropolymer mold (green) with disc shaped wells was covered by an aliquot of the pre-polymer mixture (red). The mold was passed through a pressured nip (black) covered by a high energy sheet (grey), wicking away excess liquid from the mold surface while filling the wells of the mold. The filled mold was cured photochemically, yielding cross-linked hydrogel particles, which were harvested from the mold by freezing onto a thin film of 1% poly (vinyl alcohol) in water (blue) and peeling away the mold. Melting of this layer resulted in a suspension of red blood cell mimic (RBCM) hydrogel particles. (B-E) Fluorescent images of hydrated RBCMs with varying % crosslinker (B) 10% crosslinked (C) 5% crosslinked (D) 2% crosslinked and (E) 1% crosslinked. Scale bars are 20 μm66
- Figure 2.7** Modulus of hydrated samples of hydrogel as % crosslinker was varied from 1-10%. Additional dye (1% fluorescein-o-acrylate) was included to show the effect the addition of a near-IR dye to the composition for in vivo imaging applications.....67
- Figure 2.8** Discoid master templates fabricated in SU-8 on six inch silicon wafers. Discs with diameters of (A) 1.5 μm , (B) 2 μm , (C) 3 μm , (D) 4 μm , (E) 5 μm , and (F) 6 μm were prepared with an aspect ratio of 0.3. The scanning electron microscope images are shown at approximately the same scale and represent embossed films of cyanoacrylate cast from PRINT molds made using the appropriate masters.....68
- Figure 2.9** The dose dependant cell viability of HUVEC (endothelial) cells when dosed with HEA-based RBCMs with varied crosslink density (1-10%) after 72 hours of incubation with the particles as determined by MTS (A) and ATP/luciferase

	(B) assays as a percent of saline-dosed control.....	69
Figure 2.10	Uptake of 1, 2, 5, and 10% crosslinked RBCMs in HUVEC cells after dosing times from 15 minutes to 24 hours based on flow cytometry. Results are expressed in terms of the percentage of cells which had taken up RBCMs (internalized) and which were free of RBCMs (unassociated).....	70
Figure 2.11	Microfluidic evaluation of RBCM deformability. (A) A schematic of the microfluidic devices. The channel has a repeating pattern of 50 μm long pores which are 3 μm wide and 3.5 μm tall, forcing particles passed through the device to deform. Flow was driven by a syringe pump. (B) An image sequence showing a 1% crosslinked RBCM (6.0 μm diameter) deforming to pass through a 3 x 3.5 μm channel (25 ms between frames). (C) 10% crosslinked RBCMs stuck in the entrance of the 3 μm pores in a microfluidic device. Scale bars are 30 μm	71
Figure 2.12	Intravital microscopy data and compartmental analysis. (A) Vasculature highlighted with rhodamine B labeled dextran prior to injection of RBCMs. (B) Dylight 680 labeled 1% cross-linked RBCMs flowing through this stretch of vasculature 20 minutes after dosing, with ROI outlined in yellow. (C) Colored overlay of A and B, with dextran in blue and particles shown in red. Scale bars are 100 μm . (D) Two-compartment model schematic and governing equations for the model applied to the data. (E) Decrease in fluorescent signal in the ROI for the 2 hour scan in this mouse. The semi-log plot shows calculated fit for the two compartment pharmacokinetic models.....	72
Figure 2.13	A standard curve which correlates fluorescent efficiency (signal intensity) and concentration of 1% crosslinked RBCMs in whole blood. Deviation from linearity defines the lower limit of quantification for fluorescent signal. Data collected for the blood draw experiments fell within the linear range of this plot. Scale bars represent one standard deviation, with n=3.....	73
Figure 2.14	A plot of particle concentration in whole blood over time for 1% crosslinked RBCMs where n=4 for each data point. A two compartment pharmacokinetic model with elimination from the central compartment was fit to the data (red) by nonlinear regression analysis. The fit was used to calculate pharmacokinetic parameters for these particles. Scale bars represent one standard deviation, with n=3.....	74

Figure 2.15	Biodistribution of RBCMs. (A) Distribution of RBCMs into various tissues 2 hours post dosing by percent recovered fluorescence normalized for tissue weight. Error bars represent one standard deviation, with n=3 for each case. (B) Lung tissue from a mouse dosed with 10% cross-linked RBCMs. Particles are shown in red, with cell nuclei in purple and cytoskeleton (F-actin) stained green. (C) Lung tissue from a mouse dosed with 1% cross-linked RBCMs, with tissue stained as in (B). Very few RBCMs were in this tissue compared to mice dosed with more rigid particles, consistent with the tissue distribution data. Scale bars are 50 μm	75
Figure 2.16	A plot showing the biodistribution of 1% crosslinked RBCMs in mice over a 2-120 hour time course in the liver, lung, spleen and kidneys. Data is presented as fluorescent efficiency per gram of tissue weight. Error bars represent one standard deviation, with n=3 for each case.....	76
Figure 2.17	Histological analysis of spleen tissue from RBCM dosed mice. (A) Overlaid image of immunostained spleen tissue from a mouse dosed with 2% cross-linked RBCMs. The particles (red) are primarily sequestered in the red pulp, an area of tissue which is rich in macrophages (green). Cell nuclei are shown in purple. (B) An enlarged view of the area indicated in (A) by a grey square.....	77
Figure 2.18	Left: A chrome on quartz reticle designed for fabrication of master templates with micron sized discoid features. Right: Bright field microscopy images of the patterned sections of the reticle at 100x magnification (scale bar is 20 μm).....	78
Figure 2.19	A plot showing SU-8 film thickness as a function of weight percent solids of SU-8 2010 when diluted from the original 58% solids with SU-8 thinner. Film were spin coated at 3000 rpm for 30 seconds. Thickness measurements were made based on post-exposure feature heights.....	79
Figure 3.1	Synthetic scheme for hydroxyl PEG acrylates (HPAs). The structure of the monoacrylated products are shown below the reaction scheme, along with the naming convention.....	106
Figure 3.2	Fluorescent images of the particles used for the in vivo studies. The particles have hydrated diameters of (A) $3.79 \pm 0.17 \mu\text{m}$, (B) $6.39 \pm 0.56 \mu\text{m}$, and (C) $8.88 \pm 0.47 \mu\text{m}$	107

Figure 3.4	Biodistribution of extremely deformable particles of different sizes in mice over the course of several days. These semi-log plots show the percent of fluorescent signal normalized per gram of tissue weight. Four mice were examined per time-point, with error bars representing one standard deviation.....	108
Figure 3.5	Biodistribution of low modulus hydrogel particles of different sizes in mice in terms of total fluorescence signal (fluorescence efficiency) in each tissue. Fluorescence in blood was measured in 100 μ L aliquots and adjusted to account for the total blood volume of each mouse. Four mice were measured per time point. Error bars represent one standard deviation.....	109
Figure 3.6	A plot showing the change in particle concentration in blood over time for particles of different sizes. Particles with a diameter of 6.4 μ m, similar to that of mouse red blood cells, were cleared more slowly than both larger and smaller particles with identical mechanical properties and composition. The concentration of the largest particles, with a diameter of 8.8 μ m, fell to below the lower limits of quantification after 7 hours post-injection.....	110
Figure 3.7	SEM images of 200 nm particles made from 1% PEG ₄₀₀₀ DA crosslinked HP ₃ A. The particles are on a harvesting film after transfer from the mold. A scratch in the harvesting film (top right corner of both images) illuminates the deformability of these particles where they were disturbed as the scratch was made.....	111
Figure 4.1	Cationic hydrogel particles (A) Particles fluoresce in the green channel due to matrix bound fluorescein dye. (B) Fluorescence in the red channel from adsorbed Cy3 dye-conjugated DNA 20mer. Particles were incubated at 37 °C for one hour with 1 μ M DNA, then washed 3 times to remove unassociated DNA. Scale bars are 20 μ m.....	127

Figure 4.2	Analysis of miRNAs bound to and released from CRBCM particles. Lanes 1-3 are miRNA 96 in increasing amounts (100, 200 and 300 ng). Lane 4 is miRNA 96 desorbed from CRBCs in high salt concentration, causing band broadening. Lane 5 was loaded with miRNA 96 after degradation with and RNase cocktail. Ethidium bromide was not sufficient to stain the degraded RNA. Lanes 6-10 were identical to 1-5, respectively, but with miRNA 100 in place of miRNA 96.....	128
Figure 5.1	A plot showing the diameter and modulus of low aspect ratio particles examined in this dissertation. The grey oval indicates the particles which demonstrated longer circulation times as a result of avoidance of physical filtration mechanisms in the circulation. The green box indicates the combination of particle diameters and moduli which should be the target of future studies.....	146
Figure 5.2	A schematic representation of atomic force microscopy (AFM) being used to probe the mechanical properties of a PRINT particle. A known force is applied by the AFM to the particle, causing a deformation in the particle. The movement of the cantilever is tracked by the movement of a laser on a photodiode detector as it reflects from the top of the cantilever. Deformations must be small relative to the thickness of the particle to avoid interference from the substrate.....	147
Figure 5.3	A schematic of the initial attempts at the fabrication of micron sized, self assembled HA/PA membranes. (A) A PRINT mold (green) is filled with HA solution (red) and frozen before bringing into contact with a layer of PA solution (brown). (B) The assembly is frozen on dry ice and, (C) the mold is peeled away, leaving the frozen HA particles on the PA ice surface. (D) The solutions thaw and the HA drops into the PA solution where membrane self-assembly occurs, yielding hollow sacs.....	148
Figure 5.4	Membranes assembled from HA particles cast in 7x7 μm cylinder PRINT molds and harvested to a solution of PA. (A) The particles appeared to assemble into fully formed sacs which were reminiscent of red blood cells. (B) Inspection with a confocal microscope showed that the sacs did not fully close, likely due to incomplete immersion of HA particles into the PA solution. Scale bars are 20 μm	149

Figure 5.5 An image of sacs formed from assembly of HA and PA with a connecting scum layer resulting from incomplete de-wetting of the PRINT mold surface. The bottom left of the image contains collapsed sacs trapped in this scum layer, while the upper right side has more holes in this membrane. The scale bar represents 20 μm150

List of Abbreviations and Symbols

% v/v	Volume percent
°C	Degrees C
μm	Micrometer
μM	Micromolar
¹²⁵ I	Iodine 125
AEM	2-aminoethyl methacrylate hydrochloride salt
AFM	Atomic Force Microscope
AR	Aspect ratio
ATP	Adenosine triphosphate
AUC	Area under the curve
BALB/c	A strain of mouse
CD 47	A human "marker of self" protein
CEA	2-carboxyethyl acrylate
CLT	Total body clearance
CO ₂	Carbon dioxide
Cp	Concentration of particles in plasma
CRBCM	Cationic red blood cell mimicks
Cy3	Cyanine dye 3
DEAP	2,2-diethoxyacetophenone
DMF	Dimethylformamide
DNA	Deoxyribose nucleic acid

DPBS	Dulbecco's phosphate buffered saline
EGDA	Ethyleneglycol diacrylate
EtOH	Ethanol
FBS	Fetal bovine serum
g/mol	Grams per mole
GEM	Genetically engineered mouse
GPa	Gigapascal
HA	Hyaluronic acid
Hb	Hemoglobin
HBOC	Hemoglobin based oxygen carrier
HCl	Hydrochloric acid
HCPK	1-hydroxycyclohexyl phenyl ketone
HEA	2-hydroxyethylacrylate
HIV	Human immunodeficiency virus
HPA	HydroxyPEG acrylate
ICP-MS	Inductively coupled plasma mass spectrometry
ipa	Isopropanol
IR	Infrared
kCl	Potassium chloride
kDa	Kilodalton
kPa	Kilopascal
LbL	Layer-by-layer
MA	Micropipette aspiration

mCi/mL	Millicurie per milliliter
MgSO ₄	Magnesium sulfate
miRNA	Micro ribose nucleic acids
MPa	Megapascal
mPEG	Methoxy terminated poly(ethylene glycol)
MS	Microplate stretching
MTC	Magnetic twisting cytometry
mV	Millivolt
N	Newton
NaCl	Sodium chloride
nm	Nanometer
OT	Optical tweezers
PA	Peptide amphiphile
PBS	Phosphate buffered saline
PEG	Poly(ethylene glycol)
PEGDA	Poly(ethylene glycol) diacrylate
PET	Poly(ethylene teraphthalate)
PFPE	Perfluoropolyether
PRINT	Particle replication in non-wetting templates
psi	Pounds per square inch
PVOH	Poly(vinyl alcohol)
qRT-PCR	Quantitative reverse transcription polymerase chain reaction
RBC	Red blood cell

RBCM	Red blood cell mimic
RNA	Ribose nucleic acid
RNase	Ribonuclease
rpm	Rotations per minute
SEM	Scanning electron microscopy
SU-8	A negative photoresist
$t_{1/2}$	Half-life
TB	Trypan blue
TBS	Tris buffered Saline
Tff	Tangential flow filtration
TGA	Thermogravimetric analysis
UV	Ultraviolet
$V_3A_3K_3$	A polypeptide with 3 valine, 3 Alanine, and 3 Lysine amino acids
V_c	Volume of the central compartment
$V_{d\beta}$	Volume of distribution in the beta phase
α	Alpha
β	Beta

Chapter 1

The Biomechanics of Soft Tissues

1.1 The Mechanics of Biology

Biomechanics seeks to understand the workings of biological systems through the mechanical properties of the component materials. Natural materials display a wealth of structures and structure dependant properties which are essential to their specific functions. Tissues in the body possess a range of mechanical properties (**Table 1.1**); with elastic moduli ranging from stiff calcified bone (5-13 GPa)^{1,2} to softer materials like pre-calcified bone (> 30 kPa)^{3,4}, red blood cells (26 kPa)⁵, skin and muscle cells (around 10 kPa) and extremely soft brain tissue (about 0.5 kPa)⁴. With advances in nanotechnology allowing for closer scrutiny of the structure and properties at the cellular and sub-cellular levels, the links between biomechanics and human disease has developed as a subject of intense scrutiny. Indeed, as we grow more advanced and versatile in our ability to design and fabricate new materials for biological applications, we are increasingly looking towards the soft materials found in nature for inspiration and guidance.

1.2 Cellular Response to Environment

An essential consideration in designing materials for biological applications lies in understanding how the mechanical properties of a biomaterial will enable a desired biological response. Circulating cells are extremely soft; the mechanical flexibility of red blood cells allows them to avoid filtration in the spleen, one of several factors resulting in long circulation times for these abundant cells⁴. The mechanical properties of a local environment may influence the biological response of cells as much or more than chemical stimuli. The differentiation of stem cells⁶, the proliferation of fibroblasts⁷, and cell death⁸ are highly influenced by the geometry of the cellular microenvironment. Similarly, substrate mechanical properties can influence cell and tissue behavior³. For example, mesenchymal

	Source	Testing method	Elastic modulus (kPa)	Ref
Bone	Human	Nanoindentation	13.5×10^9	2
Tobacco mosaic virus	Virus	AFM	6×10^6	9
HIV (immature)	Virus	AFM	9.3×10^5	10
Achilles' tendon	Rat	Tension	3.1×10^5	11
HIV (mature)	Virus	AFM	1.2×10^5	10
<i>E. coli</i> DH5 alpha	Bacteria	AFM	$1.9 - 3.0 \times 10^3$	12
Articular cartilage	Bovine	Compression	9.5×10^2	13
Skeletal muscle	Rat	Tension	1.0×10^2	14
Carotid artery	Mouse	Perfusion	90	15
Spinal cord	Human	Tension	89	16
Thyroid cancer ^a	Human	Compression	45	16
Pre-mineralized bone	-	-	30	3
Poly(dimethyl siloxane)	Synthetic	-	10-1000	3
Polyacrylamide	Synthetic	-	0.1-100	3
Spinal cord	Rat	Tension	27	17
Red blood cells	Human	AFM	26	5
Cardiac muscle	Mouse	Tension	20–150	18
Skeletal muscle	Mouse	AFM	12	19
Thyroid	Human	Compression	9	20
Lung	Guinea pig	Tension	5–6	21
Breast tumor ^b	Human	Compression	4	22
Alginate	Algae	-	0.1-150	3
Hyaluronic acid	Various	-	0.1-150	3
Collagen	Various	-	0.001-1	3
Fibronectin	Various	-	0.001-1	3
Matrigel	Mouse	-	<1	3
Lung cells (normal)	Human	AFM	2.1	23
Lung cancer cell ^c	Human	AFM	0.56	23
Kidney	Swine	Rheology	2.5	24
Premalignant breast	Human	Indentation	2.2	16
Fibrotic liver	Human	Compression	1.6	25
Liver	Human	Compression	0.640	25
Lymph containing metastases	Human	Vibrational resonance	0.330	26
Brain	Swine	Indentation	0.260–0.490	27
Lymph node	Human	Vibrational resonance	0.120	26

^a Thyroid papillary adenocarcinoma. ^b Mammary ductal carcinoma. ^c Non-small cell carcinoma

Table 1.1. Young's modulus values for various cells, viral particles, tissues and soft materials, with source and testing method listed where available.

stem cells cultured on polyacrylamide substrates of different stiffness developed distinctly different morphologies and lineage²⁸. Cells cultured on soft (0.1–1 kPa) substrates developed neuronal cytoskeletal markers while a moderately stiff substrate (8–17 kPa) resembling muscle resulted in the expression of myogenic markers and a stiffer substrate (25–40 kPa)

resembling pre-calcified bone proved osteogenic. In order to differentiate based on the elasticity of a substrate, the stem cells must be able to pull on the matrix and judge the force necessary for a deformation. Because these stem cells egress from their origin in the marrow and engraft in different environments through the body, they must be capable of differentiation based on microenvironmental clues. In light of this issue, it may not be surprising that sensing of the microenvironment was found to be more selective than soluble induction factors in directing stem cell differentiation²⁸.

1.3 Mechanics of Disease

In addition to cellular behavior and differentiation on substrates, the elasticity of individual cells has been given increasing attention due in large part to the increase in the elasticity of cancer cells compared to benign cells of the same type and the possibility that this difference may be translated to better screening methods for the disease^{23,29,30}. This increase in deformability may have several biological consequences which promote the survival and proliferation of these cells. A decrease in cell stiffness may result in reduced recognition by phagocytic cells. Bacteria are much stiffer than most tissues in the body, with elastic moduli from 1.9-3.0 MPa, about 100 times that of red blood cells¹². Virus particles are also orders of magnitude less flexible, with the tobacco mosaic virus (6,000 MPa)⁹ and HIV virus particles (115-930 MPa)¹⁰ extremely stiff compared to commonly circulating cells. Phagocytotic pathways may have evolved to preferentially act on recognition of bacterial shape³¹; it stands to reason that the dramatically increased stiffness of bacterial cells and viral particles may also cause a recognition phenomenon. Phagocytosis of soft, polyacrylamide microparticles was significantly reduced compared to more rigid counterparts³². These softer beads were unable to stimulate the assembly of actin filaments required for the formation and

closure of phagosomes. The addition of a lysophosphatidic acid, an activator of several signaling pathways, resulted in an increase in phagocytosis of soft beads to levels similar to those for the rigid beads. Rigid beads were unaffected by the addition of lysophosphatidic acid, suggesting that the acid activated a pathway usually initiated by rigid substrates. These results suggest that macrophages use substrate rigidity and force input from a surface-bound particle as cues to determine whether the target should be ingested.

The elasticity of cancer cells may enable their proliferation throughout the body. Metastasis describes the process by which cancer cells spread from one organ or tissue to a different part of the body. For metastasis to occur, a cancer cell must first invade a lymphatic or blood vessel by a process called intravasation. Transport through the circulatory system results in lodging of the cancer cells in small blood vessels and subsequent extravasation to the parenchymal tissue lining the vessel wall. Greater elasticity, which has been identified as an indication of disease³³, may allow cancer cells to more readily escape tumor beds and infiltrate the bloodstream in a metastatic process. A decrease in the stiffness of the cell can be directly attributed to changes in the cellular cytoskeleton from which mechanical rigidity is derived. The cytoskeletal components of actin, microtubules, and intermediate filaments work in concert with their accessory proteins to facilitate tasks such as cell motility, mitosis, ribosomal and vesicle transport and mechano-transduction³⁴. The order and structure of these cellular components in the cytoskeleton devolves to a more irregular and compliant state as cells progress from normal to cancerous³⁵. Cancer cells have high motility and replication, both of which are facilitated by a less rigid cytoskeleton. In addition to the decrease in stiffness of cancer cells versus normal cells, several studies have correlated increased metastatic efficiency in multiple cancer cell lines with decreased cell

stiffness^{29,35,36}. Metastatic cancer cells from patients with non-small cell carcinomas of the lungs and breast ductal adenocarcinoma were found to be more than 70% softer than benign cells of the same type using AFM analysis, with elastic moduli on the order of 0.5 kPa²³.

1.4 Methods for Measuring Elasticity

The measurement of elasticity on a cellular level can be difficult due to the low forces and short length scales involved, but a variety of techniques have been developed to probe the mechanical properties of cells (**Figure 1.1**). These techniques can be broadly separated into several categories according to the length scale across which they act on the cell. Atomic force microscopy (AFM) and magnetic twisting cytometry (MTC) mechanically probe the cell surface with forces on the order of $10^{-12} - 10^{-6}$ N and displacements smaller than 1 nm²⁹. In AFM methods, the deformation is localized, induced by the sharp tip at the end of an AFM cantilever, though rounded spherical tips can be used to broaden the deformation area³⁷. The applied force is calculated by calibration of the deflection of the cantilever by reflection of a laser to a photodiode detector. In MTC, a magnetic bead is attached covalently to the cell surface and rotated via the application of a magnetic field. Analysis of the membrane deformation yields information about the elastic and viscoelastic properties of the cell membrane³⁸.

Deformations of large portions of the cell with sub micron displacements are possible using the optical tweezers (OT)³⁹ and micropipette aspiration (MA)⁴⁰ techniques shown in Figure 1.1 as well as other techniques like mechanical microplate stretching (MS)²⁹. For these techniques, forces on the order of $10^{-12} - 10^{-7}$ N are applied and the deformation tracked using optical microscopy. Optical tweezers feature beads covalently attached to a cell

membrane; cells picked for analysis will feature two beads attached to a single cell at opposite sides of the membrane. A laser is aimed at the beads, which are made from a high-refractive index dielectric material. The beads, focused on by individual lasers, are attracted towards the focal point of each laser trap, inducing displacement between them. In MA techniques, suction aspirates a portion of a cell, or the entire cell through a micropipette tip. Analysis of the geometry change then provides the elastic and viscoelastic response of the cell, though adhesion to a substrate and friction between the cell surface and the walls of the micropipette are typically ignored⁴¹. In MS experiments, a cell is covalently bound to two functionalized glass surfaces which are moved or sheared apart with force control and measured displacement determining the mechanical properties of the cell³⁰.

In addition to the above methods for probing the mechanical properties of cells, a wide variety of methods are employed which provide a qualitative measure of deformability rather than quantitatively measuring forces and cellular response. Measurements of the time required populations of cells to pass through micropore filters with distinct pore sizes offers a facile simulation of cell motility through the microvasculature^{42,43}. Microfluidic systems offer more sophisticated models of the vasculature, and can be sized to model flow through restrictions in blood vessels or tissue^{42,44}. These channels are typically fabricated from poly(dimethyl siloxane), glass or silicon with dimensions in the range of 10-100 μm . The device design can vary from narrowing channels to multiple branches designed to replicate the branching of blood vessels to capillaries. Assays can be designed to put a fixed pressure over a channel, or to measure flow characteristics, cell velocity, and cell count passing through such a restricted space, providing insight into the relative flexibility of the cells examined.

1.5 Conclusions

As our ability to measure the stiffness of materials on the length scale of cells has advanced, so too our understanding of the role played by mechanical rigidity and flexibility in biological materials. The picture emerging from these studies describes mechanical flexibility as a component of biology that is equally essential to biological function as chemical factors like molecular signaling, ligand-receptor interactions and protein structure. While our understanding of the interplay between material properties and biological functions is growing, the field remains in an early stage of development, with many questions still unanswered⁴. However, it is clear that the design of biomaterials can be enhanced by consideration of material stiffness.

1.6 Figures

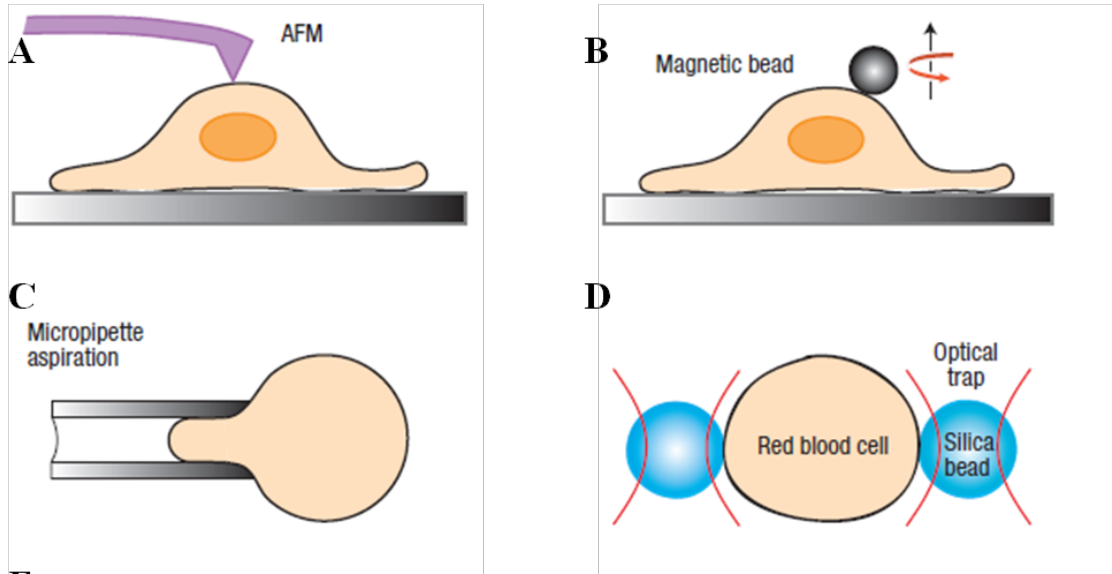


Figure 1.1. Schematic representations of different techniques used to measure the mechanical properties of cells. (A) Atomic force microscopy (AFM) and (B) magnetic twisting cytometry (MTC) are methods that probe local areas of cells at a force resolution of 10^{-10} and 10^{-12} N, respectively, and a displacement resolution of at least 1 nm. (C) Micropipette aspiration (MA) and (D) optical trapping deform an entire cell at a force resolution of 10^{-10} and 10^{-11} , respectively. This figure was adapted from reference ⁴⁵.

1.7 References

- (1) Choi, K.; Kuhn, J. L.; Ciarelli, M. J.; Goldstein, S. A. *J Biomech* **1990**, 23, 1103.
- (2) Rho, J.-Y.; Tsui, T. Y.; Pharr, G. M. *Biomaterials* **1997**, 18, 1325.
- (3) Rehfeldt, F.; Engler, A. J.; Eckhardt, A.; Ahmed, F.; Discher, D. E. *Adv Drug Deliv Rev* **2007**, 59, 1329.
- (4) Mitragotri, S.; Lahann, J. *Nat Mater* **2009**, 8, 15.
- (5) Dulinska, I.; Targosz, M.; Strojny, W.; Lekka, M.; Czuba, P.; Balwierz, W.; Szymonski, M. *J Biochem Biophys Methods* **2006**, 66, 1.
- (6) Graziano, A.; d'Aquino, R.; Cusella-De Angelis, M. G.; De Francesco, F.; Giordano, A.; Laino, G.; Piattelli, A.; Traini, T.; De Rosa, A.; Papaccio, G. *J Cell Physiol* **2008**, 214, 166.
- (7) Milner, K. R.; Siedlecki, C. A. *J Biomed Mater Res A* **2007**, 82, 80.
- (8) Chen, C. S.; Mrksich, M.; Huang, S.; Whitesides, G. M.; Ingber, D. E. *Science* **1997**, 276, 1425.
- (9) Schmatulla, A.; Maghelli, N.; Marti, O. *Journal of Microscopy* **2007**, 225, 264.
- (10) Kol, N.; Shi, Y.; Tsvitov, M.; Barlam, D.; Shneck, R. Z.; Kay, M. S.; Rousso, I. *Biophys J* **2007**, 92, 1777.
- (11) Almeida-Silveira, M. I.; Lambertz, D.; Pérot, C.; Goubel, F. *European Journal of Applied Physiology* **2000**, 81, 252.
- (12) Cerf, A.; Cau, J.-C.; Vieu, C.; Dague, E. *Langmuir* **2009**, 25, 5731.
- (13) Freed, L. E.; Langer, R.; Martin, I.; Pellis, N. R.; Vunjak-Novakovic, G. *Proceedings of the National Academy of Sciences* **1997**, 94, 13885.
- (14) Linder-Ganz, E.; Gefen, A. *Journal of Applied Physiology* **2004**, 96, 2034.

- (15) Guo, X.; Lu, X.; Ren, H.; Levin, E. R.; Kassab, G. S. *American Journal of Physiology - Heart and Circulatory Physiology* **2006**, 290, H1788.
- (16) Levental, I.; Georges, P. C.; Janmey, P. A. *Soft Matter* **2007**, 3, 299.
- (17) Fford, R. J.; Bilston, L. E. *Journal of Biomechanics* **2005**, 38, 1509.
- (18) Wu, Y.; Cazorla, O.; Labeit, D.; Labeit, S.; Granzier, H. *Journal of Molecular and Cellular Cardiology* **2000**, 32, 2151.
- (19) Engler, A. J.; Griffin, M. A.; Sen, S.; Bönnemann, C. G.; Sweeney, H. L.; Discher, D. E. *The Journal of Cell Biology* **2004**, 166, 877.
- (20) Lyshchik, A.; Higashi, T.; Asato, R.; Tanaka, S.; Ito, J.; Hiroka, M.; Brill, A. B.; Saga Togashi, K. *Elastic moduli of thyroid tissues under compression*; Dynamedia: Silver Spring, MD, ETATS-UNIS, 2005; Vol. 27.
- (21) Yuan, H.; Kononov, S.; Cavalcante, F. S. A.; Lutchen, K. R.; Ingenito, E. P.; Suki, B. *Journal of Applied Physiology* **2000**, 89, 3.
- (22) Paszek, M. J.; Zahir, N.; Johnson, K. R.; Lakins, J. N.; Rozenberg, G. I.; Gefen, A.; Reinhart-King, C. A.; Margulies, S. S.; Dembo, M.; Boettiger, D.; Hammer, D. A.; Weaver, V. M. *Cancer cell* **2005**, 8, 241.
- (23) Cross, S. E.; Jin, Y. S.; Rao, J.; Gimzewski, J. K. *Nat Nanotechnol* **2007**, 2, 780.
- (24) Nasseri, S.; Bilston, L. E.; Phan-Thien, N. *Rheologica Acta* **2002**, 41, 180.
- (25) Yeh, W.-C.; Li, P.-C.; Jeng, Y.-M.; Hsu, H.-C.; Kuo, P.-L.; Li, M.-L.; Yang, P.-M.; Lee, P. H. *Ultrasound in medicine & biology* **2002**, 28, 467.
- (26) Miyaji, K.; Furuse, A.; Nakajima, J.; Kohno, T.; Ohtsuka, T.; Yagyu, K.; Oka, T.; Omata, S. *Cancer* **1997**, 80, 1920.
- (27) Miller, K.; Chinzei, K.; Orssengo, G.; Bednarz, P. *Journal of Biomechanics* **2000**, 33, 1369.

- (28) Engler, A. J.; Sen, S.; Sweeney, H. L.; Discher, D. E. *Cell* **2006**, *126*, 677.
- (29) Suresh, S. *Acta Biomater* **2007**, *3*, 413.
- (30) Suresh, S. *Nat Nanotechnol* **2007**, *2*, 748.
- (31) Gratton, S. E.; Ropp, P. A.; Pohlhaus, P. D.; Luft, J. C.; Madden, V. J.; Napier, M. E.; DeSimone, J. M. *Proc Natl Acad Sci U S A* **2008**, *105*, 11613.
- (32) Beningo, K. A.; Wang, Y. L. *J Cell Sci* **2002**, *115*, 849.
- (33) Discher, D. E.; Janmey, P.; Wang, Y. L. *Science* **2005**, *310*, 1139.
- (34) Wang, N.; Butler, J. P.; Ingber, D. E. *Science* **1993**, *260*, 1124.
- (35) Guck, J.; Schinkinger, S.; Lincoln, B.; Wottawah, F.; Ebert, S.; Romeyke, M.; Lenz, D.; Erickson, H. M.; Ananthakrishnan, R.; Mitchell, D.; Kas, J.; Ulvick, S.; Bilby, C. *Biophys J* **2005**, *88*, 3689.
- (36) Suresh, S.; Spatz, J.; Mills, J. P.; Micoulet, A.; Dao, M.; Lim, C. T.; Beil, M.; Seufferlein, T. *Acta Biomater* **2005**, *1*, 15.
- (37) Stolz, M.; Raiteri, R.; Daniels, A. U.; VanLandingham, M. R.; Baschong, W.; Aebi, U. *Biophys J* **2004**, *86*, 3269.
- (38) Puig-de-Morales-Marinkovic, M.; Turner, K. T.; Butler, J. P.; Fredberg, J. J.; Suresh, S. *Am J Physiol Cell Physiol* **2007**, *293*, C597.
- (39) Mills, J. P.; Qie, L.; Dao, M.; Lim, C. T.; Suresh, S. *Mech Chem Biosyst* **2004**, *1*, 169.
- (40) Evans, E. A. *Biophys J* **1973**, *13*, 941.
- (41) Hochmuth, R. M. *J Biomech* **2000**, *33*, 15.
- (42) Shevkoplyas, S. S.; Yoshida, T.; Gifford, S. C.; Bitensky, M. W. *Lab Chip* **2006**, *6*, 914.

- (43) Koutsouris, D.; Guillet, R.; Lelievre, J. C.; Guillemin, M. T.; Bertholom, P.; Beuzard, Y.; Boynard, M. *Biorheology* **1988**, 25, 763.
- (44) Shelby, J. P.; White, J.; Ganesan, K.; Rathod, P. K.; Chiu, D. T. *Proc Natl Acad Sci U S A* **2003**, 100, 14618.
- (45) Bao, G.; Suresh, S. *Nat Mater* **2003**, 2, 715.

Chapter 2

Towards Synthetic Red Blood Cells: Using Mechano-biological Mimicry to Extend Circulation Times of Hydrogel Microparticles

2.1 Introduction

The effect of changes in the physical and mechanical properties of nano- and microparticles on their *in vivo* behavior in the circulation has become an area of growing interest, with increasing attention directed to the design of particles for use in the fields of drug delivery and medical imaging¹⁻⁵. Many basic design parameters have relevance on the behavior of synthetic particles once introduced to the circulation, including particle shape, size, aspect ratio, charge, surface chemistry and deformability. While the precise nature of the body's response to changes in each of these parameters remains a focus of intense study, some guidelines have been determined.

Size has been, perhaps, the most well explored parameter for particles in the field of drug delivery and has long been considered the dominant factor in the determination of *in vivo* behaviors such as circulation time, biodistribution profile, and mechanism and rate of cellular internalization^{3,6,7}. For example, microparticles are generally regarded as unsuitable for intravenous application due to their rapid clearance times, while the ideal nanoparticle design gives diameters below 100 nm¹. The interaction of cells with particles can be determined, to some extent, by tuning parameters like particle size and shape; the rates and mechanisms of cellular internalization for micro- and nanoparticles are influenced by both particle shape^{6,8} and deformability⁹. Filamentous particles were found to have increased circulation times with respect to their spherical counterparts, though this effect may be a factor of both the shape and deformability of these particles or their tendency to fragment to avoid uptake⁵. Particles with negative surface charge are less likely to undergo cellular internalization than those with positive charges due to electrostatic repulsion with negatively charged cell membranes⁶

Though particle size has long been considered dominant in determining *in vivo* behaviors such as circulation time and biodistribution profile, it stands to reason that physical filtration barriers in the body could be navigated by larger, but more deformable particles^{7,10}. Deformable particles which resembled RBCs in size and shape have been shown to deform in restricted channels¹¹ or capillaries¹² which were smaller than the particle diameter, though the modulus of these particles was not characterized¹¹ or was poorly matched to RBCs¹² and was restricted to *in vitro* testing in both cases. In one case, Haghgooie *et al.* fabricated discoid particles with 8 μm diameter by stop flow lithography from solutions of 700 g/mol molecular weight PEG diacrylate in 200 g/mol PEG with the polymerizable monomer between 10 and 40% v/v¹¹. The deformability of these particles was tested by passing them through microfluidic channels which were 4 μm in diameter and 4 μm tall at low pressures. This allowed for a qualitative examination of particle deformability as the pressure in the channels could be changed to obtain a threshold pressure for pushing the particles through the small channels as the crosslink density was varied. An interesting result of this study was that the particles deformed to navigate the channels primarily by folding, rather than stretching, as is more typical for RBCs.

To replicate the hollow membrane structure of natural RBCs, Doshi, et al. used spherical particles as a template for layer-by-layer assembly of complementary polyelectrolytes¹². Dissolution of the spherical template resulted in a biconcave collapsed structure which was similar in shape to mature red blood cells. The authors determined the elastic modulus of their particles from force-indentation curves obtained by AFM, and found their particles to be over 6 times stiffer than similarly evaluated RBCs (92.8 kPa and 15 kPa respectively). The particles were able to deform when passed through a circular capillary

(5µm diameter) which was smaller than their diameter (6 µm). These particles were not evaluated in vivo.

In a simulation of renal filtration of soft particles, microgels translocated through pores that were 1/10th of the particle diameter under physiologically relevant pressures¹³. In this study, Hendrickson, et al. applied 0.5 psi of hydrostatic pressure on track etch membranes with 100 nm pores to drive hydrogel particles as large as 1 µm in hydrated diameter through the pores. In the kidneys, renal filtration occurs by passage through endothelial gaps which are approximately 8 nm in diameter with a pressure differential of 0.7-1.5 psi¹³. Particles with hydrated diameters of 116 nm were passed through membranes with 10 nm pores with 0.5 psi in a more realistic simulation of renal filtration conditions. Two flexible gels, with different crosslink densities correlating to bulk modulus values of 8 and 13 kPa, were examined in these studies, though the particles made from these materials showed a similar ability to traverse the pores. These gels may not have direct biological relevance, as they were fabricated from crosslinked poly(N-isopropylacrylamide), which would collapse at physiological temperatures (37 °C) above the lower critical solution temperature of the hydrogel (32 °C), rendering them less deformable.

Filamentous worm-like micelles (filomicelles) were found to have increased circulation times with respect to their spherical counterparts, though this effect was attributed to the size and shape of these particles as well as the deformability⁵. These filomicelles were observed to decrease in length with increasing time in vivo; a factor which may be crucial to their extended circulation times. Initiation of a phagocytotic event results in a fragmentation of the filament, leaving behind a fragment but with the bulk of the filament avoiding uptake.

Inspired by nature's example of long-circulating microparticles, we sought to mimic the size and shape of RBCs while varying the modulus across a physiologically relevant range to probe the physical barriers encountered *in vivo* by soft microparticles. The mammalian red blood cell (RBC) presents a fascinating example of a biological particle for which deformability is essential to function. Once mature, mammalian RBCs eject their nucleus and all of their organelles, and so neither self-replicate through mitosis nor synthesize any RNA or proteins to effect cellular repairs¹⁴. The extraordinary flexibility of mammalian red blood cells (RBCs) enables them to deform many thousands of times during their long lives in the circulation with up to 100% strain¹⁵ as they pass through restrictions in the vasculature which are smaller than their diameter. During their 120 day lifetime, RBCs experience chemical changes to their membrane structure, rendering them less flexible, and leading to their removal from the circulation via splenic filtration¹⁶. Instead, RBCs remain in the circulation for a finite time, approximately 120 days, before a gradual decrease in their flexibility results in their clearance. The extreme flexibility of RBCs is such that, when young, they routinely deform to pass through capillaries throughout the body and the slit-like sinusoids in the spleen which are much smaller than their diameter. During their lifetime they experience gradual chemical changes to their membrane structure, rendering them less flexible, and which cause their removal from the circulation via splenic filtration at the end of this lifecycle¹⁶. Beyond RBCs, cancer cells, especially metastatic cancer cells, are elastically softer than healthy cells, a characteristic that is believed integral to their ability to spread to new locations^{17,18}.

Here we show that increasing the deformability of RBC sized particles to biologically relevant levels increased their circulation times beyond that of conventional microparticles

and significantly altered their biodistributions. Particle deformability was inferred from the measured properties of the bulk materials, and evaluated by multiple *in vitro* methods, including microscopy-based inspection, measuring filtration times through a track etched membrane, and by passing the particles through microfluidic devices with narrow channels. We found that, as a consequence of their low modulus, these discoid microparticles bypassed several *in vivo* filtration mechanisms, illustrated by animal survival and dramatic increases in elimination half-lives of particles with decreasing modulus. Such deformable and long-circulating particles may find utility in the fields of drug delivery and medical imaging, where long circulation times and varied biodistributions are often desirable characteristics¹⁻³. Further, we expect these results will stand as an introduction for particle deformability as a vital design parameter that can affect the behavior of particles on both the micro and nano scales.

2.2 Results and Discussion

2.2.1 Early Designs of Deformable PRINT RBC Mimic Particles

2.2.1.1 Design of Deformable Particles

Our initial efforts to design deformable RBC mimicking PRINT particles were based on the addition of a porogen to previously established particle matrices. Previously, Gratton et al. used PEG triacrylate and 2-aminoethyl methacrylate (AEM) as primary components of their particle matrix for multiple *in vitro* and *in vivo* studies¹⁹. Here, a non-reactive porogen, PEG₅₅₀dimethyl ether (PEG₅₅₀), was added in varying percentages to a particle matrix in order to decrease crosslink density and increase the deformability of the particles. As a qualitative measure of deformability, scanning electron microscopy (SEM) was used to

examine deformable PRINT particles. Particles were made from a formulation consisting of 89% PEG₄₂₈ triacrylate, 10% mPEG₁₀₀₀ methacrylate and 1% DEAP photoinitiator. As seen in **Figure 2.1**, particles made from this formulation, mixed 1:1 (by weight) with a porogen appeared to be much more deformable, with a striking resemblance to actual red blood cells.

An amine functional monomer, AEM, was incorporated into the particles to allow for facile surface functionalization. Surface coatings of PEG or other hydrophilic polymers on particles creates a hydrophilic steric barrier, which has been shown to prevent aggregation and to provide colloidal stability to particle dispersions^{20,21}. Particles fabricated with a 7 μ m PRINT disc PRINT mold were composed of 50% AEM, 48% PEG₄₂₈ triacrylate, and 2% HCPK (photoinitiator), with porogen (PEG₅₅₀) added to this preparticle solution. After washing the particles to remove the porogen, SEM examination revealed that particles fabricated with 50% porogen appeared flexible and were largely unbroken. Greater amounts of porogen made the particles too fragile to survive the fabrication and purification process, possibly as a result of phase separation. As seen in **Figure 2.2**, particles with 75% and 90% porogen have large pores visible, and were easily broken by the purification process.

These experiments provided an initial insight into the interplay between increasing deformability and decreasing toughness. It was concluded that the addition of greater than 50-60% of a porogen could result in an undesired loss of particle durability. As such, the addition of porogen was limited to 60% or less to maintain particle integrity.

2.2.1.2 Evaluating Deformability by Filtration Times

To evaluate the deformability of these porogen added 7 μ m disc particles, we initially measured time for filtration through a Nucleopore polycarbonate membrane with 5 μ m pores

(Whatman, Ltd.). This method of measuring filtration times through membranes has been used extensively to evaluate the relative deformability of RBCs, with stiffer cells taking longer times to pass through the filter²². Particles for the filtration studies were composed of 28% AEM, 60% PEG₄₂₈ triacrylate, 10% PEG₁₀₀₀ methacrylate, 1% Fluorescein-o-acrylate, and 1% HCPK. In this work, filtration was driven by an aspirator generated pressure differential (**Figure 2.3**). Particles were prepared without added porogen (PEG₅₅₀), or with 25%, 50% or 60% porogen. As the concentration of particles was measured by weight, an adjustment was necessary to produce solutions with approximately equal numbers of particles. Particles made with porogen were adjusted to account for the theoretical difference in particle density. For example, 5 mL of a 0.01 mg/mL solution of 0% porogen particles should have approximately the same number of particles as 5 mL of a 0.005 mg/mL solution of 50% porogen particles because the particle density is approximately 50% of the non-porous particle.

The times observed for filtration of 5 mL of these particle solutions followed the expected trend, with higher amounts of porogen resulting in more rapid filtration (**Figure 2.3**). Imaging of the filtrate revealed that a small number of particles had successfully passed through the membrane in the case of the particles with added porogen, though the number of particles in the filtrate was not quantified. Examination of the polycarbonate membranes after filtration showed large amount of particles remaining on the membrane in all cases, likely as a result of poor fluid flow through areas of the membrane which were in contact with a supportive backing. In contrast, a solution of human red blood cells in isotonic saline rapidly traversed the membrane while leaving no residual cells on the membrane. While some particles traversed the pores in these membranes, the difference in filtration times may

have been a result of the different porosity of the particles used in each case and the ease of passing fluid through them, rather than passing the particles through the pores. This method of measuring deformability may be best relegated to the examination of cells or non-porous particles in order to avoid this complication.

2.2.1.3 Preliminary *in vivo* Evaluation of Porous 7 μm RBC mimicking PRINT Particles

Preliminary *in vivo* evaluations of deformable RBC-like PRINT particles were conducted to determine the effect of modulus on particle circulation times. A series of 7 μm disc particles with decreasing crosslink density were prepared with compositions described in **Table 2.1**. For the most rigid particle (A) the matrix consisted primarily of a trifunctional PEG acrylate (PEG₉₁₂triacylate, 70%). A moderately deformable composition (B) included the addition of 50 weight percent of a non-functional porogen (PEG₅₅₀). The most deformable particle (C) replaced much of the trifunctional PEG acrylate with a difunctional PEG acrylate (PEG₃₃₀diacylate) in addition to the inclusion of 50% porogen. The increase in deformability was evident in the SEM images of the particles taken after purification (**Figure 2.4**).

Monomer	A (%)	B (%)	C (%)
PEG ₉₁₂ triacylate	70	35	5
2-aminoethyl methacrylate	28	14	14
Fluorescein o-acrylate	1	0.5	0.5
HCPK	1	0.5	0.5
PEG ₃₃₀ diacylate	0	0	30
PEG ₅₅₀ dimethylether	0	50	50

Table 2.1. The composition of 7 μm disc PRINT particles used for preliminary *in vivo* studies.

In this study, 7 μm disc PRINT particles were PEGylated and radiolabeled with ^{125}I to track their biodistribution. Particles were administered into healthy BALB/c mice via bolus tail vein injection at a dose of 20 mg/kg. The particles were radiolabeled using Iodogen® following the procedure recommended by the supplier (Pierce). Mice were sacrificed at time points 1, 3, 8, and 24 hours after dosing and tissues harvested. The tissue distribution was monitored using a gamma counter, and the percent recovery of injected dose was calculated from the measured radioactivity. The biodistribution of the particles is shown in **Figure 2.5**.

The particles examined in this study primarily distributed into the lungs, with the bulk of the recovered dose accumulating in this tissue. This was likely a first-pass filtration with the particle becoming entrapped in the capillary beds of the lungs directly after tail-vein injection, as this organ is almost immediately down-stream from the tail vein in the mouse circulatory system. All three groups showed similar behavior with regards to this filtration in the lungs, demonstrating that the decrease in modulus was insufficient to overcome this initial biological barrier for large particles in the circulation.

A modest amount of the injected dose remained at the injection site in the tail. This may be due to the rupture of blood vessels upon rapid injection of a large number of particles in a short period of time (< 5 seconds), creating endothelial gaps for particle retention. Very little (less than 1%) of the dose was detected in the kidneys, heart, spleen, bladder, brain or in the blood. A low, but significant amount of radioactivity was observed in thyroid gland, possibly indicating the biodegradation of particles, yielding radioactive I_2 . Production of iodine from biochemical degradation of iodinated proteins or peptides is not uncommon and is also consistent with the observation that signal in the thyroid, while remaining low overall, increased over the 24 hour period studied ²³.

Interestingly, the most deformable of the particles showed enhanced, though still low, accumulation in the liver which increased over the course of the study. This may have been due to mechanical fragmentation of these particles due to the stresses experienced in the circulation. Fragments of particles may have been sequestered in the sinusoidal walls of the liver, which is lined with discontinuous endothelium that allows for passive entrapment of foreign particulates or nanoparticles ¹⁹. Particle fragmentation in the circulation was undesirable for this study; fragmentation of the particles would serve to complicate the analysis of the distribution since smaller fragments could distribute differently than intact particles. Fragmentation and deformation seem to have been competing processes. Further, fragmentation would expose unPEGylated, positively charged surfaces, possibly leading to a more rapid uptake of fragments versus intact particles.

2.2.1.4 Evaluation of Bulk Mechanical Properties

To determine the modulus of the hydrogels used in the above studies, bulk samples of the materials were prepared. The samples were evaluated in both a dry state and after 24 hours of soaking in water to hydrate the gels (**Table 2.2**). While we were able to decrease

	A	B	C
Modulus – dry (MPa)	8.61	5.23	0.87
Modulus – hydrated (MPa)	2.45	1.57	0.76

Table 2.2. Modulus values for bulk samples of the materials used for the particles in the mouse study.

the modulus of the particles by decreasing the crosslink density of the matrix material, the Young's modulus of the materials remained much greater than that of red blood cells (15-26 kPa)^{12,24}. Indeed, even the most deformable particles, with a modulus of 760 kPa, were over an order of magnitude stiffer than RBCs.

2.2.1.5 Conclusions from Initial Studies

This work represented an initial effort to determine the effect of particle modulus on *in vivo* behavior. While neither of the particle formulations included in the studies showed significant differences from the “rigid” control particle, several important lessons were learned. The lack of difference in the *in vivo* profiles of the particles demonstrated that the changes in the modulus of the particles were biologically insignificant. That is, while the particles were made to be softer, they remained too rigid to navigate the first filtration barrier encountered in the circulation; the narrow capillaries in the lungs. The accumulation of the softest particle, C, in the liver, implies particle fragmentation *in vivo* and indicates that these materials may not be ideal for this application due to insufficient toughness. Further decreases in crosslink density for these, or similar, PEG di- or triacrylates, would yield a lower modulus material; however, a corresponding decrease in the material toughness would likely result in the advent of greater fragmentation.

More studies with these materials would be required to determine the nature of the material failure leading to fragmentation. There may have been phase separation of the different monomers leading to an inhomogeneity in crosslink density and, possibly the creation of fracture points at the phase boundaries or in the less-tough phase. The reaction rate of acrylates (such as the PEG di- and tri-acrylates) and methacrylates (AEM) should

differ to some extent, leading to blocky polymer chains, encouraging phase separation and reducing toughness. Uneven surface PEGylation may have led to particle aggregation in solution, which would have added to the initial sequestration of particles in the lungs.

While different hydrophilic polymers may be better suited for the fabrication of particles with RBC-like modulus, future work with PEG acrylate systems could avoid many of the above pitfalls with the advent of several changes to the particle matrix material. First, longer chain PEG diacrylates may be a better material choice than either the PEG triacrylates or shorter PEG diacrylates. These materials should decrease crosslink density while increasing the PEG character of the particles. Such an increase in PEG character may reduce the need for surface PEGylation, and therefore, inclusion of AEM in the particle matrix. Inclusion of the methacrylate component (AEM) may have resulted in phase separation in the particles and diminished the toughness of the particles; exclusion of this component may eliminate these issues. Inclusion of a solvent, such as water or a higher molecular weight organic, may serve to minimize any phase separation, resulting in greater particle homogeneity and better mechanical properties.

2.2.2 HEA-Based Red Blood Cell Mimics

2.2.2.1 Fabrication of HEA-Based Red Blood Cell Mimics

The particle replication in non-wetting templates (PRINT[®]) technique that has been developed in our laboratory allows for the fabrication of non-spherical, shape-specific particles through use of elastomeric fluoropolymer molds^{4,25}. Using PRINT, HEA-based particles were fabricated with similar size, shape, and deformability characteristics as RBCs (**Figure 2.6**). In these studies we chose to model the 6 μm diameter mouse RBC²⁶ and

observe the *in vivo* behavior of the RBC mimics (RBCMs). While the distinctive biconcave discoidal shape of mature RBCs is generally conserved throughout the animal kingdom, mouse RBCs (6 μm diameter) are slightly smaller than their human counterparts (8 μm diameter)²⁶.

2.2.2.2 Determination of Modulus of Bulk HEA Hydrogels

To evaluate the suitability of HEA hydrogels for RBCM particles, we hydrated macroscopic coupons of hydrogels with varying percentage of PEGDA cross-linkers with different molecular weights in water and tested their mechanical properties with an Instron 5556 Universal Testing Machine (Instron) with a strain rate of 5 mm/min. Many hydrogels exhibit excellent biocompatibility²⁷, with their swelling and deformability controllable by varying the amount of cross-linking in the gel²⁸. PEGDA crosslinkers with molecular weight of 700 and 4,000 g/mol were used, with longer PEG chains resulting in lower modulus gels. In addition to lower modulus compared to the shorter crosslinker (PEG₇₀₀DA), hydrogels made with PEG₄₀₀₀ DA had reduced swelling and were capable of greater strains without failure with comparable weight percentages of monomer. Generally, HEA hydrogels with low crosslink density were able to undergo high strains before breaking (>100%) and had a suitably low modulus for comparison with RBCs. Two compositions were fabricated “pre-swollen” as 25% solutions of monomers in water. While this had the intended effect of reducing the swelling that accompanied hydration of the gels, it served to decrease the strength of the materials (**Table 2.3**).

For the *in vivo* studies, several changes were made to the above hydrogel composition. To mimic the negatively charged RBC membrane, we added 2-carboxyethyl

Crosslinker	% PEG-DA (crosslinker)	% water in monomer solution	Modulus (kPa)	Stress at Yield (kPa)	% Strain at Yield	% Swelling with hydration
PEG ₇₀₀ DA	10	0	621 ± 25	82.3 ± 18.7	8.2 ± 1.8	240
PEG ₇₀₀ DA	1	0	89 ± 14	61.7 ± 6.1	91.9 ± 8.4	420
PEG ₇₀₀ DA	0.5	0	21 ± 4	15.4 ± 1.2	161.0 ± 1.0	1020
PEG ₇₀₀ DA	0.5	75	3.3 ± 0.4	5.3 ± 0.8	151.3 ± 28.2	314
PEG ₄₀₀₀ DA	5	0	28 ± 2.5	15.0 ± 2.4	79.0 ± 33.8	262
PEG ₄₀₀₀ DA	5	75	4.0 ± 2.6	5.1 ± 0.7	84.5 ± 12.8	128
PEG ₄₀₀₀ DA	1	0	14 ± 0.6	16.0 ± 1.8	132.0 ± 59.9	345
PEG ₄₀₀₀ DA	0.5	0	12 ± 2.5	8.0 ± 2.6	229.7 ± 58.4	360

Table 2.3. Mechanical properties of 2-hydroxyethyl acrylate hydrogels with varying length and weight percentage of poly (ethylene glycol) diacrylate (PEG-DA) crosslinker. Hydrogels were prepared in two cases as 25% solutions in water, increasing the flexibility of the gels. Swelling percentage represents the % increase in area of the coupons after 24 hours of soaking in water. Error represents one standard deviation, with n=3.

acrylate (10%). Fluorescent dyes were needed to facilitate tracking of the particles *in vivo*. Hydrogels composed primarily of 2-hydroxyethyl acrylate (HEA) that were lightly (1-10%, by weight) cross-linked with poly (ethylene glycol) diacrylate (PEGDA, MW=4,000g/mol) with a photoinitiator (1-hydroxycyclohexyl phenyl ketone), 10% CEA, and polymerizable fluorescent dyes (1%) were fabricated for modulus testing (**Table 2.4**). Fluorescein-o-acrylate was used as the polymerized dye for these bulk studies, and to improve depth of tissue penetration and avoid tissue autofluorescence, a near IR dye (Dylight₆₈₀maleimide) was used for *in vivo* applications. The addition of the bulky dye molecules to the polymer samples caused an increase in the hydrogel stiffness at higher crosslink densities (at 10%

Monomer	(%)
PEG ₄₀₀₀ diacrylate	1-10
2-Carboxyethyl Acrylate	10
1-Hydroxycyclohexyl Phenyl Ketone	1
Methacryloxyethyl Thiocarbonyl Rhodamine B	0.1
2-Hydroxyethylacrylate	Remainder
Polymerizable Dye	0-1
Total	100

Table 2.4. The composition of HEA hydrogels intended for *in vivo* use as RBCMs. The polymerizable dye for bulk samples was fluorescein-o-acrylate; for RBCM particles, the fluorescein-o-acrylate was replaced by Dylight₆₈₀ maleimide.

crosslinker, modulus equal to 63.9 ± 15.7 and 53.2 ± 19.1 kPa for hydrogels with, and without added dye, respectively). For samples with lower amounts of crosslinker (1 and 2%), there was little change in modulus of hydrated samples with and without dye, though we observed a decrease in the amount of water taken up by the samples which included dye (**Figure 2.7**). By lowering the amount of cross-linker from 10% to 1% in samples including dye, we tuned the modulus of the resultant hydrated polymer from 63.9 to 7.8 kPa, respectively (**Table 2.5**); overlapping the range of the reported modulus for RBCs (26 ± 7 kPa)²⁴. The above formulations were targeted for use in further studies.

% Crosslinker	Modulus of Bulk Material (kPa)	Distribution Half-life (hours)	Elimination Half-life (hours)	AUC (fluorescence*hour)	Average R ²
10%	63.9 ± 15.7	0.04 ± 0.001	2.9 ± 0.9	0.6 ± 0.1	0.8966
5%	39.6 ± 10.4	0.07 ± 0.04	5.1 ± 2.2	0.8 ± 0.6	0.9029
2%	16.9 ± 1.7	0.2 ± 0.02	7.1 ± 0.8	1.4 ± 0.3	0.9468
1%	7.8 ± 1.0	0.3 ± 0.1	93.3 ± 31.1	15.4 ± 15.6	0.9330

Table 2.5 Modulus values and compartmental analysis of RBCM particles from intravital microscopy experiments. Ranges given represent one standard deviation. Values were derived from scans of three mice.

2.2.2.3 RBCM characterization

Due to the swelling observed in the bulk hydrogel samples, we designed master templates and molds for these studies. Master templates with disc features were fabricated on 6 inch silicon wafers with features cast in SU-8 photoresist (**Figure 2.8**). To account for hydrogels with different swelling ratios when hydrated, masters were made with feature diameters between 1 and 6 microns. For the *in vivo* studies, the features of the masters were scaled-down from the desired hydrated particle diameter, to 2 or 3 μm , allowing the RBCMs to swell to the desired dimensions upon hydration. The RBCMs fabricated from these masters were discs that were 5.2- 5.9 μm in diameter and 1.22-1.54 μm tall, with the feature size and final RBCM dimensions dependent upon the percent of cross-linker and the mold used (**Table 2.6**). Filling the molds resulted in a meniscus, leaving the particles thinner in the middle and thicker at the edges (**Figure 2.6**). This effect, which is not uncommon for the PRINT method ⁶, yielded RBCMs that were reminiscent of the biconcave shape of RBCs.

	1% cross-linker	2% cross-linker	5% cross-linker	10% cross-linker	Mouse red blood cell
Particle Diameter (μm)	5.96 ± 0.27	5.68 ± 0.32	5.66 ± 0.34	5.18 ± 0.30	6.0^{26}
Zeta Potential (mV)	-24.2 ± 5.4	-23.6 ± 3.4	-19.9 ± 6.6	-17.2 ± 3.4	-46.6 ± 4.84

Table 2.6. Physical characteristics of RBCM particles and mouse RBCs. Error represents one standard deviation from the mean with n=50 for particle diameters, and n=16 for zeta potential measurements.

2.2.2.4 Biocompatibility of RBCMs

To assess the biocompatibility of the RBCMs, we performed in vitro cytotoxicity assays on HUVEC (endothelial) cells. We dosed cells with varied concentrations of RBCMs (1.5-200 $\mu\text{g/mL}$) and incubated for 72 hours (**Figure 2.9**) before performing both MTS and ATP-luciferase assays to assess cell life. Particles were well tolerated at all dosages tested by both assays, demonstrating a high level of biocompatibility. To examine the interaction of RBCMs with endothelial cells, we performed a flow cytometry-based cell uptake experiment²⁹. RBCMs were dosed to HUVEC cells at a concentration of 15 $\mu\text{g/mL}$ and incubated for 15 minutes, 1, 2, 4, and 24 hours then evaluated to determine the percentage of cells which had internalized the RBCM particles. Interaction between the RBCMs and cells were minimal, with less than 10% of cells having internalized particles after 24 hours of incubation time (**Figure 2.10**).

2.2.2.5 Microfluidic Examination of Particle Deformability

To demonstrate the ability of RBCMs to deform in flow conditions such as they might experience in traversing the microvasculature, we utilized a microfluidic device with constricted pores (**Figure 2.11**). Microfluidic models of vascular constriction have been explored to evaluate the behavior of natural and diseased RBCs³⁰ and synthetic mimics of RBCs¹¹. We designed a 3 μm tall channel with square pores that were 3 μm wide and 50 μm long and repeated many times over the length of the device. The height of the channels was too short for the RBCMs to orient vertically to pass through the restrictions, forcing the particles to deform in order to traverse the pores. The device design (**Figure 2.11 A**) included over 100 repetitions of 3 μm restricted pores over the length of the channel, as well as an

unrestricted 15 μm path on each side of the restrictions, running the length of the channel. This architecture tested the ability of the particles to deform repeatedly while providing an unobstructed path for fluid flow to maintain reasonably low pressures through the constricted pathways. While the smallest capillaries in the body have diameters of around 5 μm , RBCs routinely deform to traverse splenic sinusoids that are much smaller³¹. When dilute suspensions of RBCMs were flowed through the device at a constant flow rate (0.06 mL/min) the lower modulus RBCMs (1 and 2% crosslinked) navigated these pores while more rigid RBCMs rapidly clogged them. In flow, the 1% crosslinked RBCMs stretched in the 3 μm wide channels, increasing in length $239\% \pm 26\%$ ($n=15$) while flowing through the restricted channels, followed by a relaxation back to their original discoid shape in the absence of flow. This behavior is similar to that of natural RBCs, which deform under flow conditions and only fully resume their characteristic discoid shape once flow is halted³². While RBCMs have similar size, shape and deformability to RBCs, they differ in fundamental structure: RBCs are fluid filled sacs contained by a complex membrane that has extreme flexibility originating from the membrane structure^{33,34}, while the RBCMs are uninterrupted hydrogel discs. These two disparate structures should have different behaviors and mechanisms of deformation in constricted flow¹¹ though further studies are needed to elucidate these details for the RBCMs.

2.2.2.6 Intravital Microscopy

We used an intravital imaging method to examine the behavior of RBCMs when intravenously injected into mice. For intravital approaches, the microcirculation is directly observed with high spatial and temporal resolution, often through the use of surgical

techniques to expose tissues of interest^{35,36}. In our approach, we observed the peripheral vasculature through the skin of an anesthetized mouse's ear. We directly observed the RBCMs via the near-IR fluorescence of the particles by imaging every 2 seconds for 2 hours as the particles traversed this portion of the vasculature. Elimination curves were generated by tracking the change in fluorescent signal from the particles over time (**Figure 2.12**), normalizing each scan to the maximum intensity slice and plotting decay as a function of this maximum intensity.

2.2.2.7 Pharmacokinetic Analysis

Several pharmacokinetic models were investigated using a standard pharmacokinetic modeling program (WinNonlin (version 5.2.1; Pharsight Corp., Mountain View, Calif.)) to describe the plasma concentration versus time profiles to determine the best model. One- and two-compartment models with elimination from the central compartment, from the software's library, were investigated, as was a two-compartment model with elimination from both the central and peripheral compartments, which was built by our group. The evaluation of the goodness of fit was based on the Akaike information criterion, the variability (CV) of the parameter estimates, and the absence of a significant correlation between independent model parameters (<0.95). The two compartment model with one elimination step from the central compartment provided the best fit for all of the data sets examined.

To evaluate the kinetics of RBCM clearance, we used this two compartment pharmacokinetic model, characterized by a bi-exponential decrease in particle concentration over time³⁷, with parameters fit by non-linear regression analysis³⁸. This model describes an

initial (distribution) phase where the particles distribute from the plasma into various tissues, followed by a late (elimination) phase that describes the ultimate clearance of particles from the plasma (**Figure 2.12**). For small molecules and nanoparticles the distribution is attributed to extravasation into tissue; because of their size, the distribution of RBCMs may be due to physical entrapment in constricted capillaries or tissues with low blood flow rather than by an extravasation process. While we only observed the RBCMs for the initial 2 hours *in vivo*, the uncertainty associated with the mathematical fitting was minimized due to the large number of data points used to fit each curve (over 350). Calculated distribution and elimination half-lives ($t_{1/2(\alpha)}$ and $t_{1/2(\beta)}$, respectively) trended to longer times with decreased modulus (**Table 2.5**). While the least flexible RBCMs were cleared quite rapidly, circulation times increased with increasing particle elasticity, with the most deformable RBCMs eliminated over 30 times more slowly than their most rigid counterparts ($t_{1/2(\beta)} = 3.9$ days).

Intravital microscopy provided a method for direct observation of RBCM particles in the peripheral vasculature of mice, and allowed us to make a close and thorough examination of the initial clearance profiles of these particles. Our analysis provided curves with approximately 350 data points illustrating the elimination of these particles from the circulation over each two hour scan. Non-linear regression analysis yielded excellent fits, with the large number of data points adding a measure of certainty to the shape defined by these elimination curves. With a method of directly observing the particles, we expect that our detection limits should be quite low as we are able to discern individual particles in the scans. However, this method was not without limitations. Direct correlation of the intensity of the fluorescent signal of the particles to a particle concentration was difficult due to several factors, including variabilities in the depth, volume and flow rates in observed

portions of vasculature and the relatively fast movement of particles relative to the scanning speed of the microscope. Lacking the correlation to particle concentration, we were unable to perform a full pharmacokinetic analysis on the RBCMs examined, though much was learned through an analysis of the shape of these curves.

2.2.2.8 Evaluation of 1% RBCMs at Long Times

To verify the long-circulating behavior of 1% crosslinked RBCMs, we tracked particle concentration in blood at time points out to 5 days post-injection via a more traditional blood-draw method. We examined 3 mice per time-point, including 2, 8, 24, 72, and 120 hours post injection. At each time point examined, we sacrificed the mice, collected blood via cardiac puncture and measured the fluorescent signal from the particles in the whole blood, which was correlated to concentration through the generation of a standard curve (**Figures 2.13 and 2.14**). Pharmacokinetic analysis of this data by the two-compartment model discussed above was in good agreement with the data obtained from the intravital technique; both techniques showed a fairly rapid distribution of the majority of the dose to various tissues, with 10-15% remaining in the blood after 2 hours, resulting in an elimination half life of 3.6 days, with 5% of the injected dose remaining in the blood after 5 days (**Table 2.7**).

A (mg/mL)	B (mg/mL)	α (hr ⁻¹)	β (hr ⁻¹)	$\alpha t_{1/2}$ (hr)	$\beta t_{1/2}$ (hr)	V _C (mL)	AUC (mg*hr/mL)	CL _T (mL/hr)	Vd _{β} (mL)
0.19	0.048	0.24	0.0077	2.886	90.24	2.93	7.07	0.099	12.89

Table 2.7. Pharmacokinetic parameters for 1% crosslinked RBCMs calculated from blood draws taken out to 5 days post-injection.

2.2.2.9 Biodistribution of RBCM particles after Intravenous Injection

To examine the biodistribution of RBCMs with changing deformability, we sacrificed the mice two hours post-injection and harvested tissue and blood samples for further analysis. Tissue samples were not perfused prior to analysis. Five and 10 % crosslinked RBCMs distributed primarily into the capillary beds in the lungs (**Figure 2.15**). This behavior is typical for intravenously injected microparticles, with the bulk of the dose most likely sequestered immediately post-injection as this is the first downstream tissue with microvasculature. These stiffer RBCMs were poorly tolerated, with significant distress requiring sacrifice of some mice prior to scan completion; presumably due to the stiff particles contributing to pulmonary embolism. More flexible RBCMs (1 and 2% cross-linker) were very well tolerated, presumably due to the avoidance of filtration in the lungs. Mice which were sacrificed early were not included in any data sets presented here, as the time post-injection was incongruent with the bulk of the data analyzed. The most deformable RBCMs (1% crosslinked) were primarily sequestered in the spleen (67% RD/g), having largely avoided filtration in the lungs. Lung filtration was largely avoided by particles with 2% or less cross-linker (≤ 16.9 kPa, bulk material), suggesting that the modulus of these materials may indicate a threshold value for avoidance of filtration by the lungs. Uptake in the kidneys was significant for all but the 1% crosslinked RBCMs, though further studies will be required to elucidate the mechanism of this clearance.

Distribution of 1% crosslinked RBCMs in liver, lung, spleen and kidneys was tracked for 2, 8, 24, 72, and 120 hours post-injection (**Figure 2.16**). Saturation of tissues occurred at different times, indicating a redistribution of particles after some initial distribution at the time of dosing. While splenic accumulation peaked at 24 hours, signal in the lungs

decreased over the time course of the experiment; suggesting a delayed release of the physically entrapped particles back into the circulation.

With approximately 5% of the cardiac output flowing through the spleen¹⁶ and the total blood volume of the mouse circulating 7-8 times per minute³⁹, the whole blood volume was passed through the mouse spleen some 42-48 times over the course of our two hour scans. The continued persistence of 1% cross linked RBCMs in the circulation after this time suggests that splenic accumulation may be due in part to long residence time rather than permanent filtration, as is the case for RBCs, where filtration occurs first as an effect of slow blood flow through the macrophage-containing red pulp, followed by physical filtration when passing through the sinusoids or transmural apertures¹⁶.

2.2.3 Conclusions and Future Work

The above studies have clearly demonstrated the importance of particle deformability on *in vivo* behavior over a physiologically relevant range of mechanical properties. The most deformable particles, 1% crosslinked RBCMs, avoided filtration in the capillary beds in the lungs, leading to much slower clearance compared to particles which were stiffer. A 30 fold increase in the elimination half-life of the 1% RBCMs resulted from an approximately 8 fold decrease in elastic modulus. Interestingly, the modulus of the stiffer particles was higher than that of normal RBCs, but similar to that of pathological RBCs as evaluated by AFM²⁴, with normal blood cells (26 kPa) coming in softer than those with hereditary spherocytosis (43 kPa), anisocytosis (40 kPa) or G6PD deficiency (90 kPa). A comparison of 10% crosslinked RBCMs (70 kPa) with G6PD deficient RBCs or 5% crosslinked RBCMs (40kPa)

with spherocytosis or anisocytosis RBCs may provide insights on the role of RBC modulus in these diseases.

The method of the accumulation and retention of the RBCMs in the spleen may be of significant interest in future studies (**Figure 2.17**). The pharmacokinetic analysis suggests that accumulation in this tissue may be, in part, reversible. This makes sense physiologically, with low blood flow in the red pulp of the spleen causing a pooling of the RBCMs in this tissue over time. However, it is possible that the accumulation is due primarily to uptake of RBCMs by splenic macrophages in this tissue. The use of splenectomized mice for a study tracking the clearance of RBCMs over time may shed some light on this issue. Lacking this filtration mechanism, it is possible that RBCM pharmacokinetics would change dramatically, possibly following a one compartment model or with greatly extended circulation times.

Use of RES depleted mice represents an alternate strategy to probe the interaction of RBCMs with macrophages in the spleen and elsewhere. The intravenous application of clodronate liposomes has been demonstrated to specifically and temporarily deplete macrophages in the reticuloendothelial system⁴⁰. Once phagocytosed by macrophages, the liposomes accumulate inside the cells and cause cell apoptosis. This strategy has been employed to study the role played by the RES in tumor uptake⁴¹ and biodistribution⁴² of quantum dots. Changes in biodistribution and circulation profile of the RBCMs should indicate the role played by physical sequestration in the spleen versus cellular internalization.

Another interesting system for probing the interaction of RBCMs with macrophages is the integrin associated protein CD47, which acts as a “marker of self” on red blood cells and leukocytes⁴³. This protein binds to signal regulatory protein alpha on macrophages and serves to downregulate phagocytotic pathways. Expression of CD47 analogs provide

smallpox and vaccinia viruses some protection from macrophage clearance ⁴⁴, while overexpression of CD47 has a similar function in leukemia and hematopoietic stem cells ⁴⁵. Recently, CD47 was shown to inhibit macrophage uptake when conjugated to polystyrene beads in cell culture ⁴⁶. RBCMs appear to be a promising substrate for application of these “markers of self”, which may allow for even longer circulation times. The low blood flow conditions in the splenic red pulp assure proximity of RBCMs to splenic macrophages at this point in the circulation and inhibition of phagocytosis by recognition of “self” would most likely greatly extend circulation times.

Further studies will be required to illuminate the capability of these particles to carry and deliver therapeutic payloads, however, extremely low modulus RBCMs could have therapeutic applications for splenic disorders due to their preferential accumulation in this tissue, and have potential for drug delivery applications due to their long-circulation times and low accumulation in the liver. Drug dosing can be limited by toxicity to a clearance organ such as the liver^{47,48}. The apparent splenic clearance of RBCMs affords the possibility of different dosing restrictions if these particles were to be used as drug carriers because of the low concentrations found in the liver, as well as the possibility for direct treatment or imaging of the spleen.

In addition to carrying therapeutics, RBCMs should be evaluated for their capacity to carry hemoglobin (Hb) and transport oxygen throughout the body. Previous work by Kelly, et al. has demonstrated that the PRINT process is well tolerated by proteins ⁴⁹. To modify RBCMs to carry and deliver oxygen, Hb can be included in the pre-particle formulation. The primary anticipated challenges include the possible denaturation of some of the encapsulated Hb by the particle making process, difficulty in encapsulating erythrocyte like

amounts of Hb (up to 33% by weight) while retaining hydrogel strength and deformability, and leakage of Hb from the particles leading to renal toxicity. While some amount of denaturation may be inevitable due to the UV curing process and the free radicals generated therein, it may be possible to shorten the exposure time or decrease the temperature of the UV oven to increase Hb stability. Cargo encapsulation at high weight percentages may significantly alter the physical properties of the particle matrix material, requiring reexamination of the relative component ratios to obtain suitable moduli for long circulation times.

The most deformable of the RBCMs tested here successfully navigated regions of constricted blood flow, resulting in extended circulation times and illuminating a critical design parameter for microparticles. Further experimentation with extremely deformable materials on different size scales – from tens of nanometers to the 6 μm diameter particles used in this study, should cast light on the role played by deformability in enhancing the circulation times of biologically relevant particles.

2.3. Materials and Methods

2.3.1. Materials

Fluorocur[®], the perfluoropolyether (PFPE) used as the molding material in the PRINT process, was purchased from Liquidia Technologies (Product # 2M-140). Trimethylolpropane ethoxylate triacrylates (PEG triacrylates) and PEG diacrylates (Aldrich), were passed through short plugs of alumina prior to use to remove inhibitors. Photoinitiators 2,2-diethoxyacetophenone (DEAP), and 1-hydroxyl-cyclohexyl phenyl ketone (HCPK) were purchased from Aldrich and used as received.

Commercially available 2-hydroxyethylacrylate (HEA, 96%, Aldrich) contains impurities such as acrylic acid, ethylene glycol and ethyleneglycol diacrylate (EGDA), and was purified prior to use according to the procedure set forth by Elif, et al ⁵⁰. Briefly, HEA was dissolved in water (25% by volume) and the solution extracted 10 times with hexanes. Salt (200 g of NaCl/L) was added to the aqueous phase and the monomer extracted by washing with ether (4 times). The solution was dried with MgSO₄ (3 wt %), and ether removed by rotary evaporator. The purified monomer was distilled under vacuum prior to use. The purification of the HEA monomer and subsequent storage conditions were crucial to the reproducibility of the properties of hydrogels composed of this monomer. HEA was stored in aliquots at -20 °C to prevent degradation. It became apparent that, over time, the short-chain crosslinker (EGDA) was regenerating in solution. This was most readily apparent in particles made from older or improperly stored HEA, where the hydrated diameters were smaller than expected. We attributed this to the presence of some EGDA in the HEA monomer, which reformed over time. Proper storage of the monomer for up to 3 months (at -20 °C in aliquots to prevent repeated exposure to the atmospheric moisture) resulted in reproducible particle diameters.

Poly(ethylene glycol)₄₀₀₀diacrylate (PEG₄₀₀₀DA, Polysciences, Inc.), 2-carboxyethyl acrylate (Aldrich), fluorescein-*o*-acrylate (97%, Aldrich), Dylight₆₈₀maleimide (Thermo Scientific), Fluorescein-*o*-acrylate (97%, Aldrich), PEG₅₀₀₀N-hydroxysuccinimidyl ester (PEG₅₀₀₀NHS) (polysciences, inc.) and methacryloxyethyl thiocarbamoyl rhodamine B (PolyFluor 570, Polysciences, Inc.) were used as received. Iodogen® pre-coated tubes were purchased from Pierce Biotechnology, Inc., and radioactive iodine (Na¹²⁵I) was purchased from Perkin Elmer Life and Analytical Sciences, Inc. as 100 mCi/mL in 10⁻⁵ M NaOH. All

other chemicals were purchased from Fisher Scientific, and were used as received unless otherwise noted.

2.3.2 Fabrication of Master Templates

Master templates were fabricated at the North Carolina State University Nanofabrication Facility (NCSU NNF) using traditional photolithographic techniques. Photolithography is a process in which a film of photoresist on a silicon wafer is exposed to light that has passed through a patterned mask or reticle. The light induces a change in solubility in the photoresist, typically due to the presence of photoacid generators in the resist. In a positive resist, the exposed area becomes soluble. In negative photoresists, the light exposure causes a crosslinking reaction which renders the exposed regions insoluble. After exposure the soluble portion of the photoresist is removed with a developing solution. The resist pattern can then be used as part of a final device (more typical for negative resists) or as mask for etching the silicon wafer. In the case of etching of silicon, cleaning steps are used to remove residual resist from the wafer. Achievable feature sizes for each technique are largely dictated by the wavelength of light that is used to expose the photoresist.

Silicon wafers (6 inch) were purchased from Silicon Quest International and were used as received. Chrome on quartz reticles (6" x 6" x 0.250") were purchased from Benchmark technologies for use on the GCA 8500DSW stepper at the NCSU NNF with a negative resist. The reticles had clear circles with diameters five times the intended diameter of the features on the master templates due to the 5x reduction lens of the GCA stepper (Figure 2.18).

The wafers were coated with SU-8 photoresist at the desired thickness by diluting SU-8 2010 (58% solids, Microchem) with SU-8 thinner (Microchem). Due to the viscosity of the SU-8 resists, proper mixing was essential. Mixtures of SU-8 and the SU-8 thinner were covered in foil and mixed on a shaker for 6 hours prior to the spin coating procedure. Film thicknesses were determined by the % solids in the diluted SU-8 and were designed to obtain the desired feature heights (**Figure 2.19**). Obtaining uniform films across the diameter of the 6 inch wafers required special attention to several details. First, the spin coater had to be exhaustively cleaned prior to use, as the excess SU-8 caused any residual resist on the sides or top of the spin coater to drip onto the wafer, ruining the uniformity of the coating. This effect may have been due to the SU-8 thinner acting as a solvent for residues of other photoresists used in this shared equipment. Static dispensing of SU-8 (7.5 mL) was required, with an extended slow spin (300 rpm for 15 seconds) to coat the wafer, after which the spinning was allowed to stop completely (5 seconds) before the next step of the program spun the resist to the desired thickness (3000 rpm by 133 rpm/sec for 30 seconds). It was important to seal the top port of the spin coater lid to avoid bull's eye defects. The coated wafers were soft-baked at 95 °C for 90 seconds. Wafers with SU-8 films were prepared at UNC's cleanroom facility and transported in this state to NCSU in a light-proof wafer boat for exposure.

Features were exposed using the GCA 8500DSW i-line (365 nm laser) wafer stepper with a 5 x reduction lens at the NCSU NNF. Exposure times were 1 second per step. The wafers placed on a 95 °C hot plate for 2 minutes as a post-exposure bake. The resist was developed for 2 minutes in SU-8 developer, after which the wafers were hard baked at 165 °C for 30 minutes to increase feature durability. Feature heights were verified with a KLA

Tencor P-6 profiler, and by SEM of 99% PEG₄₂₈ triacrylate, 1% DEAP PRINT particles fabricated from the masters. Feature fidelity was confirmed by SEM examination of embossed cyanoacrylate (Zap CA PT-08, Pacer Technologies) film cast from PRINT molds prepared from these master templates (**Figure 2.8**).

2.3.3 Fabrication of Thick PRINT Molds

The 7 μm RBC particles were made from “thick” PRINT molds fabricated as follows: 10-12 mL of fluorocur® resin (Liquidia technologies) was placed onto a 6 inch silicon wafer etched with the desired pattern (raised discs with diameter of 7 μm and aspect ratio of 0.25). The resin was allowed to spread and completely wet the wafer for 3-5 minutes under a nitrogen purge in a UV oven, followed by 2 minutes of exposure to UV irradiation ($\lambda = 365$ nm, power > 20 mW/cm²) to cure the resin. The elastomeric mold was removed from the surface by gently peeling it away. This method describes the fabrication of a “thick mold”.

2.3.4 Fabrication of “Thin” PRINT Molds

Thin molds were fabricated by drop casting approximately 500 μL of Fluorocur resin onto a master template. The resin was spread out using a sheet of poly(ethylene teraphthalate) (PET) that had been specially treated for adhesion with the Fluorocur resin. The master was coated evenly with Fluorocur by laying the sheet onto the resin on the master, allowing it to spread, then peeling the sheet off and rotating it slightly before touching it back down to the master. This process was repeated multiple times until the entire master template was coated with PFPE resin. Air bubbles were removed from between the master template and the PET by peeling the PET all the way off of the PFPE-wetted master surface and slowly and *gently*

rolling the PET back over the master using a soft, rubberized roller which was longer than the width of the master. The master/PFPE/PET sandwich was placed in a UV oven. The oven was purged with nitrogen for 2 minutes, then exposed to UV light ($\lambda=365\text{nm}$) for 3 minutes to cure the resin. The PET with the cured resin was then peeled off the master template, yielding a thin mold consisting of a thin, patterned layer of PFPE bound to a PET backing sheet.

2.3.5 Particle Fabrication

For the PRINT technique^{4,6}, low surface energy molds are filled with a liquid pre-particle mixture using a variety of techniques so that the wells of the mold are filled while the area of the mold between the wells remains clean. For particles composed primarily of PEG triacrylates or PEG diacrylates, the particles were fabricated by spraying a 10% (w/v) solution of the monomers in isopropanol onto the mold to wet it evenly. The molds were allowed to dry for 5 minutes in air to allow the isopropanol to evaporate. The mold surface was covered with a sheet of PET and this assembly sent through a laminator with a heated nip at a slow rate while the PET was peeled back at a steady angle. A slow peel rate and steady peeling angle are essential for fabrication of large, low aspect-ratio particles to avoid filling defects or scum formation. Following this, the mold was placed in a UV oven, purged with nitrogen for 2 minutes and UV irradiation was applied ($\lambda = 365 \text{ nm}$, power > 20 mW/cm²) for 2 minutes to cure the particles.

The master templates and molds used to make HEA-based RBC particle had discoid features with 2 and 3 μm diameters and heights of 0.6 and 0.9 μm , respectively and produced particles with 5-6 μm diameters due to swelling of the particle hydrogel material. For the

fabrication of the particles, the pre-polymer mixture was spread onto a mold which was taped to a silicon wafer and chilled to 2-5°C on a custom built laminator platform. The reduced temperature prevented evaporation of the pre-polymer solution prior to photo-curing. A PET sheet was laminated to the top of the mold and pre-polymer solution, wetting the total mold area. The sheet was peeled away at the nip point of the laminator, leaving the wells of the mold filled while wicking away excess solution. The filled mold was immediately transferred into a chilled (~5°C), nitrogen purged UV oven and cured with UV light ($\lambda=365\text{nm}$, 3 minutes, power ~ 20 mW/cm²).

2.3.6 Ice-harvesting of Particles

Particles were harvested from the mold by freezing to a thin layer of ice, called “ice harvesting”. For this method, 1 mL of millipore water or 0.1% 2×10^3 g/mol poly(vinyl alcohol) (PVOH, Acros) in water was placed onto a substrate. The substrates used included clean, 6 inch silicon wafers, or PET sheets. The mold was placed face-down onto the substrate so that the water spread out evenly, forming a uniform layer between the substrate and the mold surface. This assembly was placed into a -80°C cooler (dry ice), but was not brought into direct contact with the ice. The assembly was allowed to freeze for at least 30 minutes; shorter freeze times resulted in poor harvest yields. The mold was peeled rapidly away from the substrate at a steep angle, leaving particles stuck to the layer of ice frozen to the substrate. Upon melting of the ice, particles were collected by pooling the solution on the wafer with a cell scraper, and collecting it with a pipette. This procedure was generally repeated two times per mold to harvest nearly 100% of the particles from the molds.

2.3.7 Particle Purification

PEG-acrylate particles were purified by washing up to 6 times with water or acetone via centrifugation, removal of supernatant and resuspension of the particle pellet with sonication and vortex mixing. The HEA based particles were washed and concentrated via tangential flow filtration with a MicroKros hollow fiber filter (500 kDa, Spectrum Laboratories, Inc.) to remove any sol fraction from solution. Particles were then suspended in 0.1% 2×10^3 g/mol PVOH in PBS, pH 7.4 for subsequent experiments.

2.3.8 Particle Characterization

HEA based particle dimensions were determined by analysis of images from a microscope mounted camera (Zeiss AxioCam MRm) using a 100x objective (Zeiss Axio Imager D.1M). Over 50 fully hydrated particles in pH 7.4 PBS buffer were measured for each case. Mouse red blood cells (RBCs) used for zeta potential measurements were pelleted and washed three times with cold PBS prior to crosslinking with 1% glutaraldehyde for 5 minutes. The mouse RBCs were washed with PBS and diluted 1000 fold with cold DI water for zeta potential measurements. Zeta potentials for HEA particles and RBCs were measured on a nano ZS zetasizer (Malvern Instruments) in water. The zeta potential of PEG-acrylate particles was measured using a ZetaPlus Zeta Potential Analyzer (Brookhaven Instruments Corporation) in water at a concentration of 0.3 mg/mL.

To obtain particle mass, the particles were transferred to a previously weighed eppendorf tube, centrifuged to pellet and the supernatant removed. This pellet was dried overnight in a vacuum oven to remove residual solvent, massed, and dispersed in saline to the appropriate concentration. The concentration of HEA based particles was determined

using thermogravimetric analysis (TGA) to determine the mass of particles in a small sample (20 μ L) of particle solution.

2.3.9 Surface modification of particles

To modify the surface of amine-containing particles with PEG, the particles were transferred to dry DMF and placed into a flame-dried vial. Freshly distilled triethylamine was added to the reaction mix, followed by addition of a solution of excess (2.5 molar equivalents compared to amines) PEG₅₀₀₀ NHS in DMF. The mixture was incubated at room temperature overnight with mixing. Acetic anhydride (excess) was added to quench any unreacted amines. Solvent was removed by applying vacuum with slight heating. Particles were resuspended in 1 M HCl and mixed for 5 minutes. Particles were then washed with water by centrifugation and resuspension, until the supernatant pH was neutral. The PEGylation reaction was monitored by the change in zeta potential of the particles from positive to negative values, with typical values of -25 to -45 mV for particles after PEGylation.

2.3.10 Humidity Control

Because of the low temperatures used during the particle fabrication process for HEA-based particles, a low level of relative humidity was required, beyond the typical ambient conditions in the laboratory. However, particle fabrication using PRINT requires a fair amount of manual dexterity and specialized equipment and proved impractical in a glove box environment. Subsequently, a small, single person enclosure was designed to maintain low humidity for this process using inexpensive and readily available equipment. A portable

greenhouse with polyethylene panels and a 6' x 6' footprint was used for the body of the enclosure. This was large enough to accommodate a table holding the chilled laminator and UV oven with some additional work space. The chiller unit for the chilled laminator and UV oven generates a fair amount of heat, and was placed outside of the enclosure with chilled fluid lines piped to the equipment inside. A small home dehumidifier was placed inside the enclosure to remove moisture from the air. Additionally, a compressed air line runs into the room through a drierite dessicator (Drierite Co. Ltd.) to put a positive pressure on the room with arid air. A heat-exchanger after the desiccator, consisting of 50 feet of coiled copper tubing in a dry ice/ipa bath, serves to cool the incoming air, offsetting the heat generated by the equipment and personnel.

Humidity in the room can be maintained at 20-30% at temperatures of 70-75 °F, which is sufficient to prevent condensation on the chilled laminator (the limiting factor). In the higher temperature months, when the relative humidity in the building soared to 50-60% at 72-74 °F, low humidity conditions became more difficult to maintain as the dehumidifier worked harder to dry the air, causing it to generate more heat. In this case, it was necessary to leave the enclosure for 15 minutes out of every hour to allow the temperature and humidity to drop back to acceptable levels.

2.3.11 Modulus Testing

To measure the mechanical properties of crosslinked hydrogels, macroscopic coupons of the prepolymer mixtures were polymerized via UV light in a Teflon mold. Approximately 650 μ L of prepolymer mixture was pipette into a 2.5 x 2.5 x 0.5 cm square mold. The mold was placed in a low-intensity UV oven, and nitrogen purged for 3 minutes prior to curing.

The low intensity oven was used to minimize the heat generated from the UV light. The coupons were cured for 5 minutes, allowed to cool for 3 minutes, then cured for an additional 3 minutes. The cross-linked hydrogels were removed from the mold, weighed, and placed in pH 7.4 PBS buffer for 24 hours to fully hydrate. The coupons were patted dry with paper towels and weighed again prior to testing with an Instron 5556 Universal Testing Machine (Instron) with a strain rate of 5 mm/min.

2.3.12 Radiolabeling of Particles with I¹²⁵

Radiolabeled particles were surface functionalized with Bolton-Hunter reagent (BHR, Sulfosuccinimidyl-3-[4-hydroxyphenyl]propionate) to provide a facile iodination site. Briefly, prior to the addition of PEG-NHS, BHR in DMF was added in a ratio of approximately 600,000 BHR/particle along with excess triethylamine. The reaction was allowed to proceed for 2 hours at room temperature, followed by the addition of PEG-NHS. Reaction proceeded as above. PRINT particles were radiolabeled using IodogenTM solid phase oxidant in the presence of Na¹²⁵I. Briefly, 10 mg of PRINT particles in 1 mL of H₂O, 53 μ L of phosphate buffered saline, and 1 mCi of Na¹²⁵I in 10 μ L of 10⁻⁵ M NaOH were added to an Iodogen pre-coated tube (50 μ g of Iodogen reagent) and the tube was swirled every other minute for 15 minutes. The radiolabeled particle solution was then transferred to a pre-weighed 1.5 mL Eppendorf tube. The original reaction tube was rinsed with one 20 μ L portion of 1 mM KI and with two 100 μ L portions of water and the rinsing solutions were added to the tube containing radiolabeled particles followed by the addition of NaHSO₃ (1 μ mol/10 μ L). The particle dispersion was then centrifuged for 10 minutes at 15,000 x g using an Eppendorf centrifuge 5415 D (Eppendorf). The supernatant was removed and the particles

were washed with four 500 μL portions of water (until the radiation in the supernatant was no greater than the background, ensuring complete removal of non-specifically bound ^{125}I) and evaporated to dryness in a SpeedVac SC100 (Savant Instruments). The total mass recovered was 9.45 mg. The specific activity was measured with a Beckman Gamma 5500B gamma counter (Laboratory Technologies) and found to be 5.5 $\mu\text{Ci}/\text{mg}$ PRINT particles.

2.3.13 Measuring Particle Filtration Times

To evaluate the deformability of 7 μm disc particles with added porogen, we measured the filtration time through a Nucleopore polycarbonate membrane with 5 μm pores (Whatman, Ltd.). The set up, seen in **Figure 2.3**, featured an Erlenmeyer flask topped with a rubber septum. The septum had two ports, one was directed to a water aspirator to generate vacuum to drive the filtration, the other port led to the filter assembly. The filter assembly (Whatman, Ltd.) held the membrane and was attached to a 10 mL syringe held upright without a plunger, acting as a reservoir for particle solutions to be filtered. A solution of particles (5 mL) was added to the open syringe, and the aspirator (held at constant flow for all experiments) connected. Filtration time was measured with a stopwatch. Solutions for this study were prepared to have approximately equal numbers of particles as a 0.01 mg/mL solution of 0% porogen particles. Particle density was assumed to fall linearly with the addition of porogen to adjust solution concentrations for equal numbers of particles/mL.

2.3.14 Microfluidics

Microfluidic masters were fabricated in the Chapel Hill analytical and nanofabrication laboratory (CHANL) cleanroom. Chrome on quartz masks were ordered from Benchmark Technologies. SU-8 was coated onto 6 inch wafers with film thickness

equal to the desired feature height. The wafers were soft baked at 95 °C for 90 seconds. A Karl Suss MA6/BA6 mask aligner was used to bring the mask into contact with the wafer, followed by 10 second exposure time. Post-exposure bake at 95 °C for 2 minutes was followed by soaking in SU-8 developer for 3 minutes to remove unexposed resist. The masters were hard baked at 165 °C for 30 minutes prior to fabrication of devices. Feature heights were analyzed using a P-6 profilimeter (KLA Tencor).

Microfluidic devices were fabricated from silicone (Sylgard 184, Dow Corning) sealed to glass after treatment with oxygen plasma. Flow in the devices was driven by a syringe pump at a fixed rate (0.06 $\mu\text{L}/\text{min}$). Dilute solutions of 1% crosslinked RBCMs (1-5 $\mu\text{g}/\text{mL}$ in PBS with 0.1% poly (vinyl alcohol)) were pumped through the channel and observed with a fluorescence microscope (Nikon TE2000). Videos were taken with a with a Photometrics Cascade II:512 camera. Particle stretching was analyzed with ImageJ software (NIH).

2.3.15 Intravital Microscopy

Intravital microscopy experiments were performed using an IV 100 laser scanning microscope (Olympus) on female BALB/c mice of 22-26 g body weight (Harlan Sprague Dawley). Hair was removed from the ear and a tail vein catheter was applied. The mice were anesthetized with isofluorane and placed onto a heated stage (37 °C) in a prone position, with an ear immobilized by taping to an aluminum block which was warm from contact with the heated stage. Vasculature was located by injection with a solution of 20 mg/mL rhodamine B labeled 70kDa dextran (Invitrogen) in PBS and visualized by excitation with a 568nm laser. A suspension of RBCMs, 33 mg particles/kg mouse weight via a 3.5

mg/mL solution of RBCMs in PBS with 0.1% poly (vinyl alcohol), was then injected and visualized using a 633nm laser. Controls were injected with the dextran solution followed by 200 μ L of PBS with 0.1% poly (vinyl alcohol). Imaging scans proceeded for 2 hours, with an image taken every 2 seconds.

For analysis of the circulation persistence of the particles, the image files from each scan were exported to imageJ. For ease of analysis, we followed the example of Tong, et al.⁵¹ and stacked the images in groups of ten. We analyzed the ROI containing vasculature for fluorescent signal in each scan and corrected for variation in laser intensity or autofluorescence by background correcting each image with the signal from a region of the scan which was free of vasculature. For comparison, we normalized each scan to the maximum intensity slice for that scan, providing curves which measured the clearance of particles from the peripheral vasculature over time as a percentage of the maximum signal.

2.3.16 Compartmental Analysis

Several pharmacokinetic models were investigated to determine the best model to describe the plasma concentration over time profiles collected with intravital microscopy, as well as the longer time point data collected via blood-draws. PK analysis was performed separately on each mouse using WinNonlin (version 5.2.1; Pharsight Corp., Mountain View, Calif.) software. Both one- and two-compartment models with elimination from the central compartment were investigated using models from the WinNonlin model library. To determine if the RBCMs followed a dual elimination mechanism, a two-compartment model with elimination from central and peripheral compartments built by our group was also investigated. The data were weighted according to the equation $1/C_i$, where C_i denotes the

predicted concentration or normalized fluorescent signal. All iterations were conducted using the Gauss-Newton algorithm⁵². The evaluation of the goodness of fit was based on the Akaike information criterion, the variability (CV) of the parameter estimates, and the absence of a significant correlation between independent model parameters (<0.95). Secondary PK parameters ($t_{1/2(\alpha)}$, $t_{1/2(\beta)}$, CL_s , CL_d , V_p , and AUC) were calculated from the estimated pharmacokinetic parameters for the long time point scans. The two compartment model from the WinNonlin library was found to best describe the data in all cases.

For determination of alpha and beta half-lives from the intravital microscopy scans, we applied the best-fit model from the WinNonlin analysis. The two compartment model assumes that particles are transported between the central and peripheral compartments with first-order kinetics and that particles are eliminated from the central compartment with first-order kinetics. The data was analyzed with equation 2.1, where C_p is the concentration of the particle in the plasma, and α and β are rate constants for the distribution and elimination processes, respectively.

$$C_p = Ae^{-\alpha t} + Be^{-\beta t} \quad \text{Equation 2.1}$$

The fit was calculated by nonlinear regression, maximizing the R^2 value for the fit and producing best fit values for the coefficients and rate constants³⁸. Half lives for the distribution and elimination process were calculated by equations 2.2 and 2.3, respectively.

$$\alpha_{t_{1/2}} = \frac{\ln 0.5}{\alpha} \quad \text{Equation 2.2}$$

$$\beta_{t_{1/2}} = \frac{\ln 0.5}{\beta} \quad \text{Equation 2.3}$$

AUC (area under the curve) was determined by integrating equation 4.1, which describes the plasma concentration/time profile (Equation 2.4).

$$AUC = \frac{A}{\alpha} + \frac{B}{\beta} \quad \text{Equation 2.4}$$

The volume of the central compartment, V_c , relates the dose administered and the initial particle concentration (equation 2.5).

$$V_c = \frac{Dose}{A + B} \quad \text{Equation 2.5}$$

Total body clearance, CL_T , describes the volume of blood cleared of particles over time, and is calculated from the dose administered and the AUC (equation 2.6).

$$CL_T = \frac{Dose}{AUC} \quad \text{Equation 2.6}$$

The volume of distribution in the elimination phase, Vd_β , describes the volume in which the particles would need to be disbursed to provide the observed concentration in blood for the elimination phase (equation 2.7).

$$Vd_\beta = \frac{CL_T}{\beta} \quad \text{Equation 2.7}$$

While exact values for particle concentrations in the plasma could not be calculated from the 2 hour intravital scans, the well defined shape of the elimination curves (350 points over 2 hours) allowed for determination of the half-life values, which are not dependant on absolute concentration.

Each elimination curve was analyzed individually for the above values, with the averages representing 3-4 mice per particle modulus.

2.3.17 Biodistribution

Controls and dosed mice were sacrificed 2 hours after injections, and blood and tissues harvested for imaging. Harvested tissues including liver, lung, spleen, kidneys, heart, and intestines were weighed, then imaged using an IVIS Kinetic fluorescence imaging system (Caliper Life Sciences) with excitation at 675 nm and emission measured at 720 nm. Blood was harvested via cardiac puncture, and pipetted in 100 μ L aliquots to black 96 well plates for analysis on the imager. The fluorescent signal for each tissue sample was background corrected by subtracting the signal from control tissues. Biodistribution profiles for the RBCMs at two hours post-dose were determined by percent of recovered fluorescence in the above tissues. Fluorescent signal in the blood was calculated by measuring the fluorescent signal from several aliquots of blood and extrapolating to account for the total blood volume in the mice (approximately 1.7 mL/20 g of body weight) ¹⁹.

2.3.18 Evaluation of 1% RBCMs at Long Times

Fluorescent signal from harvested blood was measured as above, with concentrations determined from a standard curve resulting from serial dilutions of particles in mouse blood. To verify the long circulating behavior of the 1% crosslinked RBCMs, 33 mg particles/kg mouse weight was administered with a 3.5 mg/mL solution of RBCMs in PBS with 0.1% poly (vinyl alcohol) via tail-vein injection to female Balb/c mice of 20-22g body weight. Three mice per time-point were examined, including 2, 8, 24, 72, and 120 hours post injection. At each time point examined, the mice were sacrificed and the lung, liver, kidney and spleen tissues were harvested and blood collected via cardiac puncture. The fluorescent signal from the particles was measured using an IVIS Kinetic fluorescent imager (Caliper

Life Sciences) with excitation at 675 nm and emission measured at 720 nm. Blood was pipetted in 100µL aliquots to black 96 well plates for analysis on the IVIS Kinetic imager, with blood measured in triplicate for each mouse. To track biodistribution of 1% RBCMs in lung, liver, kidney and spleen tissues over time, tissues were imaged as above and plotted as fluorescence efficiency per gram of tissue weight.

2.3.19 Histology

Lung tissues were frozen on dry ice shortly after harvesting and 10 µm frozen sections prepared for staining. Microscope slides with frozen tissue sections were allowed to thaw at room temperature for 20-30 min, at which point they were washed briefly with TBS. The sections were fixed with 2.5% paraformaldehyde in TBS for 5 min, followed by two 5 minute washes with TBS. The excess paraformaldehyde was quenched with 10 mM ethanolamine in PBS for 5 min, followed by washing twice with TBS for 2 minutes. The sections were permeabilized with 0.1% Triton X-100 (Alpha Aesar) in TBS for 5 min, and then washed with TBS twice for 5 min. The sections were incubated overnight at 4°C with 33 nM AlexaFluor₄₈₈ conjugated phalloidin (Invitrogen) and 1 µM To-Pro-3 iodide (Invitrogen), both solutions having been prepared using 0.025% Tween 20 (Fisher Scientific) in TBS. Following incubation, the sections were washed 4 times for 5 minutes prior to mounting with ProLong Gold antifade reagent (Invitrogen).

Spleen tissues were frozen on dry ice shortly after harvesting and 10 µm frozen sections prepared for staining. Microscope slides with frozen tissue sections were allowed to thaw at room temperature for 20-30 minutes, at which point they were washed briefly with TBS to remove media compounds. The sections were fixed with 2.5% paraformaldehyde in

TBS for 5 min, followed by subsequent washing with TBS twice for 5 minutes. Excess paraformaldehyde was quenched with 10 mM ethanolamine in PBS for 5 min, followed again by subsequent washing with TBS twice for 5 min. The sections were then incubated with 10% rat serum in TBS for 1 hr in a humidity chamber. After incubation, the sections were washed in TBS twice for 5 min. Following this, the sections were permeabilized with 0.1% Triton X-100 in TBS for 5 min, and then washed with TBS twice for 5 min. The sections were incubated overnight at 4°C with 0.2 µg/mL rat anti-mouse F4/80 antibody conjugated with AlexaFluor₄₈₈ dye (Invitrogen), as well as with 1 µM To-Pro-3 iodide, both of which were prepared using 0.025% Tween 20 in TBS containing 1% rat serum. Following incubation, the sections were washed 4 times for 5 min prior to mounting with ProLong Gold antifade reagent.

All samples were imaged with an Olympus FV 500 confocal laser scanning microscope with filters optimized for the different fluorescent probes, including the rhodamine B dye in the RBCMs. Images were taken with a 40x objective lens.

2.3.20 Assessment of Biocompatibility and Interaction with Endothelial Cells

HUVEC cells were seeded in 200 µL of media [HuMEC containing HuMEC supplement and bovine pituitary extract or Minimum Essential Medium (MEM) containing Earle's salts and both supplemented with 10% fetal bovine serum] at a density of 5,000 cells per cm² into a 96-well microtiter plate. Cells were allowed to adhere for 24 h and subsequently incubated with PRINT particles at concentrations ranging from 200 µg/mL to 1.56 µg/mL for 72 h at 37 °C in a humidified 5% CO₂ atmosphere. After the incubation period, all medium/particles were aspirated off cells. The ATP-luciferase assay requires 100

μ L fresh medium, which was added back to cells, followed by the addition of 100 μ L CellTiter-Glo[®] Luminescent Cell Viability Assay reagent (Promega). Plates were placed on a microplate shaker for 2 min, then incubated at room temperature for 10 minutes to stabilize luminescent signal. The luminescent signal was recorded on a SpectraMax M5 plate reader (Molecular Dynamics). The MTS viability assay utilizes 20 μ l of CellTiter 96[®] AQueous One Solution Reagent (Promega) into each well of the 96-well assay plate containing the samples in 100 μ l of culture medium. Plates were incubated at 37°C for 1–4 hours in a humidified, 5% CO₂ atmosphere. The absorbance at 490nm was recorded using a SpectraMax M5 plate reader (Molecular Dynamics). The viability of the cells exposed to PRINT particles was expressed as a percentage of the viability of cells grown in the absence of particles.

The HUVEC cell line was used to investigate the uptake of RBCMs with 1, 2, 5, or 10% crosslinker and which contained 1% fluorescein-o-acrylate as the covalently bound fluorescent dye. Cells were plated into 24 well tissue culture flat bottom plates (Corning/Costar 3526) and allowed to incubate overnight at 37°C, 5% CO₂. The following day, particles were diluted in complete medium to obtain a final assay concentration of 15 μ g/ml. 300 μ l of particles were then incubated with cells over a time course comprised of 15m, 1h, 2h, 4h, and 24h (37°C, 5% CO₂). After cell/particle incubation, the cells were washed with 1X Dulbecco's Phosphate Buffers Saline (DPBS) and detached by trypsinization (300 μ l/well). Cells were resuspended in a 1:1 solution of 0.4% trypan blue (TB) solution in 1X DPBS containing 10% FBS (500 μ l/well; total sample volume 800 μ l) and transferred to a 5 ml Falcon (352063) polypropylene round-bottom tube. This assay is based on the observation that, for non-internalized particles, the vital dye TB acts to quench the

fluorescence emission of the fluorescein bound to the particles, shifting the emission to red while an internalized particle will fluoresce green²⁹. Cells were analyzed by flow cytometry (CyAn ADP, Dako) for green and red fluorescence. There were 10,000 cells measured in each sample.

2.4 Figures

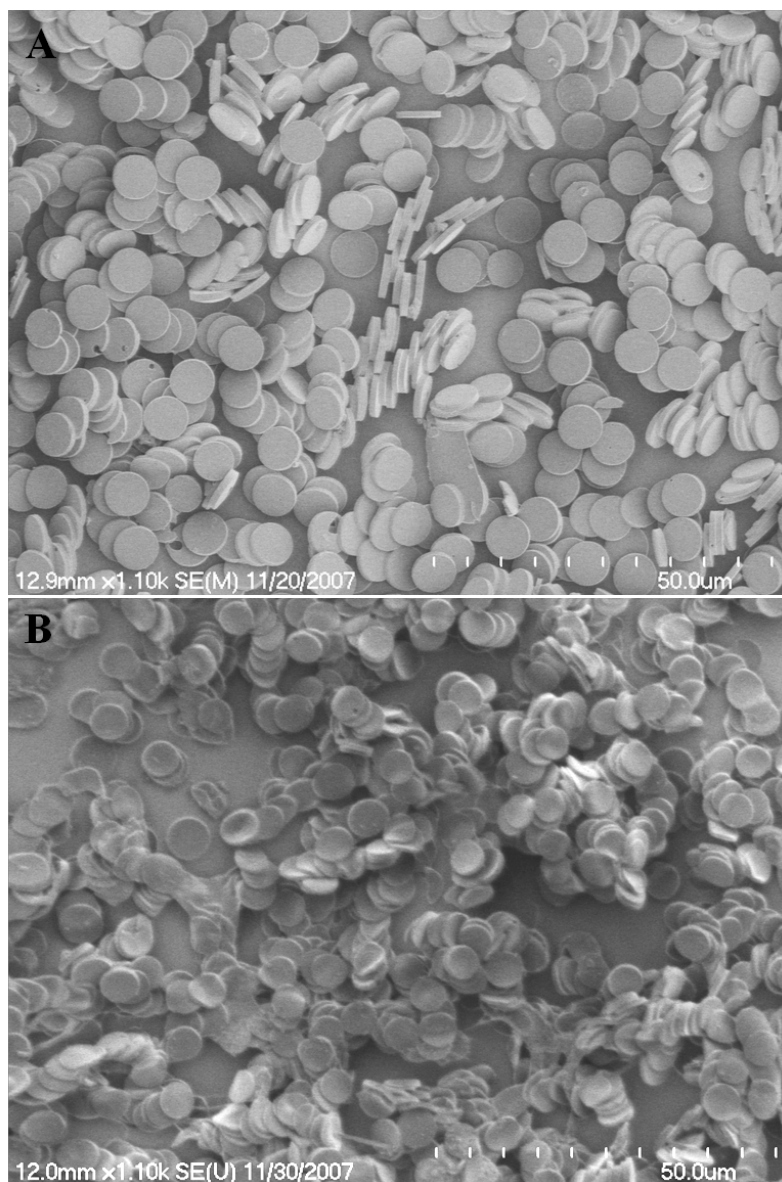


Figure 2.1. Scanning electron microscope images of 7 μm disc PRINT particles made from (A) 89% PEG₄₂₈ triacrylate, 10% mPEG₁₀₀₀ methacrylate and 1% DEAP photoinitiator and (B) 89% PEG₄₂₈ triacrylate, 10% mPEG₁₀₀₀ methacrylate and 1% DEAP photoinitiator mixed 1:1, by weight, with PEG₅₅₀ dimethyl ether as a porogen. The addition of porogen increases particle flexibility.

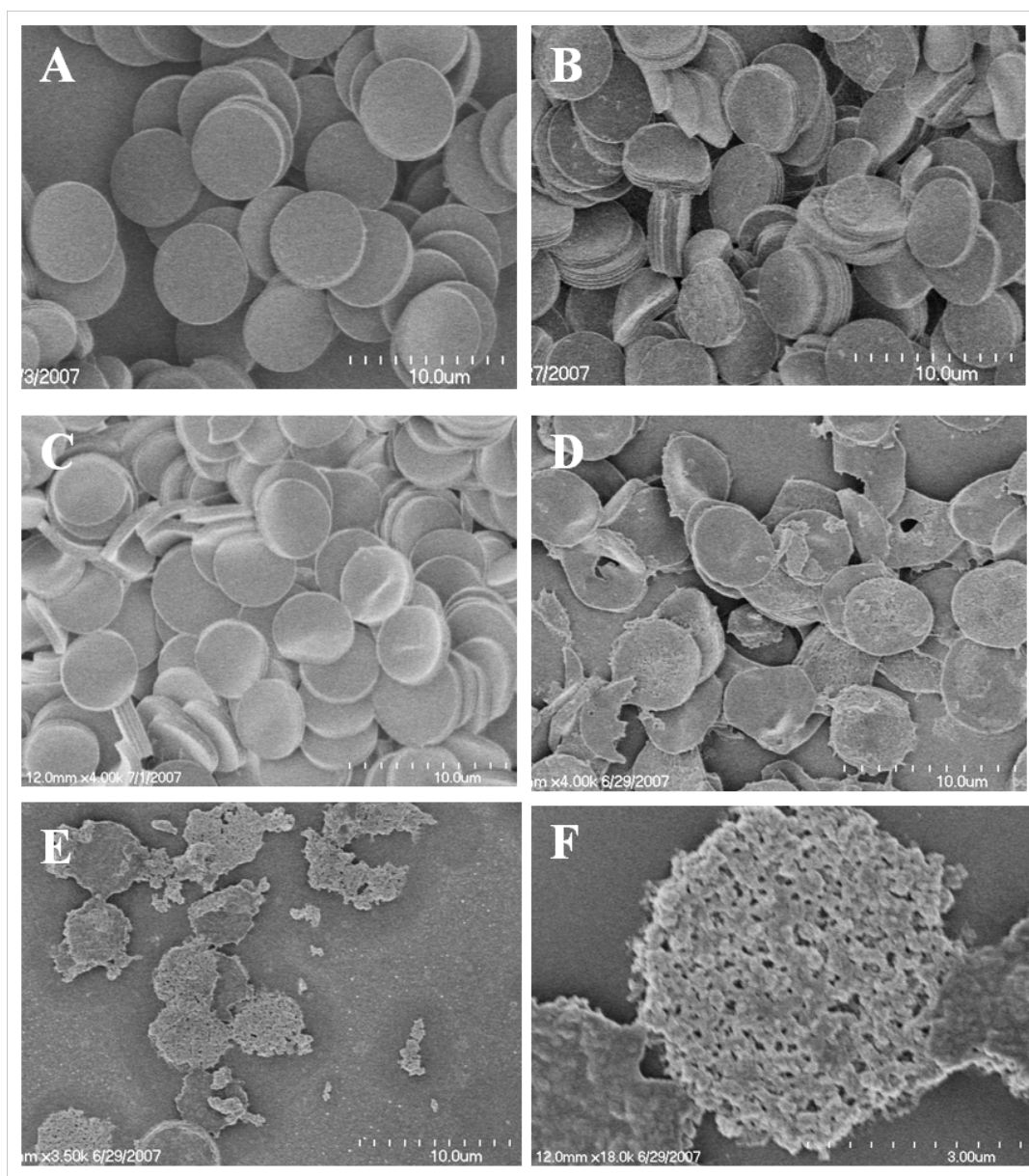


Figure 2.2. SEM images of 7 μm diameter, discoid PRINT particles with varying amounts of 550 g/mol molecular weight poly (ethylene glycol) added to the pre-particle solution as a porogen. The particles appear increasingly flexible, porous, and fragile as porogen content increases as follows: (A) 0 %, (B) 50 %, (C) 60 %, (D) 75 % and (E,F) 90 % porogen.

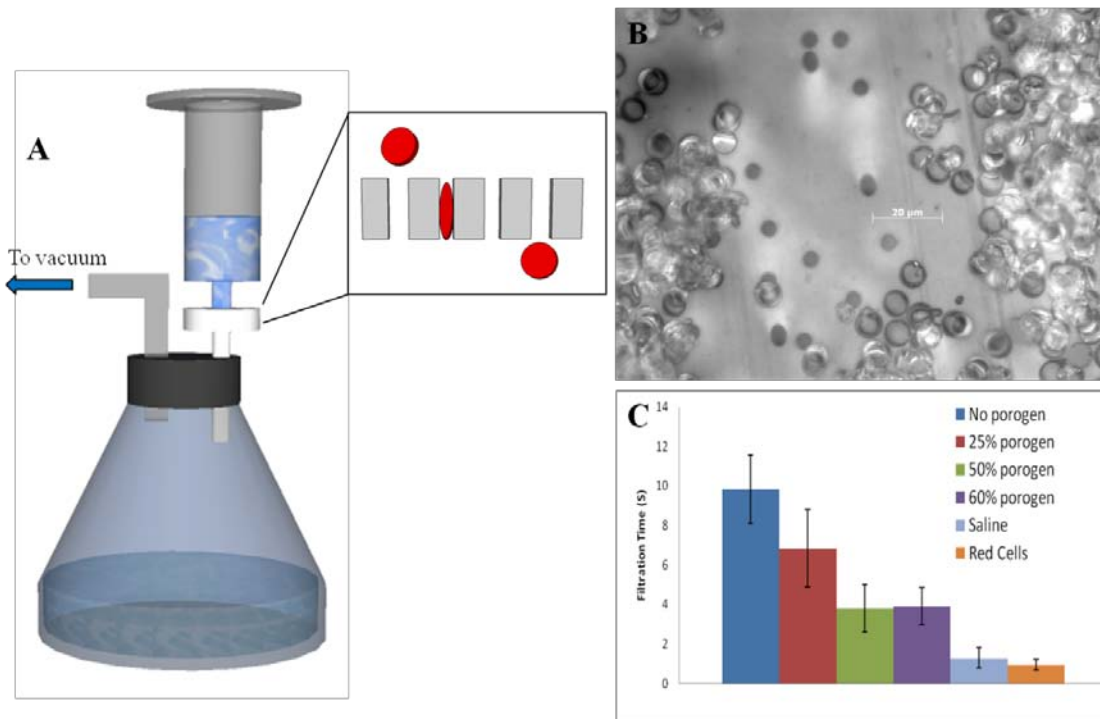


Figure 2.3. Measuring particle deformability by filtration times through a track-etched membrane. (A) A graphic showing the filtration set-up, with one port directed towards mild vacuum and a second port directed to the membrane apparatus. The cut-away depicts particles passing through the membrane. (B) A bright field microscope image of rigid particles (“No porogen”) on the membrane after filtration. Particles are along the sides and bottom of the image, with the membrane and some of the 5 μm pores visible in the center of the image. The scale bar is 20 μm . (C) Filtration times for 5 mL of particle or control solutions through a 5 μm nucleopore track etch membrane. Each plot represents $n=4$ with error bars as one standard deviation.

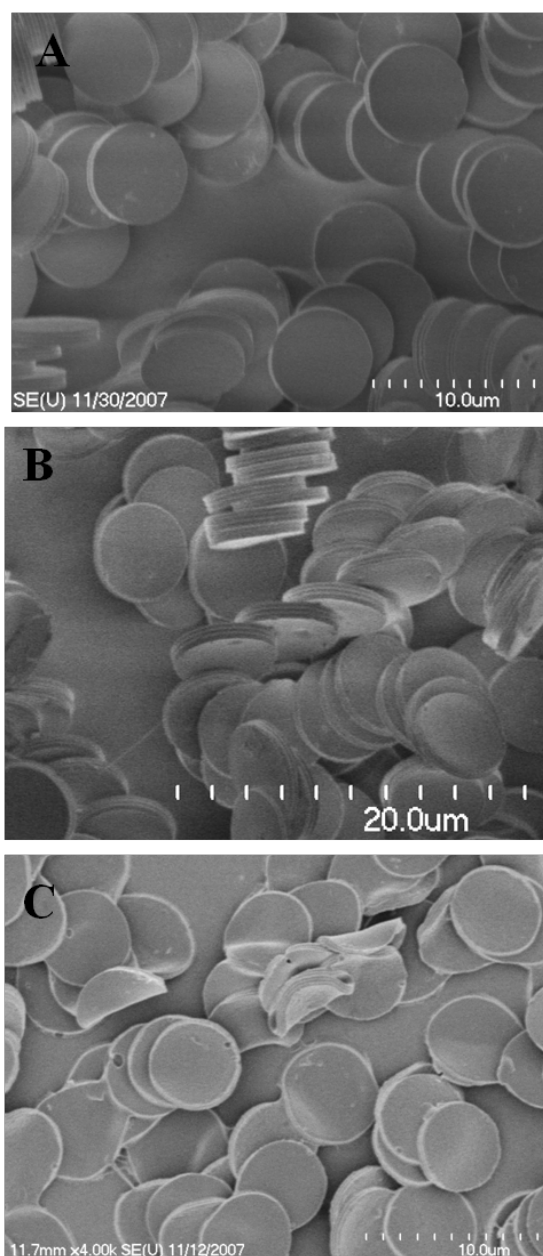


Figure 2.4. SEM images of 7 μm diameter, discoid PRINT particles with varying deformability used in preliminary *in vivo* studies. Rigid particles (A) contain no porogen while moderately deformable ones (B) were made with 50% (by weight) of a non reactive PEG porogen. The most deformable particles (C) were made primarily with a PEG diacrylate monomer in lieu of the triacrylate used in A and B, and included 50% porogen as in B.

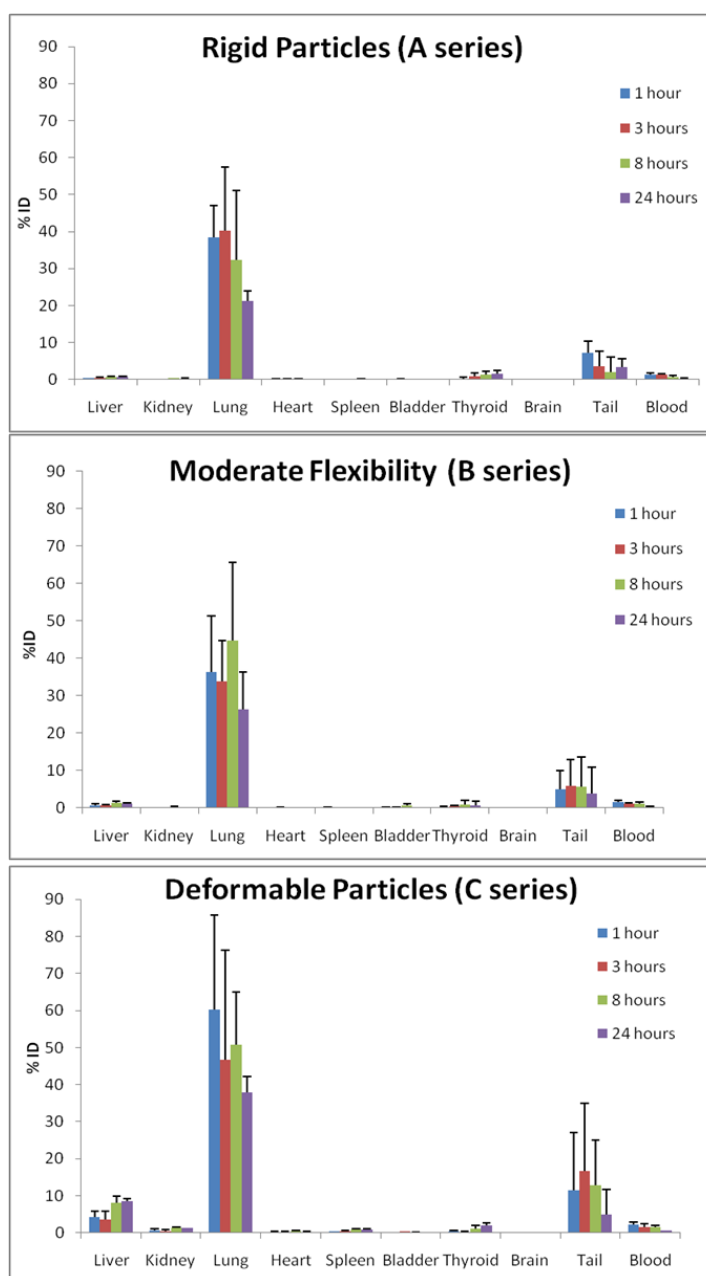


Figure 2.5. Biodistribution of 7 μ m diameter RBC mimic PRINT particles in mice as a function of % injected dose. Deformability of the hydrogel particles increases from A to C with the addition of a porogen in series B and replacement of triacrylate monomer with diacrylate in addition to porogen for series C. Particle accumulation in the tail is typical of tail vein injection procedures. Major accumulation occurred in the lungs in all cases along with poor persistence in the blood, suggesting that no formulation was deformable enough to navigate the narrow capillaries found in this organ.

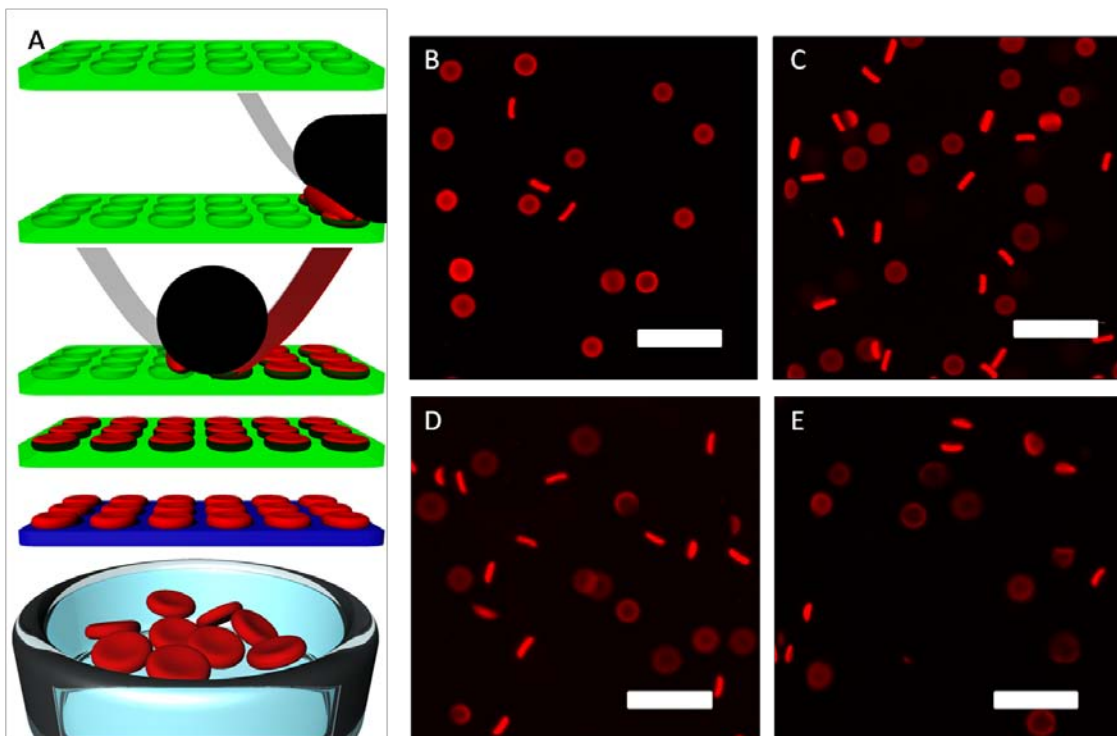


Figure 2.6. RBCM particles. (A) A graphical depiction of the PRINT process used to fabricate RBCMs. Briefly, from top to bottom, an elastomeric fluoropolymer mold (green) with disc shaped wells was covered by an aliquot of the pre-polymer mixture (red). The mold was passed through a pressured nip (black) covered by a high energy sheet (grey), wicking away excess liquid from the mold surface while filling the wells of the mold. The filled mold was cured photochemically, yielding cross-linked hydrogel particles, which were harvested from the mold by freezing onto a thin film of 1% poly (vinyl alcohol) in water (blue) and peeling away the mold. Melting of this layer resulted in a suspension of red blood cell mimic (RBCM) hydrogel particles. (B-E) Fluorescent images of hydrated RBCMs with varying % crosslinker (B) 10% crosslinked (C) 5% crosslinked (D) 2% crosslinked and (E) 1% crosslinked. Scale bars are 20μm.

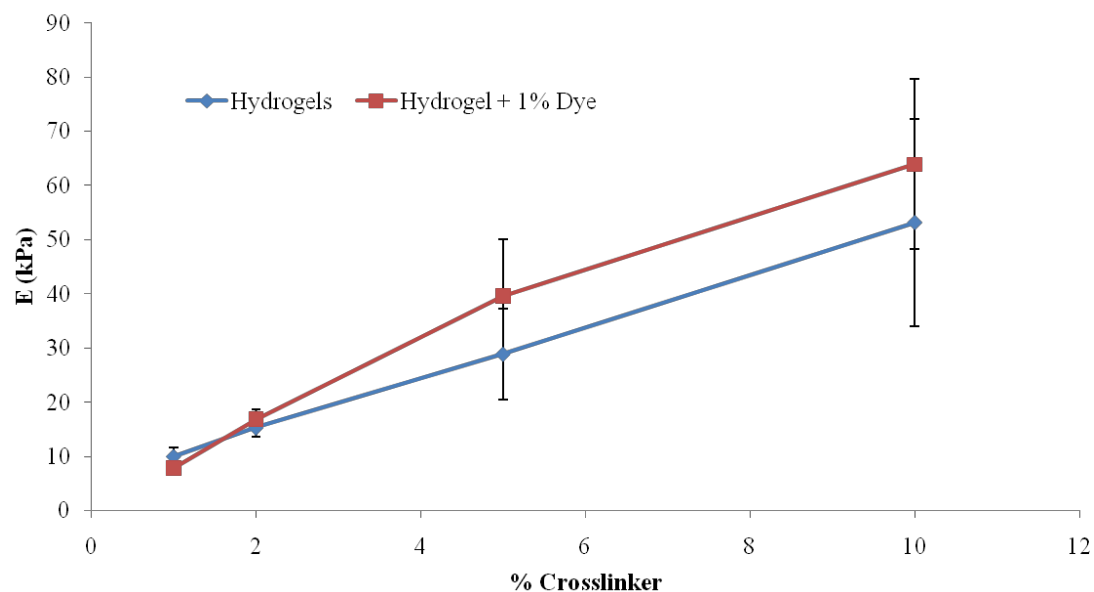


Figure 2.7. Modulus of hydrated samples of hydrogel as % crosslinker was varied from 1-10%. Additional dye (1% fluorescein-o-acrylate) was included to show the effect the addition of a near-IR dye to the composition for in vivo imaging applications.

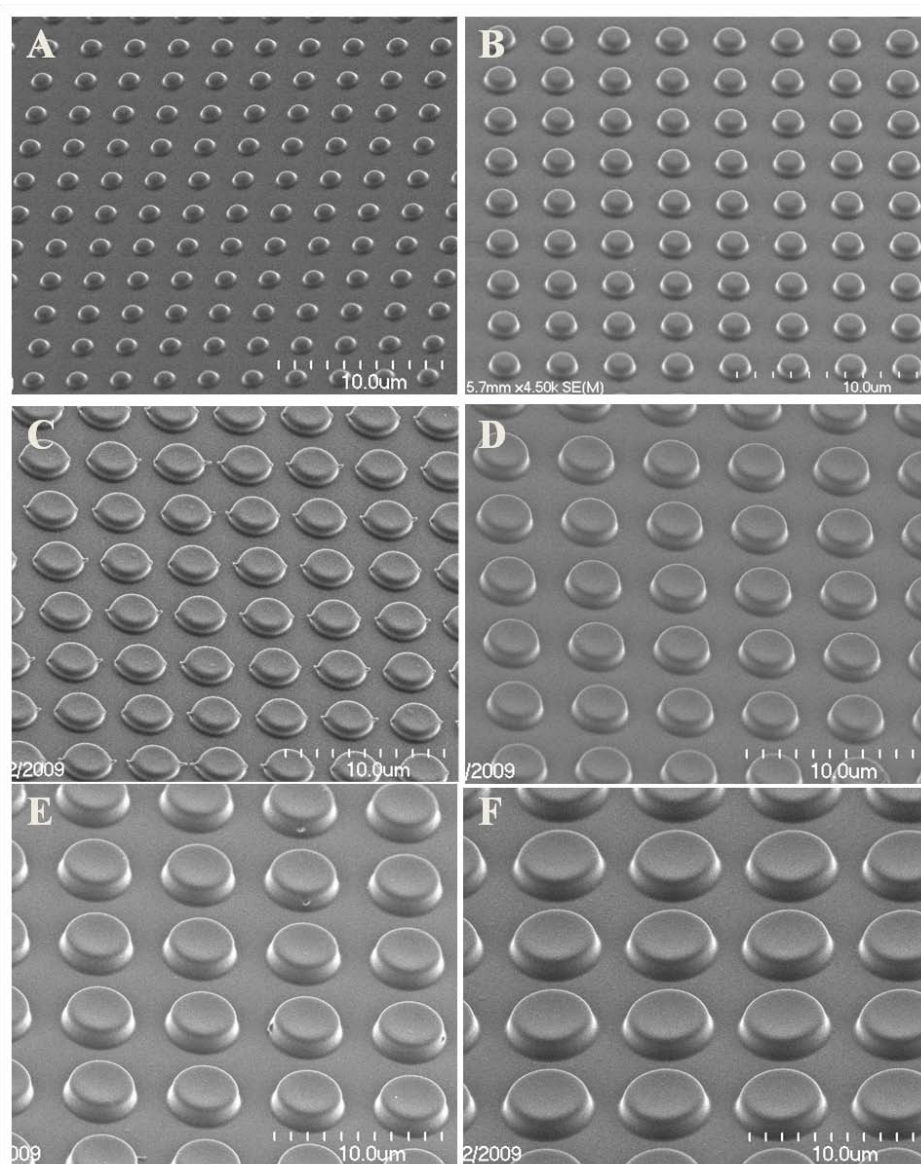


Figure 2.8. Discoid master templates fabricated in SU-8 on six inch silicon wafers. Discs with diameters of (A) 1.5 μm , (B) 2 μm , (C) 3 μm , (D) 4 μm , (E) 5 μm , and (F) 6 μm were prepared with an aspect ratio of 0.3. The scanning electron microscope images are shown at approximately the same scale and represent embossed films of cyanoacrylate cast from PRINT molds made using the appropriate masters.

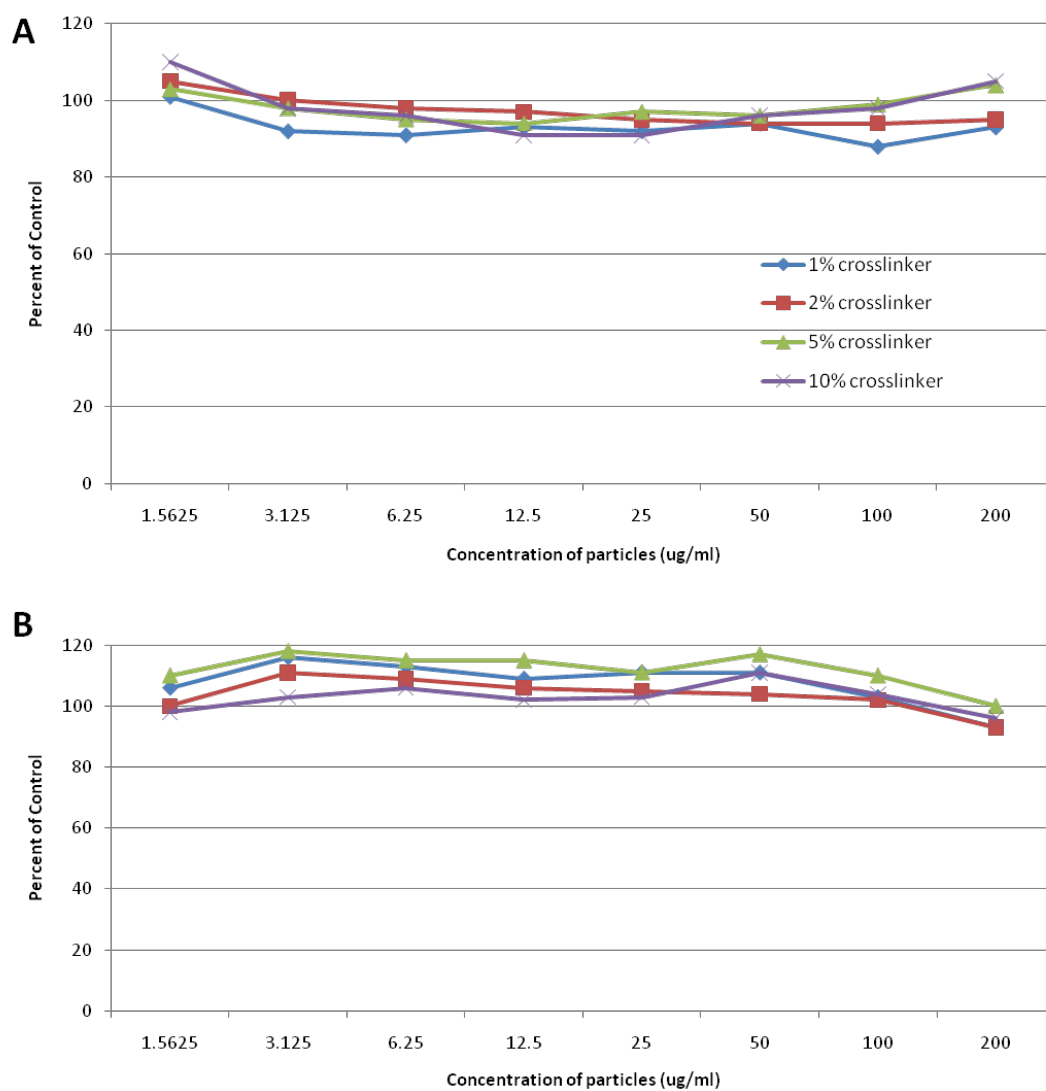


Figure 2.9. The dose dependant cell viability of HUVEC (endothelial) cells when dosed with HEA-based RBCMs with varied crosslink density (1-10%) after 72 hours of incubation with the particles as determined by MTS (A) and ATP/luciferase (B) assays as a percent of saline-dosed control.

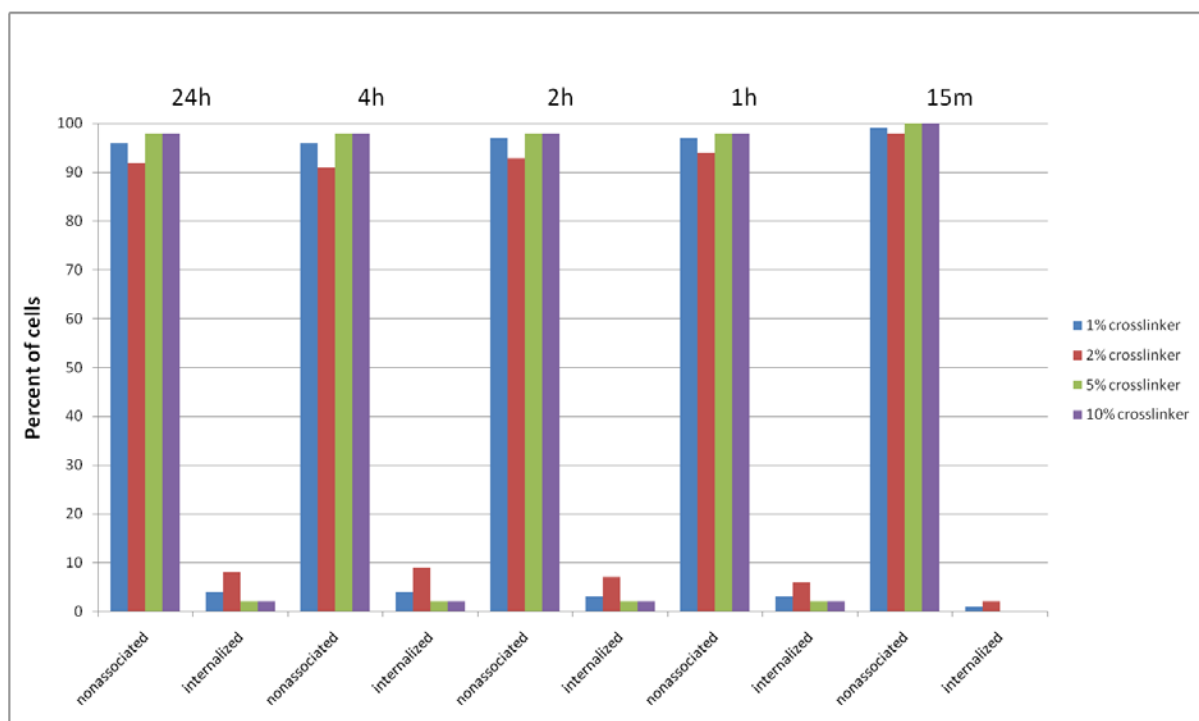


Figure 2.10. Uptake of 1, 2, 5, and 10% crosslinked RBCMs in HUVEC cells after dosing times from 15 minutes to 24 hours based on flow cytometry. Results are expressed in terms of the percentage of cells which had taken up RBCMs (internalized) and which were free of RBCMs (unassociated).

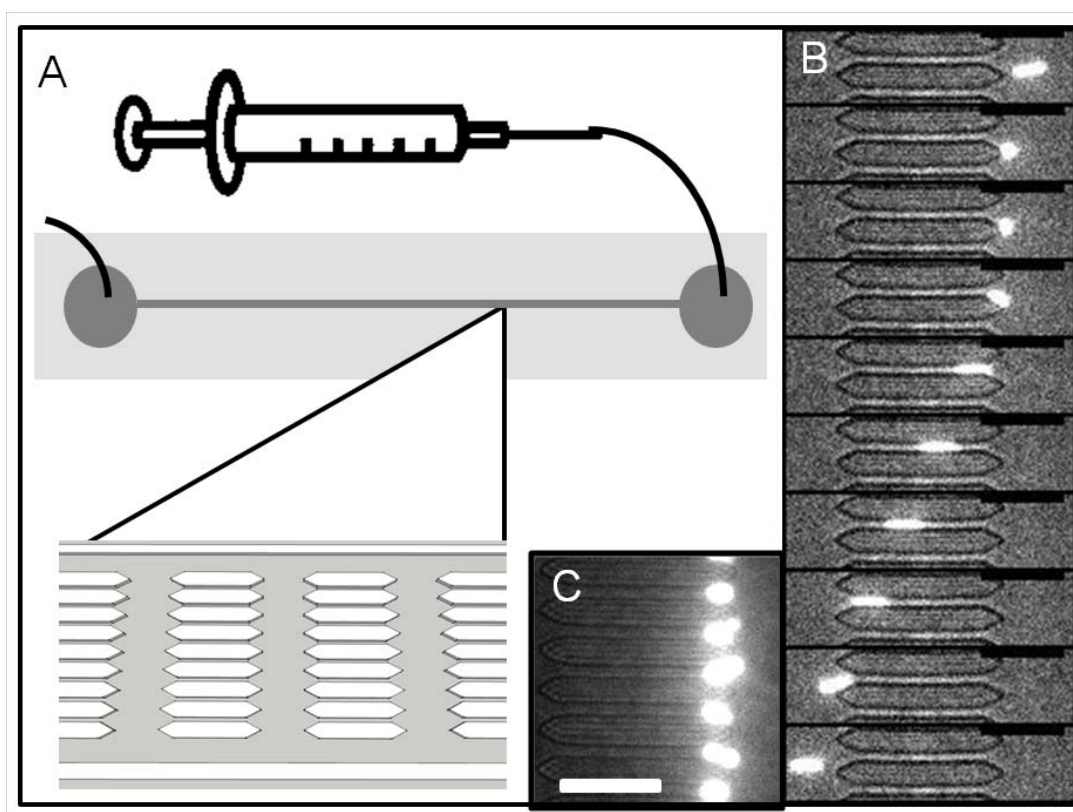


Figure 2.11. Microfluidic evaluation of RBCM deformability. (A) A schematic of the microfluidic devices. The channel has a repeating pattern of 50 μm long pores which are 3 μm wide and 3.5 μm tall, forcing particles passed through the device to deform. Flow was driven by a syringe pump. (B) An image sequence showing a 1% crosslinked RBCM (6.0 μm diameter) deforming to pass through a 3 x 3.5 μm channel (25 ms between frames). (C) 10% crosslinked RBCMs stuck in the entrance of the 3 μm pores in a microfluidic device. Scale bars are 30 μm .

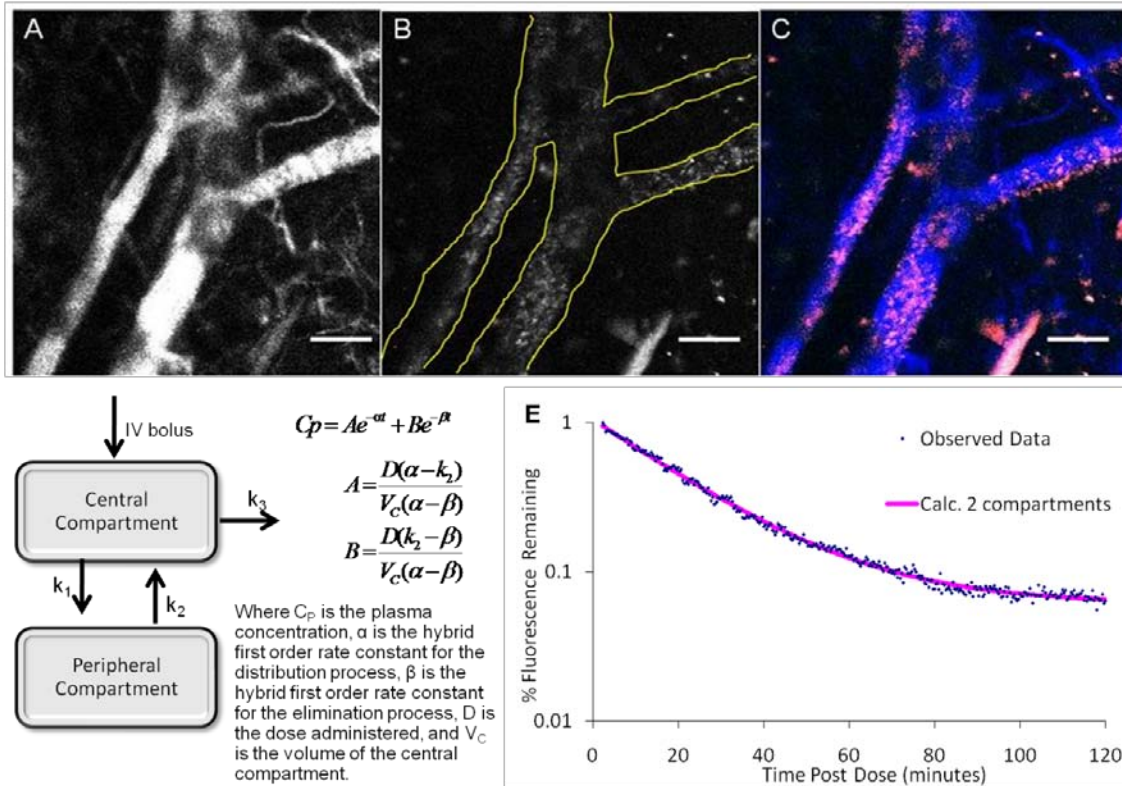


Figure 2.12. Intravital microscopy data and compartmental analysis. (A) Vasculature highlighted with rhodamine B labeled dextran prior to injection of RBCMs. (B) Dylight 680 labeled 1% cross-linked RBCMs flowing through this stretch of vasculature 20 minutes after dosing, with ROI outlined in yellow. (C) Colored overlay of A and B, with dextran in blue and particles shown in red. Scale bars are 100 μ m. (D) Two-compartment model schematic and governing equations for the model applied to the data. (E) Decrease in fluorescent signal in the ROI for the 2 hour scan in this mouse. The semi-log plot shows calculated fit for the two compartment pharmacokinetic models.

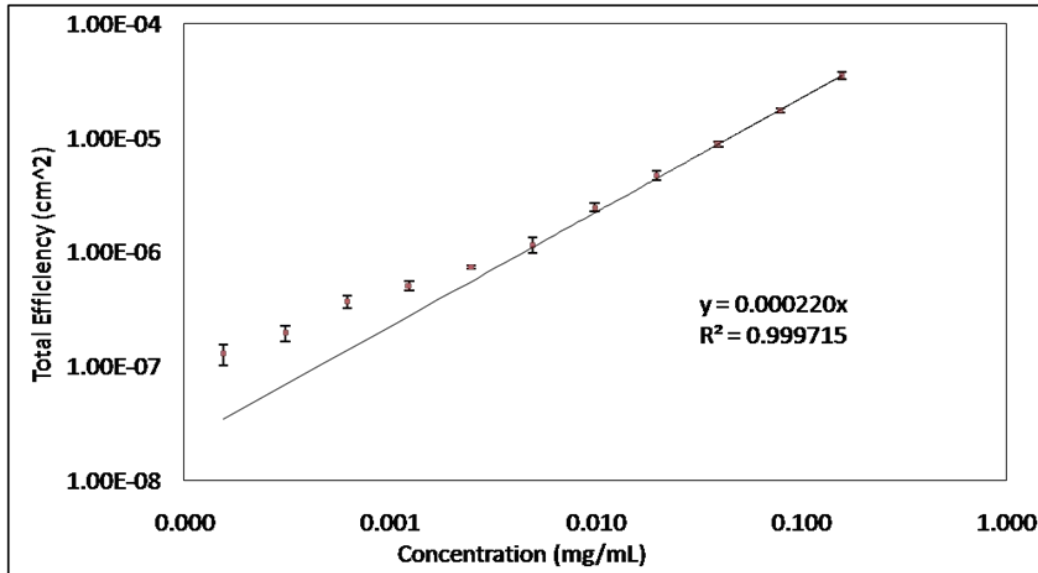


Figure 2.13. A standard curve which correlates fluorescent efficiency (signal intensity) and concentration of 1% crosslinked RBCMs in whole blood. Deviation from linearity defines the lower limit of quantification for fluorescent signal. Data collected for the blood draw experiments fell within the linear range of this plot. Scale bars represent one standard deviation, with $n=3$.

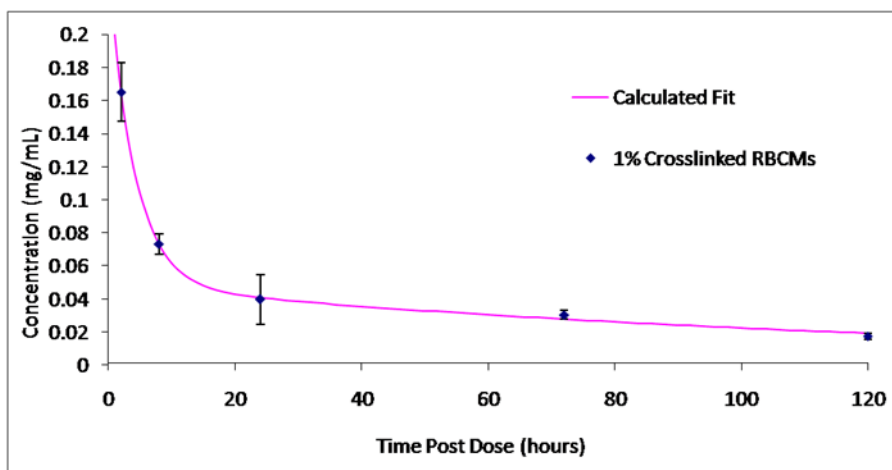


Figure 2.14. A plot of particle concentration in whole blood over time for 1% crosslinked RBCMs where $n=4$ for each data point. A two compartment pharmacokinetic model with elimination from the central compartment was fit to the data (red) by nonlinear regression analysis. The fit was used to calculate pharmacokinetic parameters for these particles. Scale bars represent one standard deviation, with $n=3$.

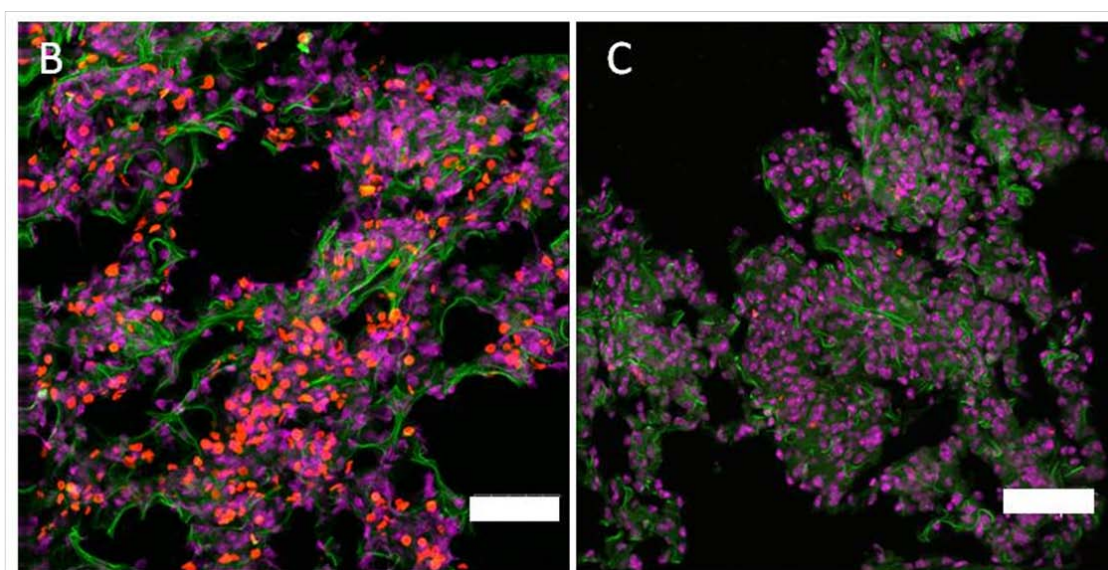
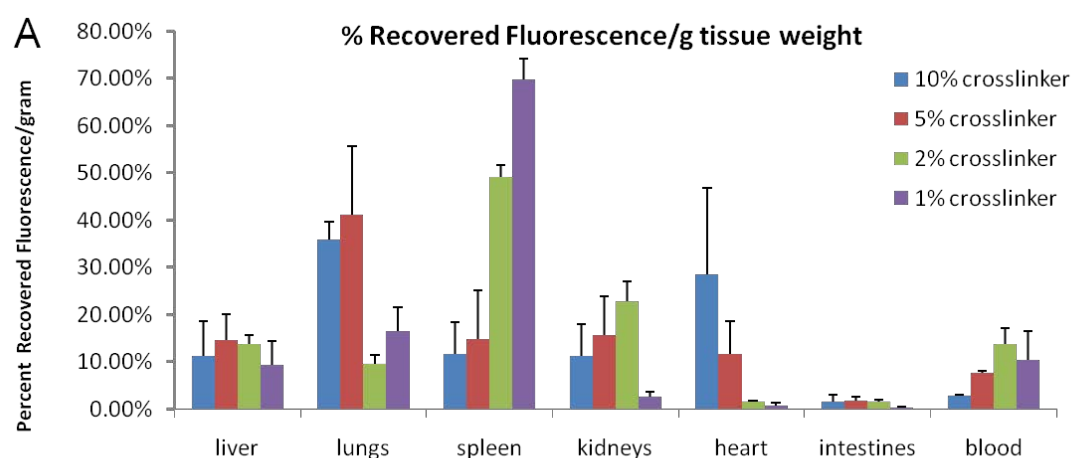


Figure 2.15. Biodistribution of RBCMs. (A) Distribution of RBCMs into various tissues 2 hours post dosing by percent recovered fluorescence normalized for tissue weight. Error bars represent one standard deviation, with $n=3$ for each case. (B) Lung tissue from a mouse dosed with 10% cross-linked RBCMs. Particles are shown in red, with cell nuclei in purple and cytoskeleton (F-actin) stained green. (C) Lung tissue from a mouse dosed with 1% cross-linked RBCMs, with tissue stained as in (B). Very few RBCMs were in this tissue compared to mice dosed with more rigid particles, consistent with the tissue distribution data. Scale bars are 50 μm .

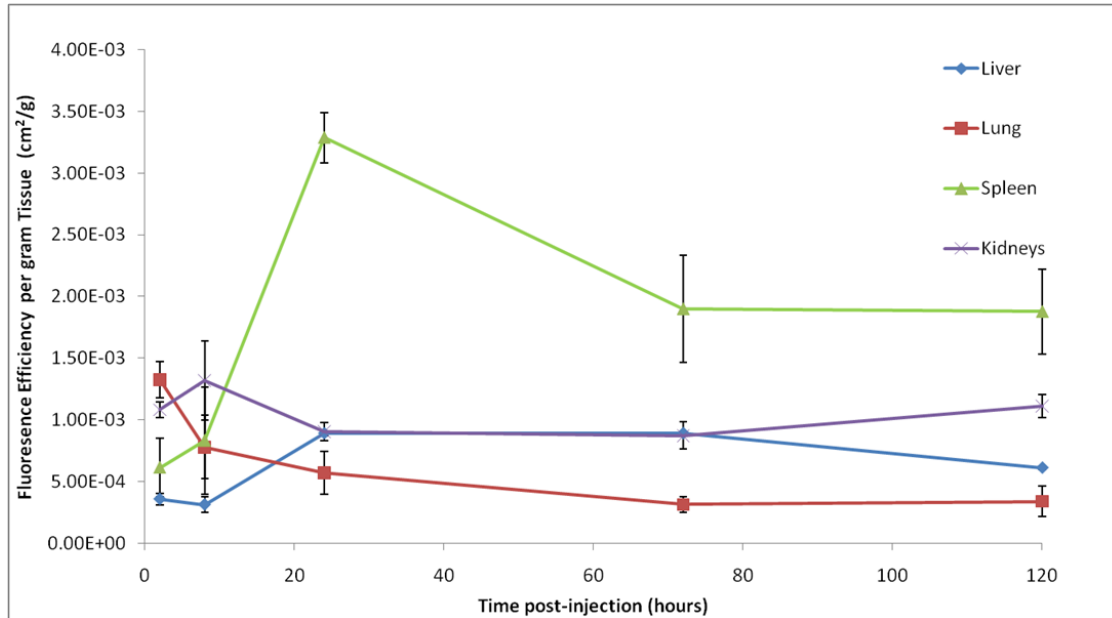


Figure 2.16. A plot showing the biodistribution of 1% crosslinked RBCMs in mice over a 2-120 hour time course in the liver, lung, spleen and kidneys. Data is presented as fluorescent efficiency per gram of tissue weight. Error bars represent one standard deviation, with n=3 for each case.

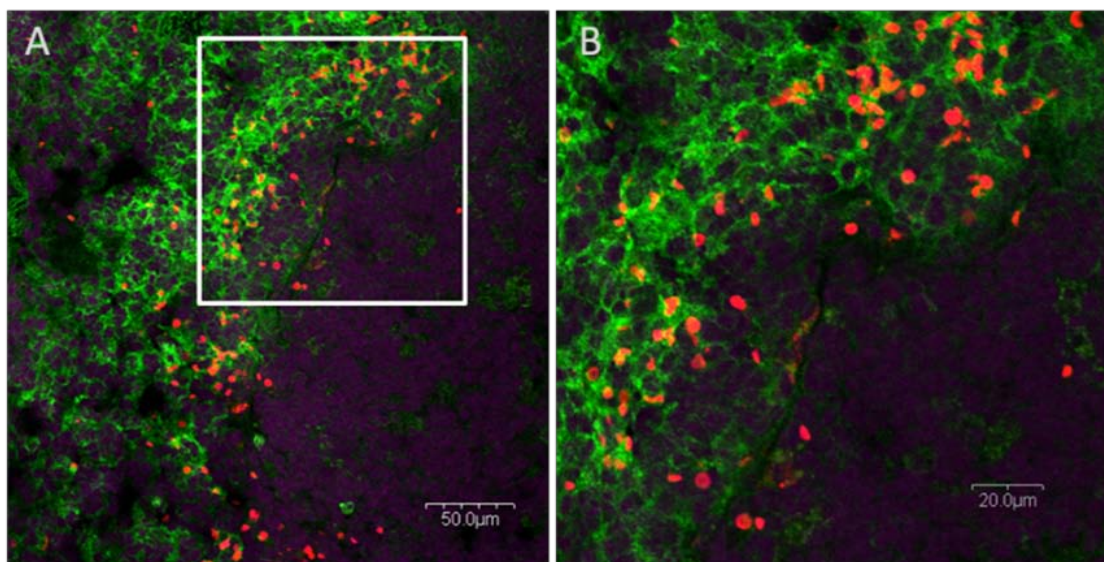


Figure 2.17. Histological analysis of spleen tissue from RBCM dosed mice. (A) Overlaid image of immunostained spleen tissue from a mouse dosed with 2% cross-linked RBCMs. The particles (red) are primarily sequestered in the red pulp, an area of tissue which is rich in macrophages (green). Cell nuclei are shown in purple. (B) An enlarged view of the area indicated in (A) by a grey square.

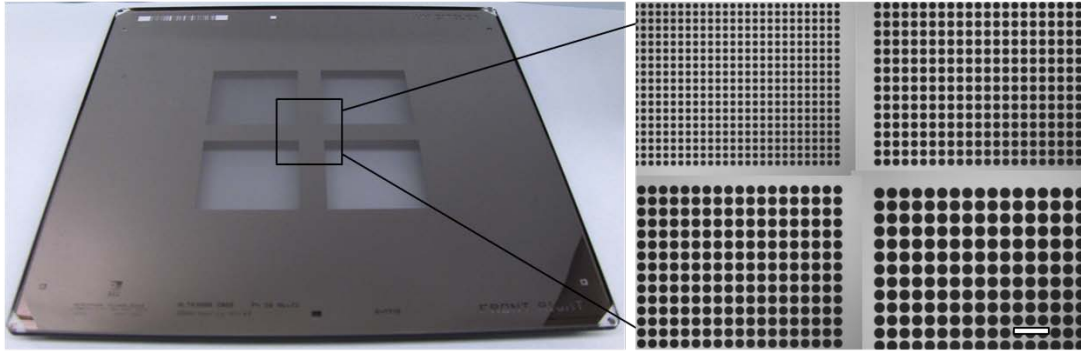


Figure 2.18. Left: A chrome on quartz reticle designed for fabrication of master templates with micron sized discoid features. Right: Bright field microscopy images of the patterned sections of the reticle at 100x magnification (scale bar is 20 μm).

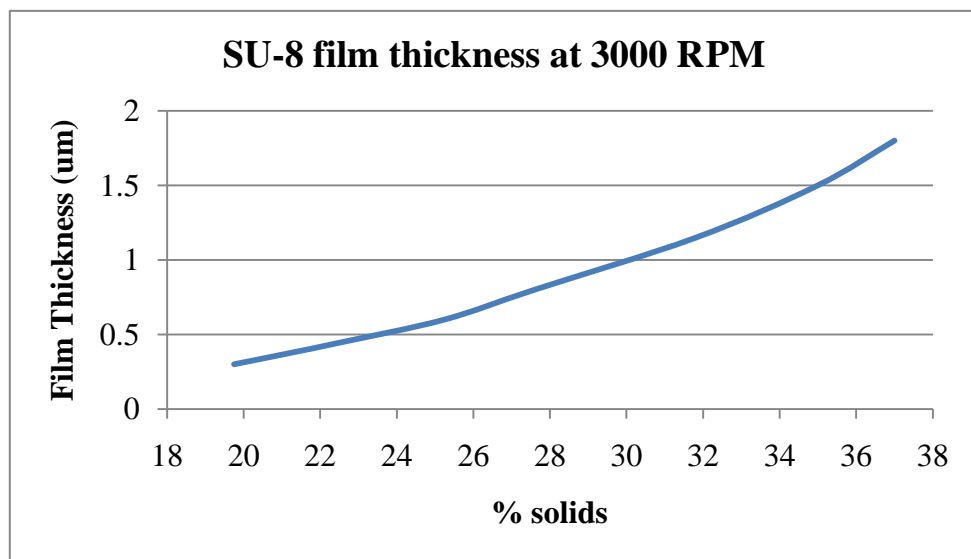


Figure 2.19. A plot showing SU-8 film thickness as a function of weight percent solids of SU-8 2010 when diluted from the original 58% solids with SU-8 thinner. Film were spin coated at 3000 rpm for 30 seconds. Thickness measurements were made based on post-exposure feature heights.

2.5 References

- (1) Alexis, F.; Pridgen, E.; Molnar, L. K.; Farokhzad, O. C. *Mol Pharm* **2008**, *5*, 505.
- (2) Canelas, D. A.; Herlihy, K. P.; DeSimone, J. M. *Wiley Interdiscip Rev Nanomed Nanobiotechnol* **2009**, *1*, 391.
- (3) Kohane, D. S. *Biotechnol Bioeng* **2007**, *96*, 203.
- (4) Merkel, T. J.; Herlihy, K. P.; Nunes, J.; Orgel, R. M.; Rolland, J. P.; Desimone, J. M. *Langmuir* **2009**.
- (5) Geng, Y.; Dalhaimer, P.; Cai, S.; Tsai, R.; Tewari, M.; Minko, T.; Discher, D. E. *Nat Nanotechnol* **2007**, *2*, 249.
- (6) Gratton, S. E.; Ropp, P. A.; Pohlhaus, P. D.; Luft, J. C.; Madden, V. J.; Napier, M. E.; DeSimone, J. M. *Proc Natl Acad Sci U S A* **2008**, *105*, 11613.
- (7) Mitragotri, S.; Lahann, J. *Nat Mater* **2009**, *8*, 15.
- (8) Champion, J. A.; Katare, Y. K.; Mitragotri, S. *J Control Release* **2007**, *121*, 3.
- (9) Banquy, X.; Suarez, F.; Argaw, A.; Rabanel, J.; Grutter, P.; Bouchard, J.; Hildgen, P.; Giasson, S. *Soft Matter* **2009**, *5*, 3984.
- (10) Fox, M. E.; Szoka, F. C.; Frechet, J. M. *Acc Chem Res* **2009**, *42*, 1141.
- (11) Haghgooie, R.; Toner, M.; Doyle, P. S. *Macromol. Rapid Commun.* **2009**, *31*, 128.
- (12) Doshi, N.; Zahr, A. S.; Bhaskar, S.; Lahann, J.; Mitragotri, S. *Proc Natl Acad Sci U S A* **2009**, *106*, 21495.
- (13) Hendrickson, G. R.; Lyon, L. A. *Angew Chem Int Ed Engl* **2010**, *49*, 2193.
- (14) Kabanova, S.; Kleinbongard, P.; Volkmer, J.; Andree, B.; Kelm, M.; Jax, T. W. *Int J Med Sci* **2009**, *6*, 156.

- (15) Fung, Y. C. *Biomechanics Mechanical Properties of Living Tissues*; 2 ed.; Springer-Verlag Inc.: New York, 1993.
- (16) *The Complete Spleen. Structure, Function, and Clinical Disorders*; 2 ed.; Bowdler, A. J., Ed.; Humana Press Inc.: Totowa, 2002.
- (17) Suresh, S. *Nat Nanotechnol* **2007**, 2, 748.
- (18) Suresh, S. *Acta Biomater* **2007**, 3, 413.
- (19) Gratton, S. E.; Pohlhaus, P. D.; Lee, J.; Guo, J.; Cho, M. J.; Desimone, J. M. *J Control Release* **2007**, 121, 10.
- (20) Arifin, D. R.; Palmer, A. F. *Artif Cells Blood Substit Immobil Biotechnol* **2005**, 33, 137.
- (21) Sakai, H.; Takeoka, S.; Park, S. I.; Kose, T.; Nishide, H.; Izumi, Y.; Yoshizu, A.; Kobayashi, K.; Tsuchida, E. *Bioconjug Chem* **1997**, 8, 23.
- (22) Durocher, J.; Payne, R.; Conrad, M. *Blood* **1975**, 45, 11.
- (23) Wolf, H.; Marschall, F.; Scheffold, N.; Clausen, M.; Schramm, M.; Henze, E. *European Journal of Nuclear Medicine and Molecular Imaging* **1993**, 20, 297.
- (24) Dulinska, I.; Targosz, M.; Strojny, W.; Lekka, M.; Czuba, P.; Balwierz, W.; Szymonski, M. *J Biochem Biophys Methods* **2006**, 66, 1.
- (25) Rolland, J. P.; Maynor, B. W.; Euliss, L. E.; Exner, A. E.; Denison, G. M.; DeSimone, J. M. *J Am Chem Soc* **2005**, 127, 10096.
- (26) Snyder, G. K.; Weathers, W. W. *J Appl Physiol* **1977**, 42, 673.
- (27) Nguyen, K. T.; West, J. L. *Biomaterials* **2002**, 23, 4307.
- (28) Rehfeldt, F.; Engler, A. J.; Eckhardt, A.; Ahmed, F.; Discher, D. E. *Adv Drug Deliv Rev* **2007**, 59, 1329.

- (29) Fattorossi, A.; Nisini, R.; Pizzolo, J. G.; D'Amelio, R. *Cytometry* **1989**, *10*, 320.
- (30) Shevkoplyas, S. S.; Yoshida, T.; Gifford, S. C.; Bitensky, M. W. *Lab Chip* **2006**, *6*, 914.
- (31) Cho, Y.; De Bruyn, P. P. *Am J Anat* **1975**, *142*, 91.
- (32) McWhirter, J. L.; Noguchi, H.; Gompfer, G. *Proc Natl Acad Sci U S A* **2009**, *106*, 6039.
- (33) Li, J.; Lykotrafitis, G.; Dao, M.; Suresh, S. *Proc Natl Acad Sci U S A* **2007**, *104*, 4937.
- (34) Park, Y.; Best, C. A.; Badizadegan, K.; Dasari, R. R.; Feld, M. S.; Kuriabova, T.; Henle, M. L.; Levine, A. J.; Popescu, G. *Proc Natl Acad Sci U S A*, *107*, 6731.
- (35) Sandanaraj, B. S.; Gremlich, H. U.; Kneuer, R.; Dawson, J.; Wacha, S. *Bioconjug Chem* **2010**, *21*, 93.
- (36) Smith, B. R.; Cheng, Z.; De, A.; Koh, A. L.; Sinclair, R.; Gambhir, S. S. *Nano Lett* **2008**, *8*, 2599.
- (37) Neubauer, A. M.; Sim, H.; Winter, P. M.; Caruthers, S. D.; Williams, T. A.; Robertson, J. D.; Sept, D.; Lanza, G. M.; Wickline, S. A. *Magn Reson Med* **2008**, *60*, 1353.
- (38) Brown, A. M. *Comput Methods Programs Biomed* **2001**, *65*, 191.
- (39) Janssen, B.; Debets, J.; Leenders, P.; Smits, J. *Am J Physiol Regul Integr Comp Physiol* **2002**, *282*, R928.
- (40) Van Rooijen, N.; Sanders, A. *Journal of Immunological Methods* **1994**, *174*, 83.
- (41) Zhang, H.; Zeng, X.; Li, Q.; Gaillard-Kelly, M.; Wagner, C. R.; Yee, D. *British Journal of Cancer* **2009**, *101*, 71.

- (42) Kennel, S. J.; Woodward, J. D.; Rondinone, A. J.; Wall, J.; Huang, Y.; Mirzadeh, S. *Nuclear Medicine and Biology* **2008**, *35*, 501.
- (43) Oldenborg, P.-A.; Zheleznyak, A.; Fang, Y.-F.; Lagenaur, C. F.; Gresham, H. D.; Lindberg, F. P. *Science* **2000**, *288*, 2051.
- (44) Lindberg, F.; Lublin, D.; Telen, M.; Veile, R.; Miller, Y.; Doniskeller, H.; Brown, E. *J Biol Chem* **1994**, *269*, 1567.
- (45) Jaiswal, S.; Jamieson, C. H. M.; Pang, W. W.; Park, C. Y.; Chao, M. P.; Majeti, R.; Traver, D.; van Rooijen, N.; Weissman, I. L. *Cell* **2009**, *138*, 271.
- (46) Tsai, R. K.; Rodriguez, P. L.; Discher, D. E. *Blood Cells, Molecules, and Diseases* **2010**, *45*, 67.
- (47) Bissell, D. M.; Gores, G. J.; Laskin, D. L.; Hoofnagle, J. H. *Hepatology* **2001**, *33*, 1009.
- (48) Lee, W. M.; Senior, J. R. *Toxicologic Pathology* **2005**, *33*, 155.
- (49) Kelly, J. Y.; DeSimone, J. M. *J Am Chem Soc* **2008**, *130*, 5438.
- (50) Elif, V.; Ali, U. *J. Polym. Sci., Part A: Polym. Chem.* **2005**, *43*, 3957.
- (51) Tong, L.; He, W.; Zhang, Y.; Zheng, W.; Cheng, J. X. *Langmuir* **2009**, *25*, 12454.
- (52) Pharsight *WinNonlin User's Guide*, 2008.

Chapter 3

Pharmacokinetics and Biodistribution of Low Modulus Hydrogel Particles

3.1 Introduction

Crosslinked hydrophilic polymers called hydrogels possess a number of properties which make them an important class of biomaterials for use in biotechnology and medicine. The presence of chemical crosslinks in these polymer networks render the hydrophilic polymer components insoluble in water, providing structure and physical integrity to the gels¹. Because of the hydrophilic nature of their constituent polymers, hydrogels can swell to encompass large amounts of water without dissolution². The high water content of hydrogels makes them soft and rubbery; physical characteristics similar to those of soft tissues³. Many hydrogels exhibit excellent biocompatibility, likely as a result of their high water content, causing minimal inflammatory responses, thrombosis, and tissue damage^{1,4-6}. The swollen structure and porous nature of hydrogels gives them high permeability to oxygen and water soluble metabolites - appealing attributes for use in contact lenses, and other membrane-related applications⁷. Hydrogels have several advantageous properties which are being exploited for medical applications to direct behavior of the gel *in vivo*. Many hydrogel properties are controlled to a large extent by the crosslink density of the gels, including the swelling, cargo release profile and stiffness of the gels^{2,8}. Because of these properties and their facile control, hydrogels of a range of structures have found use in medical applications ranging from biosensor coatings^{9,10}, drug delivery agents^{2,8}, and tissue engineering¹¹.

Recently, increasing attention has been given to the fabrication and characterization of extremely deformable hydrogel particles, with many studies demonstrating the role played by particle deformability in the interaction of particles and biological systems. In a study using poly acrylamide microparticles crosslinked with either 0.2 % (rigid) or 0.05 % (soft)

bisacrylamide, macrophages showed a strong preference for phagocytosis of rigid particles versus soft ones, suggesting that macrophages may use the rigidity of a particle as an indicator to initiate phagocytosis¹². A study comparing hydrogel particles with their elasticity (Young's modulus) varied by changing crosslink density found that the endocytotic mechanism was dependant on the elasticity of the nanoparticle, with softer particles internalized preferentially by macropinocytosis while hard-sphere uptake involves clathrin-mediated routes¹³. Low modulus microgel particles were able to traverse pores which were 1/10 their diameters under pressures relevant to renal filtration, suggesting a clearance mechanism for deformable nanoparticles¹⁴. Microparticles resembling red blood cells were more readily able to traverse microfluidic channels which mimicked the constrictions of capillaries when crosslink density was lowered^{15,16}.

Our previous work demonstrated that hydrogel particles based on lightly crosslinked 2-hydroxyethyl acrylate (HEA) which resembled red blood cells in size and shape with decreasing crosslink density had dramatically altered behavior *in vivo* in a mouse model. Particles made from this hydrogel material with a Young's modulus of 7.8 kPa were eliminated from the circulation over 30 times slower than particles which were only moderately (approximately 8x) stiffer (63.9 kPa), presumably due to avoidance of filtration in the capillary beds of the lungs, and to some extent, the spleen¹⁶. The most elastically soft particles demonstrated the ability to deform to bypass physical barriers encountered in the circulation. Because even slightly less elastic particles (modulus of 16.9 kPa) had greatly reduced circulation times, a modulus-based threshold for 6 μ m diameter particles to avoid filtration *in vivo* was inferred.

While flexible particles have been shown to have some advantageous *in vivo* properties, relatively few studies have focused on the *in vivo* behavior of very deformable particles. The rigidity of hydrogels is typically tuned by adjusting the amount of crosslinker. While this method provides fairly facile control of hydrogel modulus, increased swelling with decreasing crosslink density results in difficulty in maintaining identical particle size and size distribution with changing crosslink density for most particle fabrication methods³. However, with the PRINT® (particle replication in non-wetting templates) method, the size and/or shape of the elastomeric molds can be varied to maintain the size of hydrated particles made with varying compositions. In this study, the behavior of monodisperse populations of extremely soft hydrogel particles was probed as particle size was varied in the micron range while composition and modulus were maintained as constants.

Herein the *in vivo* behavior of lightly crosslinked hydrogel particles with identically low modulus were examined as particle size varies. A series of acrylic monomers with short PEG side chains were fabricated to facilitate particle making with the PRINT process and for the fabrication of low modulus hydrogels. It was determined that a PEG chain length of three repeat units, derived from triethyleneglycol, yielded crosslinked hydrogels with optimal properties. This monomer was used to fabricate PRINT particles from 1, 2 and 3 μm diameter molds. Using the mechanical properties of the longest circulating, HEA-based hydrogels from Chapter 2 as a target (elastic modulus ~ 8 kPa), hydrogel particles were fabricated via the PRINT® method with a similarly low modulus. The *in vivo* circulation profile and biodistribution of these extremely deformable particles was examined.

3.2 Results and Discussion

3.2.1 Hydroxy PEG Acrylate Monomers

While previous work focused on low modulus (<10 kPa) hydrogels based on HEA, this monomer was less than ideal for the PRINT process when translated to smaller sized molds. Small molecule monomers have the potential to interfere with the efficacy of particle molding methods like PRINT in two main ways. Solvent absorption into the mold material may cause a change in the size of the mold due to swelling of the mold material, and may also cause significant underfilling prior to the curing step. However, due to the fluorinated nature of the mold material used in the PRINT process, HEA is not absorbed to a significant extent, and this mechanism was unlikely to have an effect¹⁷. When particle size decreases, the surface area to volume ratio of the mold features increases, allowing evaporation to become a factor. Evaporation of the monomer would lead to underfilled molds and an increase in non-volatile components in the preparticle mixture (such as the PEGDA crosslinker). Thus, particles consisting primarily of HEA were only successfully molded with diameters of 2 μm or greater while using chilled equipment to mediate evaporative effects¹⁶. An increase in the molecular mass of the monomer serves to decrease this evaporative effect through a reduction of the vapor pressure of the monomer.

To increase the molecular weight of the monomer, PEG modified acrylics (HPAs) were synthesized with varying short-chain ($n = 2, 3$, or 4) PEG groups, essentially extending the side-chain of a HEA-like acrylic (**Figure 3.1**). Rigorous purification of the HPA monomers was necessary to remove all of the diacrylate crosslinker, and cold storage ensured that the transesterified diacrylate did not reform *in situ*. The properties of crosslinked hydrogels derive not just from the crosslink density of the gels, but also from the properties

of the main-chain polymer and the amount of water uptake or swelling². As the PEG side-chain grows in length, the steric bulk should begin to hinder the rotation of the polymer, rendering it stiffer. In terms of water uptake, as the PEG character of a gel increases, the hydrophilicity of the gel should increase as well.

To determine the mechanical properties of the bulk hydrogels, bulk samples were hydrated in deionized water overnight. The mechanical properties of the hydrated hydrogels were determined using an Instron 5556 Universal Testing Machine (Instron) with a strain rate of 5 mm/min. Bulk samples of hydrogels made with 1% PEG₄₀₀₀Diacrylate crosslinker (PEG₄₀₀₀DA) and the HPA derived from triethylene glycol (HP₃A) provided the lowest modulus HPA hydrogels (**Table 3.1**). Though HP₄A hydrogels should have a greater hydrophilic character than HP₃A hydrogels, the longer PEG chain resulted in decreased water

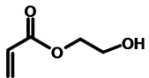
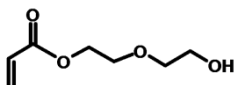
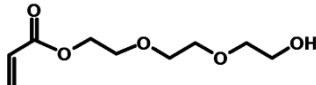
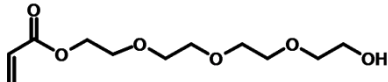
Monomer		E (kPa)	% strain at break	Swelling ratio, weight	Swelling ratio, length
HEA		10 ± 1.6	270	13.6	2.9
HP ₂ A		103 ± 8.6	60	5.8	1.9
HP ₃ A		20 ± 1.7	83	10.9	2.4
HP ₄ A		36 ± 4.8	52	8.8	2.2

Table 3.1. Properties of lightly crosslinked hydrogels composed of different acrylic monomers containing 1% of a 4,000 g/mol PEG diacrylate crosslinker and 1% of HCPK photoinitiator, hydrated for 12 hours in deionized water at room temperature. Monomers are shown with increasing PEG chain length.

uptake. This may be an effect of increased stiffness of the main chain making unentanglement, and greater swelling, difficult. Interestingly, HEA hydrogels, though incompatible with PRINT at smaller particle sizes, had the most desirable properties, with lower modulus and greater elasticity than the HPA hydrogels.

3.2.2 Low Modulus HP₃A Hydrogels

Based on previous work with low modulus hydrogels¹⁶, an elastic modulus of ≤ 10 kPa was targeted for HP₃A based hydrogels, requiring a drop in crosslink density compared to the hydrogels used to evaluate the effect of PEG side-chain length. With deformability similar to that of red blood cells (15-26 kPa)^{18,19}, a modulus in the target range should be sufficient to show a large effect on particle circulation with 6 μ m diameter particles. An acid containing monomer (2-carboxyethyl acrylate, CEA) was included in the hydrogel monomer mixture at 10 % (by weight) to give the particles a negative charge, thereby decreasing non-specific particle uptake²⁰. Bulk samples of HP₃A hydrogels containing 10% CEA monomer, 1% 1-hydroxycyclohexyl phenyl ketone photoinitiator and crosslinked with PEG₄₀₀₀DA were hydrated in pH 7.4 PBS to simulate physiological conditions and tested with the Instron tensometer (**Table 3.2**). Hydrogels with 0.05% PEG₄₀₀₀DA crosslinker had the desired properties, with a Young's modulus of 6.5 ± 1.3 kPa.

% crosslinker (weight)	1	0.5	0.05
E (kPa)	17 ± 2.2	13 ± 1.6	6.5 ± 1.3
% strain at break	53 ± 19	46 ± 7	43 ± 7.5
Swelling ratio (wt)	11.9	12.8	30.0
Swelling ratio (length)	2.4	2.6	3.5

Table 3.2. Mechanical properties of hydroxyl PEG₃ Acrylate (HP₃A) hydrogels with varying amounts of PEG₄₀₀₀diacrylate crosslinker and 10% of 2-carboxyethyl acrylate. Swelling ratios were determined from one bulk sample hydrated for 24 hours in PBS. Modulus and strain at break represent an average value determined from three samples cut from the bulk gel, with error representing one standard deviation.

3.2.3 Fabrication and Characterization of HP₃A Hydrogel PRINT Particles

HP₃A hydrogels containing 10% CEA monomer, 1% 1-hydroxycyclohexyl phenyl ketone (HCPK) photoinitiator, 0.05% PEG₄₀₀₀DA crosslinker, and fluorescent dyes, including 1% Dylight₆₈₀ maleimide for *in vivo* imaging, and 0.1% methacryloxyethyl thiocarbonyl rhodamine B for ease of particle analysis (**Table 3.3**). Particles were fabricated using PRINT molds with feature diameters of 1, 2 and 3 μm , resulting in hydrated diameters of 3.79 ± 0.17 , 6.39 ± 0.56 , and 8.88 ± 0.47 μm in PBS, respectively (**Table 3.4**).

Monomer	(%)
HP ₃ A	87.85
2-carboxyethyl acrylate	10
PEG ₄₀₀₀ Diacrylate	0.05
1-hydroxycyclohexyl phenyl ketone	1
methacryloxyethyl thiocarbonyl rhodamine B	0.1
Dylight ₆₈₀ maleimide	1

Table 3.3. The composition of hydrogel particles fabricated for *in vivo* work.

Fluorescent microscopy was used to measure the diameter of hydrated particles (n=50). The zeta potential of the particles was approximately -20 mV in all cases. The particles were suspended in 0.1% 2,000 g/mol poly (vinyl alcohol) in PBS for in vivo applications. Fluorescent images of the particles can be seen in Figure 3.3.

Mold diameter	Particle Diameter	Zeta Potential
1 μm	$3.79 \pm 0.17 \mu\text{m}$	$-22.1 \pm 5.7 \text{ mV}$
2 μm	$6.39 \pm 0.56 \mu\text{m}$	$-17.6 \pm 10.8 \text{ mV}$
3 μm	$8.88 \pm 0.47 \mu\text{m}$	$-22.9 \pm 7.47 \text{ mV}$

Table 3.4. Characterization of particles fabricated for in vivo studies. Particle diameters were determined by microscopy. Error represents one standard deviation from the mean with n=50 for particle diameters.

3.2.4 *In vivo* Studies

To examine the distribution and clearance profile of the particles, female Balb/c mice were injected intravenously at a dose of 20 mg particles/kg of body weight. The mice were sacrificed at time points of 0.2, 0.5, 1, 3, 7, 25, 56, and 104 hours post-dose and the tissues analyzed for fluorescent signal from the particles (**Figures 3.4 and 3.5**). The tissues were not perfused prior to analysis.

The smallest particles (hydrated diameter 3.8 μm) distributed primarily into the spleen and lungs immediately after injection. While signal in the lungs decreased after injection, signal in the spleen increased, peaking at 3 hours and staying fairly constant or slightly decreasing over the next 101 hours. These particles accumulated to some extent in the liver over the course of the study, with signal peaking 24 hours after injection and decreasing slightly thereafter. Liver accumulation was minor when viewed on a per gram basis (**Figure 3.4**). Accumulation in the kidneys, heart, and muscle tissue remained low at

all times, decreasing over the course of the scan, possibly due to the small amount of blood remaining in these tissues. Particles were cleared to low, but still measurable, levels in the blood by the final time-point examined, with 2.9% of the injected dose in the blood at 104 hours.

Particles with 6.4 μm diameters distributed primarily into the spleen and lungs immediately after injection with a profile similar to what we observed in previous studies with low modulus particles of this size¹⁶. Signal in the lungs decreased after injection to low levels. Signal in the spleen and liver increased after injection, with signal in the spleen peaking at 3 hours and the signal in the liver peaking later, 7 hours after injection. Signal in the spleen dipped at the 24 hour time-point, correlating to an increase in signal in the blood. This effect may have been due to the release of particles from the spleen back into the circulation. Accumulation in the kidneys, heart, and muscle tissue remained low at all times, decreasing over the course of the scan, possibly due to the small amount of blood remaining in these tissues. At the final time-point examined, 104 hours post-dose, 9.2% of the injected dose remained in the blood.

The largest particles, with hydrated diameter of 8.8 μm , were sequestered primarily in the lungs after injection, likely due to their large size compared to the diameter of the capillary beds in this tissue, and only low amounts of particles remained in the circulation. Particles cleared from the lungs over the course of the study, with accumulation in the spleen and liver increasing over time. Liver accumulation was the most significant for these larger particles compared to the other sizes examined, especially when viewed on a per gram basis. As with the 6.4 μm diameter particles, a dip in the amount of particles in the spleen and a corresponding increase in the blood occurred. For these larger particles, this effect was more

dramatic, and happened earlier in the study (7 hours post-dose). These particles were cleared from the blood to below their lower limit of quantification after the 7 hour time point (< 4.4 % of the injected dose).

3.2.5 Pharmacokinetics of Particle Clearance from Blood

Particle concentration in the blood was determined from blood drawn via cardiac puncture at each time-point. Serial dilutions of particles in freshly drawn mouse blood allowed for the generation of standard curves which correlated fluorescent signal in whole blood to particle concentration. The signal from blood harvested from dosed mice fell within the linear region of these plots in most cases, with late time-points falling below quantification limits (where the plot deviated from linearity) for the case of the 8.8 μm particles. A plot of particle concentration in whole blood over time for the three particles is shown in **Figure 3.6**.

To evaluate the kinetics of clearance for the 3.8 and 6.4 μm diameter particles, we used a two compartment pharmacokinetic model, characterized by a bi-exponential decrease in particle concentration over time ²¹, with parameters fit by non-linear regression analysis ²². This model describes an initial (distribution) phase where the particles distribute from the plasma into various tissues, followed by a late (elimination) phase that describes the ultimate clearance of particles from the plasma. For small molecules and nanoparticles the distribution is attributed to extravasation into tissue; because of their size, the distribution of our hydrogel microparticles may be due to physical entrapment in constricted capillaries (as in the lung) or tissues with low blood flow (such as the spleen) rather than by an extravasation process.

Both particles had similar pharmacokinetics of clearance, with much of the dose distributing to tissues rapidly after injection and slow elimination half-lives. Elimination half-life ($\beta t_{1/2}$) for 3.8 μm particles (59.55 h) was shorter than for the red blood cell- (RBC) sized 6.4 μm particles (85.49 h), suggesting that this size may be crucial to the long circulation times of RBCs. Additionally, the area under the curve (AUC), was more than 3 times greater for the RBC sized particles than the smaller hydrogels (8.513 and 2.498 $\text{mg}\cdot\text{hr}/\text{mL}$, respectively), indicating that a greater amount of particles stayed in the circulation over time. Parameters calculated with this model can be seen in Table 3.5.

The circulation profile of the largest particles examined in this study (8.8 μm) was not analyzed with a pharmacokinetic model because these were rapidly cleared below the limits

Particle Diameter (μm)	3.79 \pm 0.17	6.39 \pm 0.56
A (mg/mL)	0.152	0.109
B (mg/mL)	0.0268	0.0682
α (hr^{-1})	0.765	1.076
β (hr^{-1})	0.0116	0.00810
$\alpha t_{1/2}$ (hr)	0.906	0.644
$\beta t_{1/2}$ (hr)	59.551	85.488
V_c (mL)	2.248	2.262
AUC (mg*hr/mL)	2.498	8.513
CL_T (mL/hr)	0.160	0.0470
Vd_β (mL)	12.684	5.727

Table 3.5. Pharmacokinetic parameters for low modulus hydrogel PRINT particles with increasing diameters. Parameters were determined from particle concentration in whole blood at times 0.2 -104 hours post-dose using a standard two-compartment model according to the equation $C = Ae^{-\alpha t} + Be^{-\beta t}$ where C is the concentration of particles in blood, t is time post-dose.

of quantification, leaving too few data points for such analysis. These particles did not appear as if their clearance profile would fit well to a standard pharmacokinetic model due to the increase in particle concentration in blood at 3 and 7 hours, the explanation of which may require the application of more complicated models²³.

3.3 Conclusions and Future Work

The above studies have shown the promise of HPA based hydrogels for PRINT applications where extremely low modulus particles are desired. Hydrogels made from HP₃A were fabricated over a physiologically relevant range of moduli by varying the amount of PEG₄₀₀₀DA crosslinker. Low modulus ($E=6.5$ kPa) RBC-like microparticles fabricated with HP₃A demonstrated long elimination half-lives which we attribute, in part, to their deformability. Using this material, we were able to fabricate particles which were larger ($8.8\text{ }\mu\text{m}$) and smaller ($3.8\text{ }\mu\text{m}$) than RBCs, and saw evidence that particles of both sizes avoided physical sequestration as a result of their ability to deform.

Further reduction of particle size to less than a micron with similarly low modulus should follow the above studies. Reduction of particle size should allow for more facile avoidance of splenic and other filtration mechanisms, possibly leading to extended circulation times. The HP₃A monomer has a low vapor pressure compared to HEA and has very little evaporation when used in the PRINT process. Initial attempts to fabricate particles from 200 nm molds with 1% PEG₄₀₀₀DA crosslinked HP₃A appeared successful (**Figure 3.7**).

Much attention has been given to the potential of nanogels as pharmaceutical carriers due to their biocompatibility and potential for stimuli responsive cargo release². HPA

particles should show promise in this area, particularly for the encapsulation and release of macromolecular cargos, due to the high amount of swelling and the resultant large pore size of these gels. The inclusion of labile bonds into long-chain crosslinkers could facilitate cargo release from these gels. For example, acetal groups are stable at pH 7, but hydrolyze rapidly at acidic (pH =5) endosomal pH, resulting in cargo release in the endosome²⁴. Disulfide-functionalized crosslinkers degrade in response to the presence of glutathione inside of cells, and may be a promising strategy for cargo release²⁵. Derivatives of the silane-based, pH sensitive crosslinkers developed by Parrott, et al. in our laboratory may also be useful, especially due to the ease with which the degradation rate can be adjusted by changing the pendant groups on the silyl moiety²⁶.

The ability of lightly crosslinked, charged hydrogels to incorporate biomacromolecules of the opposite charge should be a focus of future study. In cases where the biomacromolecule and the hydrogel particle are oppositely charged, the components form a polyelectrolyte complex, with loading often proceeding throughout the gel rather than restricted to the surface². For example, cytochrome c, a cationic heme protein, was loaded efficiently into poly (acrylic acid)/PEG particles, with cargo release triggered by exposure to Ca^{2+} ions or acid²⁷.

For the fabrication of HPA hydrogels with high acid content, it may be desirable to synthesize a higher molecular weight, acid functional monomer. The monomer used in the current study, 2-carboxyethyl acrylate, suffers from some of the same volatility-based limitations as HEA. The extension of the PEG spacer in this monomer by one or two ethylene oxide units may allow for particles with higher acid content without any monomer evaporation.

3.4. Materials and Methods

3.4.1. Materials

Acryloyl chloride (97%), diethylene glycol (99%), triethylene glycol (99%), tetraethylene glycol (99%), and 2-carboxyethyl acrylate (CEA, 97%) were purchased from Sigma-Aldrich and used as received. Photoinitiators 2,2-diethoxyacetophenone (DEAP), and 1-hydroxyl-cyclohexyl phenyl ketone (HCPK) were purchased from Aldrich and used as received. Poly(ethylene glycol) diacrylate (PEG₄₀₀₀DA) and methacryloxyethyl thiocarbamoyl rhodamine B (PolyFluor 570) were purchased from Polysciences, inc. and used as received. Dylight 680 maleimide was purchased from Thermo Scientific. All other reagents were purchased from Fisher and were used without further purification unless otherwise noted.

3.4.2 Synthesis of Hydroxy PEG Acrylate Monomers

Mixtures of hydroxy PEG acrylate and hydroxy PEG diacrylate were obtained by reaction of di-, tri-, or tetraethylene glycol and acryloyl chloride in anhydrous dichloromethane under a nitrogen purge with triethylamine present as a scavenger for HCl evolved during the reaction. In order to obtain a higher ratio of monoacrylate to the diacrylated product and a good yield, a 7:3 ratio of di-, tri-, or tetraethylene glycol to acryloyl chloride was used²⁸. Addition of acryloyl chloride proceeded over 3 hours at room temperature, with stirring allowed to proceed for another 12-15 hours. The ammonium chloride salts were removed via filtration. The filtrate was washed several times with deionized water to extract the glycols and monoacrylates. The aqueous phase was washed

several times with diethylether to extract the monoacrylate. The ether washes were reduced by rotary evaporator in vacuo, and the product isolated via column chromatography. The product was eluted using a mixture of hexane, ethyl acetate and methanol in a 6:3:1 ratio. Free radical inhibitor 4-Methoxy Phenol (MEHQ) was added to the product fraction at 500 ppm of total acrylates prior to exhaustive vacuo rotoray evaporation to remove all of the residual solvent yielding a clear, colorless to pale yellow liquid. The acrylic monomers are referred to as hydroxyl PEG acrylates, with the length of the PEG chain attached to the acrylic moiety denoted by number. For example, HP₄A refers to the tetraethylene glycol adduct, while HP₂A refers to the diethylene glycol adduct.

3.4.3 Purification of HPA Monomers

Normal column chromatographic purification techniques were sufficient to produce reasonably pure HPA monomers (>95% purity by NMR). However, even trace impurities had measurable effects on the properties of the hydrogels fabricated with these monomers. As such, special care was taken to remove all possible impurities.

First, the separation of the mono- and diacrylate products by column chromatography required careful attention. It was necessary to take small volume fractions, especially between these two products, to ensure that no diacrylated byproduct remained to contaminate the HPA fractions. Moderately overloading a TLC plate allowed for more sensitive detection of this impurity than NMR spectroscopy.

Removal of solvent from the chromatographic fractions also proved somewhat problematic. Residual solvent in the HPA monomers caused hydrogels made from these samples to be softer, and less tough than those made from “neat” monomers. While this

effect was easily remedied by increasing the temperature and duration of the rotary evaporator, this tends to cause some of the monomer to polymerize. The presence of polymer in the solvent free HPA monomer can easily be determined by a qualitatively noticeable increase in monomer viscosity. Polymer formed in this way tends to act as a porogen in crosslinked hydrogels, changing the mechanical properties. Polymerization can be avoided with the addition of a free-radical inhibitor at low concentration (250-500 ppm) prior to rotary evaporation.

HPA monomers were stored in the freezer (-20 °C) and were warmed to room temperature prior to opening, as the monomers appear to be somewhat hygroscopic. It became apparent that, over time, diacrylate crosslinker was being generated in solution. This was most readily apparent in particles made from older or improperly stored HPA, where the hydrated diameters were smaller than expected. This was attributed to an ester hydrolysis-based mechanism, as pre-particle mixtures containing an acidic co-monomer (2-carboxyethyl acrylate) which was capable of catalyzing ester hydrolysis showed this effect more rapidly. Proper storage of the monomer for up to 3 months (at -20 °C in aliquots to prevent repeated exposure to the atmospheric moisture) resulted in reproducible particle diameters.

3.4.4 Modulus Testing

To measure the mechanical properties of crosslinked HPA hydrogels, macroscopic coupons of the prepolymer mixtures were polymerized via UV light in a Teflon mold. Approximately 650 μ L of freshly prepared prepolymer mixture was pipette into a 2.5 x 2.5 cm square mold. The mold was placed in a low-intensity UV oven, and nitrogen purged for 3 minutes prior to curing. The low intensity oven was used to minimize the heat generated

from the UV light. The coupons were cured for 5 minutes, allowed to cool for 3 minutes, then cured for an additional 3 minutes. The cross-linked hydrogels were removed from the mold, weighed, and placed in pH 7.4 PBS buffer for 24 hours to fully hydrate. The coupons were patted dry with paper towels and weighed again prior to sectioning into approximately 10 mm wide strips with a razor blade for testing with an Instron 5556 Universal Testing Machine (Instron) with a strain rate of 5 mm/min. Young's modulus was determined from the initial slope of the resultant stress-strain curves.

3.4.5 Particle Fabrication

Particles were fabricated using the PRINT (particle replication in non-wetting templates) process^{17,29}. PRINT molds for these studies were fabricated by Liquidia technologies and consisted of a thin layer of a patterned, photocured perfluoropolyether (PFPE) on top of a flexible poly(ethyleneterephthalate) (PET) backing.

To fabricate particles, the pre-polymer mixture was spread onto a mold which was taped to a silicon wafer and chilled to 2-5°C on a custom built laminator platform. The reduced temperature prevented evaporation of the pre-polymer solution prior to photo-curing. A PET sheet was laminated to the top of the mold and pre-polymer solution, wetting the total mold area. The sheet was peeled away at the nip point of the laminator, leaving the wells of the mold filled while wicking away excess solution. The filled mold was immediately transferred into a chilled (~5°C), nitrogen purged UV oven and cured with UV light ($\lambda=365\text{nm}$, 3 minutes, power ~ 20 mW/cm²).

Particles were transferred from the mold by laminating the filled, cured molds to a PET sheet which was coated with a thin film of Iuvitec (BASF). The particle-filled mold and

luvitec coating were placed in contact and passed through the nip point of a laminator. To increase the yield of harvested particles, a heated laminator was used for this step, with roll temperatures hot enough to allow the luvitec to flow and come into contact with the particles (typically ≥ 180 °F). Alternatively, it was possible in some cases to transfer the particles without added heat due to “sticky” adhesion of the particles to the luvitec film. After cooling briefly, the mold was peeled away from the luvitec sheet at a steep angle, leaving the particles on the luvitec film in an ordered array.

Harvesting of the particles from the ordered array on luvitec into solution was accomplished by “bead harvesting”. In this process, the particles on the harvesting film are passed through the vertical nip point formed by two rollers. At the nip point, a bead of water dissolves the luvitec layer, suspending the particles in solution, as the rollers slowly draw the film down through the nip. Streams of air are directed to either side of the bead of water to maintain it in the correct position to collect the particles. The particle solution can then be collected with a pipette with a fine tip.

3.4.6 Particle Harvesting and Purification

The bead harvesting process leads to well stabilized particles, but leaves an abundance of dissolved luvitec in solution. The particles were pelleted via centrifugation at 4 °C (12,000 rpm, 5-10 minutes depending on particle size) and the supernatant removed carefully so as not to disturb the pellet. The pellet was resuspended in a solution of 0.1% poly(vinyl alcohol) in Dulbecco’s pH 7.4 PBS buffer (Fisher Scientific) and this procedure was repeated 2-3 times to remove excess luvitec and any soluble fraction of poly(HPA) or unreacted monomers.

It is worth noting that tangential flow filtration (TFF), which has been suggested to be a promising and gentle method for purifying particles without causing aggregation¹⁷, proved a poor choice for these particles. In TFF filtration systems such as KrosFlo (Spectrum Laboratories, Inc.), particle solutions traveled tangentially to the membrane, effecting both diafiltration and concentration of particles while mediating particle loss due to adsorption to the membrane as a result of the indirect nature of the interaction. However, in this case, high pressures were required once the particle solution became concentrated, resulting in the mass fragmentation of the particles from the high shear stress. Centrifugation was gentler, with little or no particle fragmentation, and yielded stable particle dispersions, perhaps because of the high water content of the particles or the stabilizing presence of the luvitec and the poly(vinyl alcohol).

3.4.7 Particle Characterization

To accurately determine particle concentration, thermogravimetric analysis (TGA) was used. To determine the weight of salts and polymer in the solution, 50 μL of the particle solution was centrifuged exhaustively (14,000 RPM/20 minutes) to pellet the particles. The supernatant (20 μL) was pipetted to a tared TGA pan and the weight was monitored on a Perkin Elmer Pyris 1 TGA under the following heating steps: 25-115 $^{\circ}\text{C}$ by 10 $^{\circ}\text{C}/\text{minute}$ followed by a 10 minute hold to drive off the water in the solution. The dried sample provided the weight of salts and dissolved polymer in solution. In parallel, a 20 μL sample of the particle solution was analyzed under identical conditions, with the particle weight determined by subtracting the weight of salts and polymer in solution from this final weight.

Particles dimensions were determined by analysis of images from a microscope mounted camera (Zeiss AxioCam MRm) using a 100x objective (Zeiss Axio Imager D.1M). Over 50 fully hydrated particles in pH 7.4 PBS buffer were measured for each case. Zeta potentials for particles were measured on a nano ZS zetasizer (Malvern Instruments) in water.

3.4.8 In vivo Studies

To track the pharmacokinetics and biodistribution of particles in mice, 20 mg particles/kg mouse weight was administered via a 2.0 mg/mL solution of particles in PBS with 0.1% poly(vinyl alcohol) via tail-vein injection to female BALB/c mice of 20-22g body weight. Four mice were examined at each time-point, including points 0.2, 0.5, 1, 3, 7, 24, 56, and 104 hours post injection. At each time point examined, mice were sacrificed and tissues harvested. Harvested tissues included the lungs, liver, kidneys, spleens, heart and a posterior leg (thigh) muscle. Blood was collected via terminal cardiac puncture. Control mice were undosed.

3.4.9 Biodistribution

The fluorescent signal from the particles in the tissues and blood was measured using an IVIS Lumina fluorescent imager (Caliper Life Sciences) with excitation at 675 nm and emission measured at 720 nm. Blood was pipetted in 100 μ L aliquots to black 96 well plates for analysis on the IVIS Lumina imager, with blood measured in triplicate for each mouse. Harvested tissues were not perfused. Tissues were weighed after imaging, and biodistribution was expressed as a function of fluorescent signal per gram of tissue weight.

3.4.10 Pharmacokinetics of Particle Clearance from Blood

For determination of pharmacokinetic parameters including alpha and beta half-lives, a two-compartment model was fit to the data using nonlinear regression analysis. The two compartment model, which was described in Chapter 2, assumes that particles are transported between the central and peripheral compartments with first-order kinetics and that particles are eliminated from the central compartment with first-order kinetics. Equation 3.1, was applied to the data where C is the concentration of the particle in the blood, and α and β are rate constants for the distribution and elimination processes, respectively. Further details of the pharmacokinetic analysis can be found in Chapter 2, section 2.3.16.

$$C = Ae^{-\alpha t} + Be^{-\beta t} \quad \text{Equation 3.1}$$

3.5 Figures

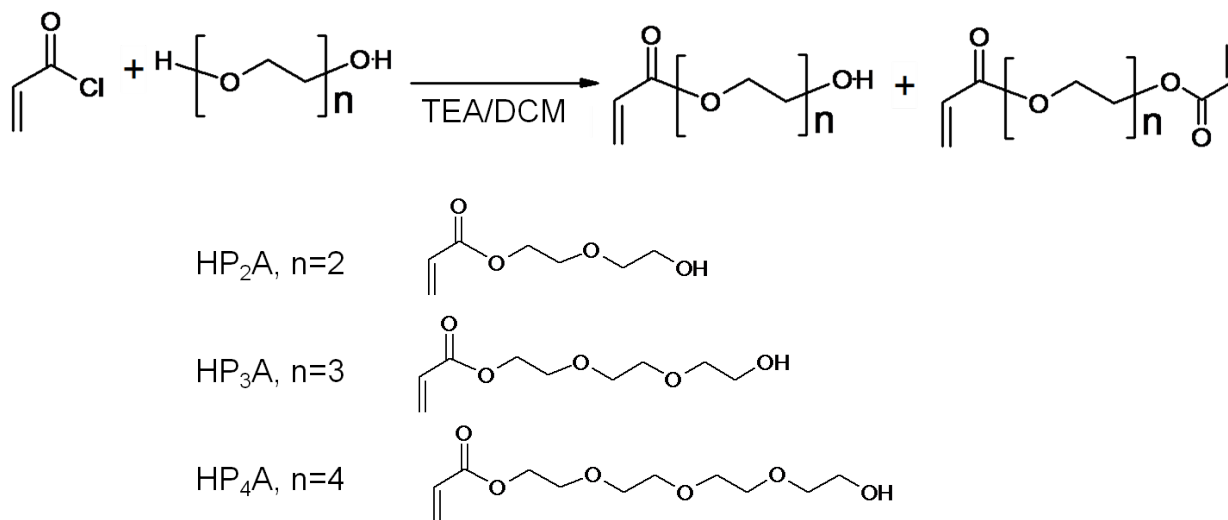


Figure 3.1. Synthetic scheme for hydroxyl PEG acrylates (HPAs). The structure of the monoacrylated products are shown below the reaction scheme, along with the naming convention.

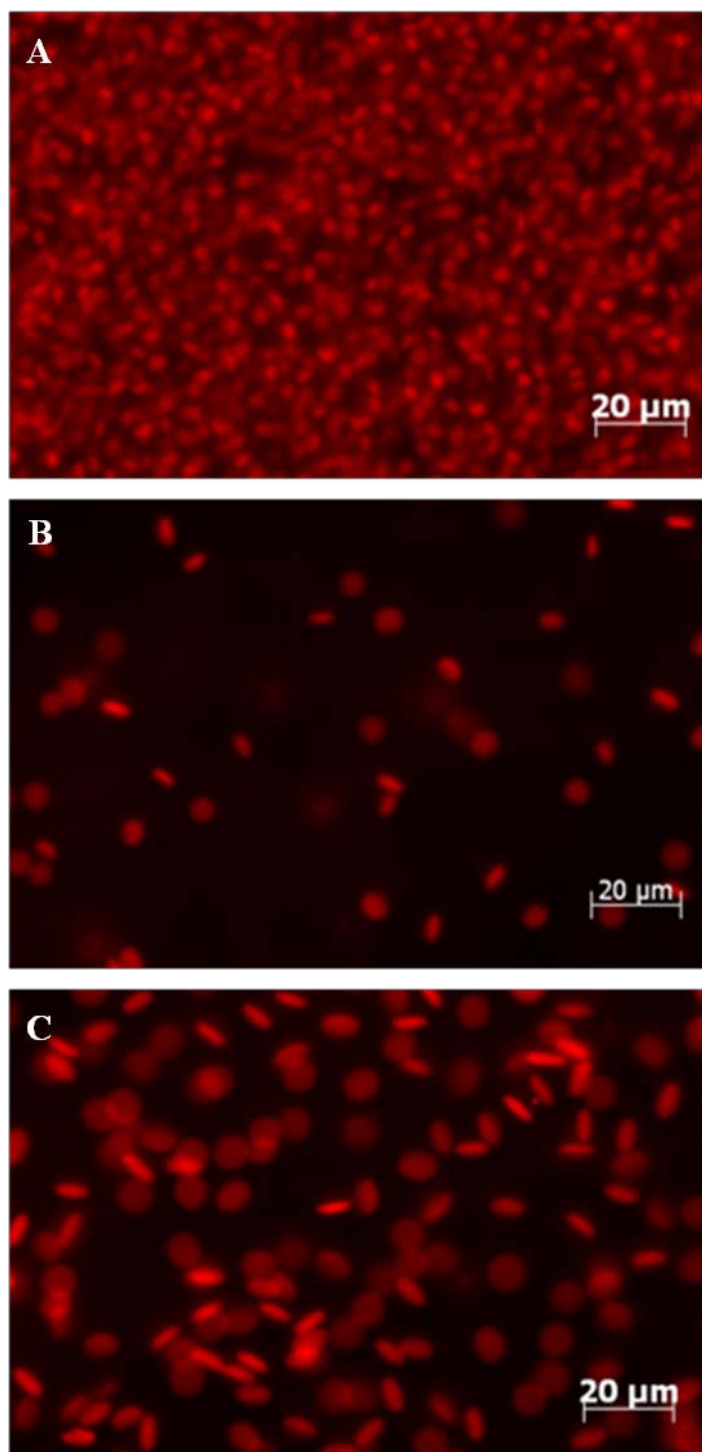


Figure 3.2. Fluorescent images of the particles used for the in vivo studies. The particles have hydrated diameters of (A) $3.79 \pm 0.17 \mu\text{m}$, (B) $6.39 \pm 0.56 \mu\text{m}$, and (C) $8.88 \pm 0.47 \mu\text{m}$.

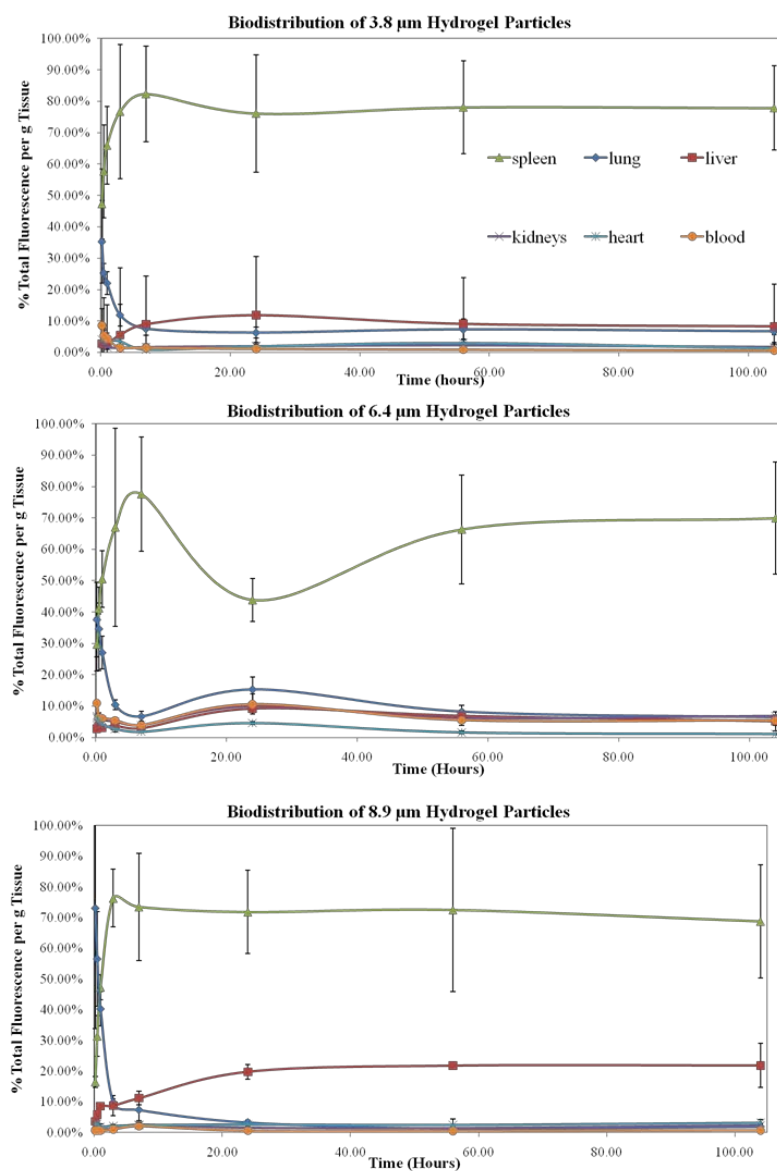


Figure 3.3. Biodistribution of extremely deformable particles of different sizes in mice over the course of several days. These semi-log plots show the percent of fluorescent signal normalized per gram of tissue weight. Four mice were examined per time-point, with error bars representing one standard deviation.

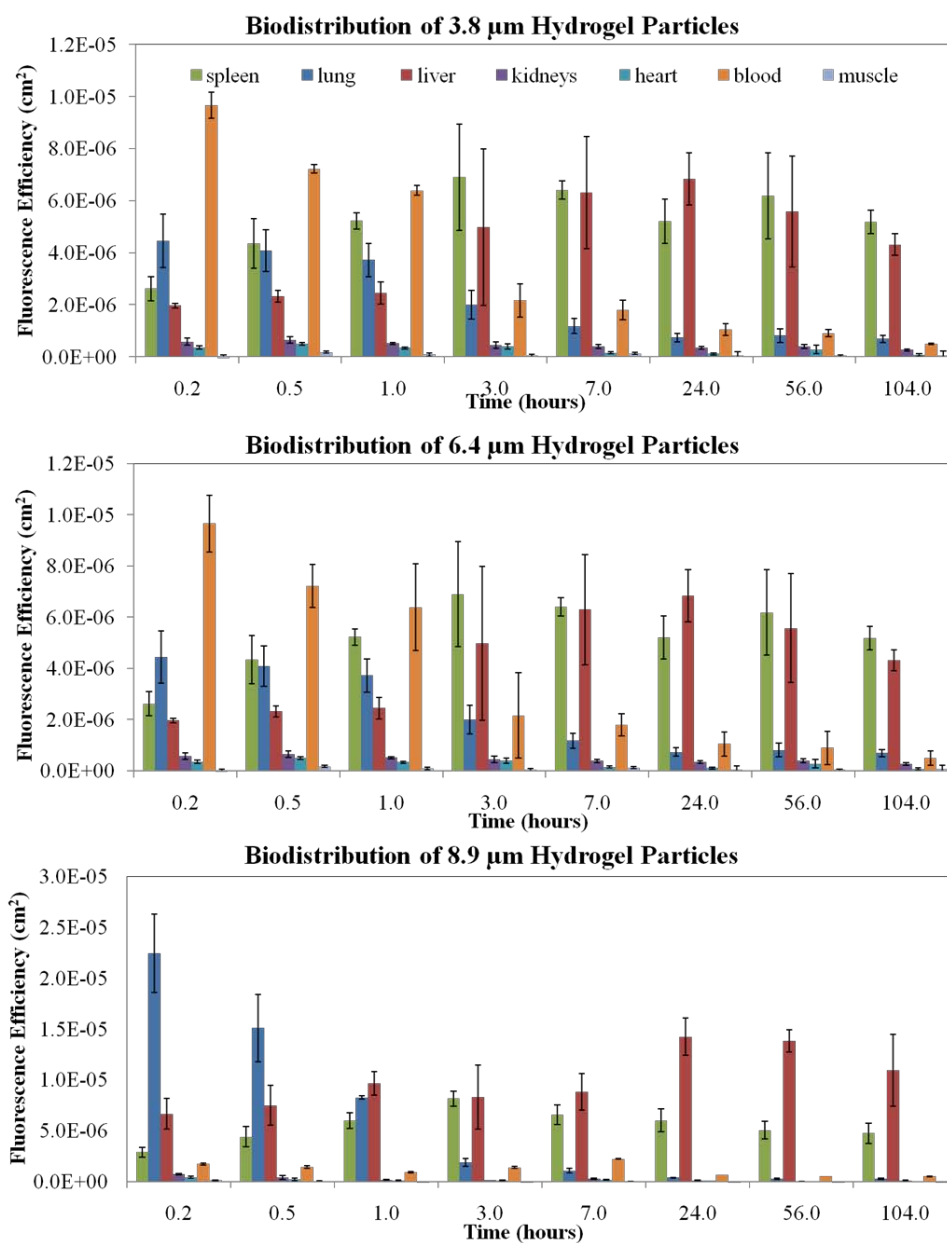


Figure 3.4. Biodistribution of low modulus hydrogel particles of different sizes in mice in terms of total fluorescence signal (fluorescence efficiency) in each tissue. Fluorescence in blood was measured in 100 μL aliquots and adjusted to account for the total blood volume of each mouse. Four mice were measured per time point. Error bars represent one standard deviation.

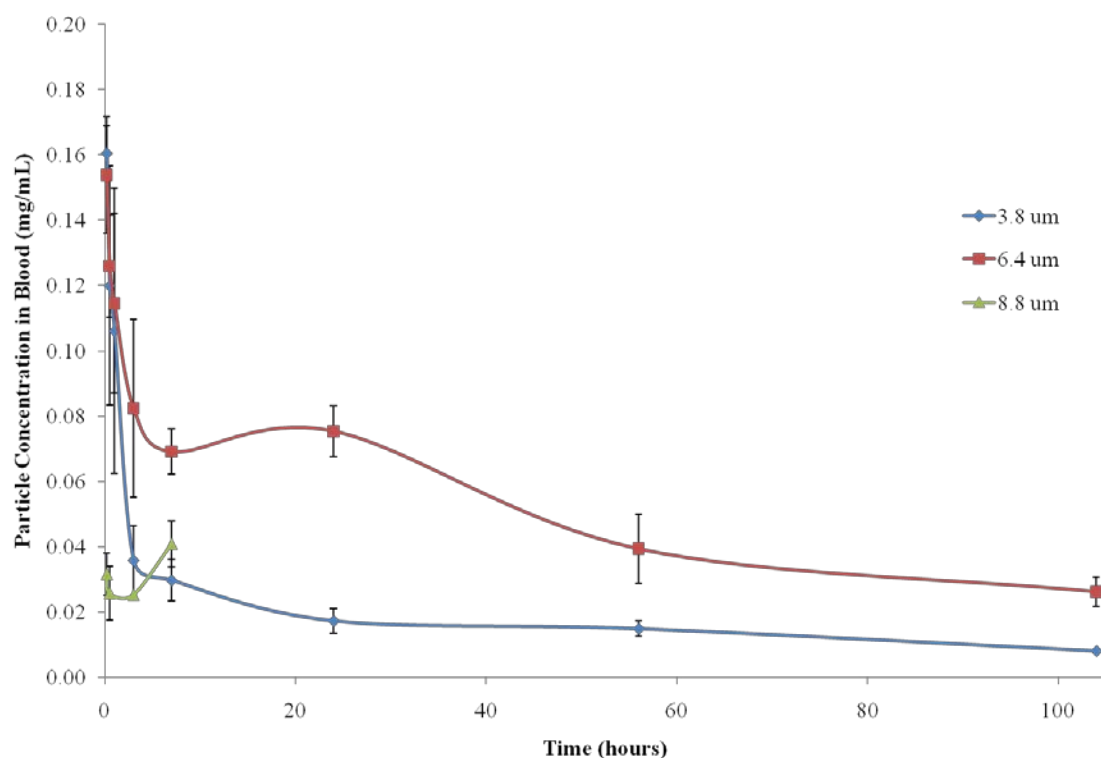


Figure 3.5. A plot showing the change in particle concentration in blood over time for particles of different sizes. Particles with a diameter of 6.4 μm , similar to that of mouse red blood cells, were cleared more slowly than both larger and smaller particles with identical mechanical properties and composition. The concentration of the largest particles, with a diameter of 8.8 μm , fell to below the lower limits of quantification after 7 hours post-injection.

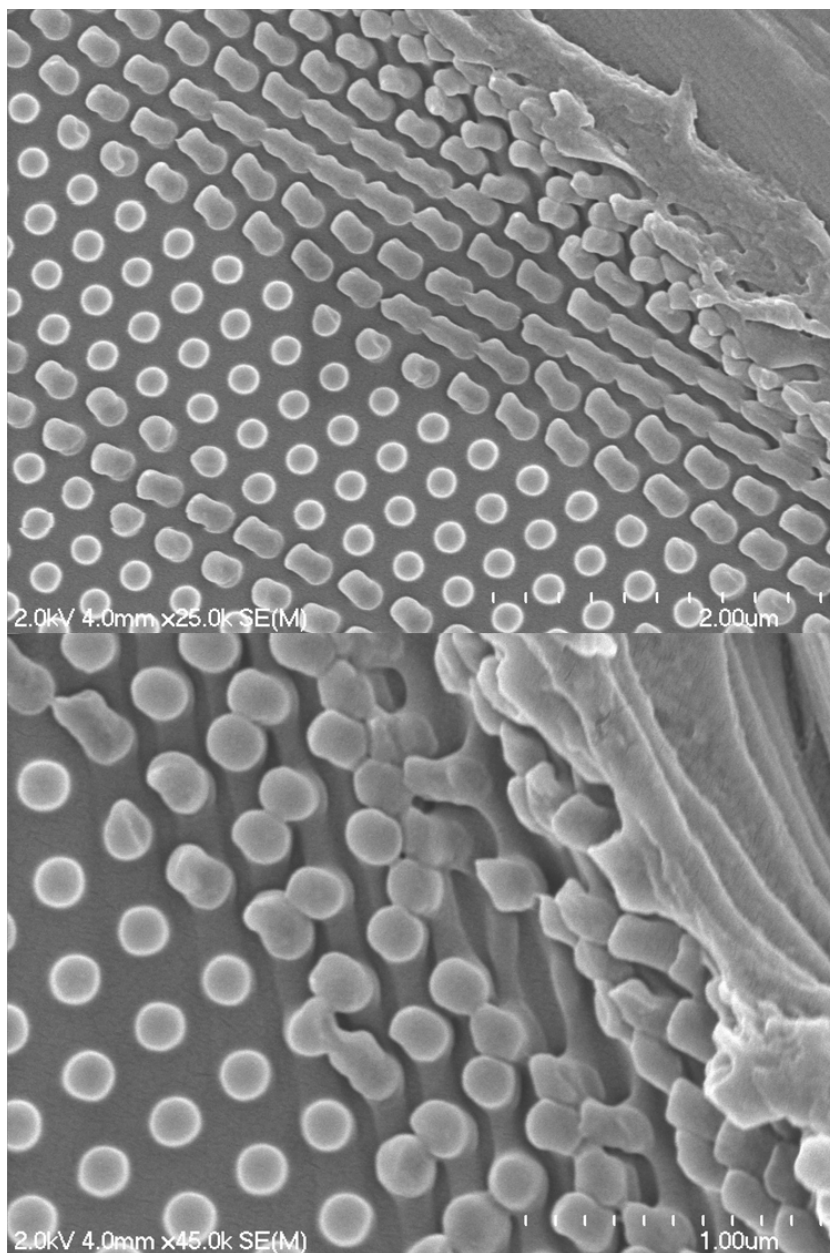


Figure 3.6. SEM images of 200 nm particles made from 1% PEG₄₀₀₀DA crosslinked HP₃A. The particles are on a harvesting film after transfer from the mold. A scratch in the harvesting film (top right corner of both images) illuminates the deformability of these particles where they were disturbed as the scratch was made.

3.6 References

- (1) Langer, R.; Peppas, N. A. *AIChE Journal* **2003**, *49*, 2990.
- (2) Kabanov, A. V.; Vinogradov, S. V. *Angew Chem Int Ed Engl* **2009**, *48*, 5418.
- (3) Mitragotri, S.; Lahann, J. *Nat Mater* **2009**, *8*, 15.
- (4) Graham, N. B. *Med Device Technol* **1998**, *9*, 22.
- (5) Graham, N. B. *Med Device Technol* **1998**, *9*, 18.
- (6) Nguyen, K. T.; West, J. L. *Biomaterials* **2002**, *23*, 4307.
- (7) Compan, V.; Tiemblo, P.; Garcia, F.; Garcia, J. M.; Guzman, J.; Riande, E. *Biomaterials* **2005**, *26*, 3783.
- (8) Hamidi, M.; Azadi, A.; Rafiei, P. *Adv Drug Deliv Rev* **2008**, *60*, 1638.
- (9) Justin, G.; Finley, S.; Abdur Rahman, A.; Guiseppi-Elie, A. *Biomedical Microdevices* **2009**, *11*, 103.
- (10) Yu, B.; Wang, C.; Ju, Y. M.; West, L.; Harmon, J.; Moussy, Y.; Moussy, F. *Biosensors and Bioelectronics* **2008**, *23*, 1278.
- (11) Leach, J. B.; Schmidt, C. E. *Biomaterials* **2005**, *26*, 125.
- (12) Beningo, K. A.; Wang, Y. L. *J Cell Sci* **2002**, *115*, 849.
- (13) Banquy, X.; Suarez, F.; Argaw, A.; Rabanel, J.; Grutter, P.; Bouchard, J.; Hildgen, P.; Giasson, S. *Soft Matter* **2009**, *5*, 3984.
- (14) Hendrickson, G. R.; Lyon, L. A. *Angew Chem Int Ed Engl* **2010**, *49*, 2193.
- (15) Haghgooie, R.; Toner, M.; Doyle, P. S. *Macromol. Rapid Commun.* **2009**, *31*, 128.

- (16) Merkel, T. J.; Jones, S. W.; Herlihy, K. P.; Kersey, F. R.; Shields, A. R.; Napier, M.; Luft, J. C.; Wu, H.; Zamboni, W. C.; Wang, A. Z.; Bear, J. E.; DeSimone, J. M. *Proceedings of the National Academy of Sciences* **2011**, *108*, 586.
- (17) Merkel, T. J.; Herlihy, K. P.; Nunes, J.; Orgel, R. M.; Rolland, J. P.; DeSimone, J. M. *Langmuir* **2009**, *26*, 13086.
- (18) Doshi, N.; Zahr, A. S.; Bhaskar, S.; Lahann, J.; Mitragotri, S. *Proc Natl Acad Sci U S A* **2009**, *106*, 21495.
- (19) Dulinska, I.; Targosz, M.; Strojny, W.; Lekka, M.; Czuba, P.; Balwierz, W.; Szymonski, M. *J Biochem Biophys Methods* **2006**, *66*, 1.
- (20) Gratton, S. E.; Ropp, P. A.; Pohlhaus, P. D.; Luft, J. C.; Madden, V. J.; Napier, M. E.; DeSimone, J. M. *Proc Natl Acad Sci U S A* **2008**, *105*, 11613.
- (21) Neubauer, A. M.; Sim, H.; Winter, P. M.; Caruthers, S. D.; Williams, T. A.; Robertson, J. D.; Sept, D.; Lanza, G. M.; Wickline, S. A. *Magn Reson Med* **2008**, *60*, 1353.
- (22) Brown, A. M. *Comput Methods Programs Biomed* **2001**, *65*, 191.
- (23) Li, M.; Al-Jamal, K. T.; Kostarelos, K.; Reineke, J. *ACS Nano* **2010**, *4*, 6303.
- (24) Goh, S. L.; Murthy, N.; Xu, M.; Frechet, J. M. *Bioconjug Chem* **2004**, *15*, 467.
- (25) Oh, J. K.; Siegwart, D. J.; Lee, H. I.; Sherwood, G.; Peteanu, L.; Hollinger, J. O.; Kataoka, K.; Matyjaszewski, K. *J Am Chem Soc* **2007**, *129*, 5939.
- (26) Parrott, M. C.; Luft, J. C.; Byrne, J. D.; Fain, J. H.; Napier, M. E.; Desimone, J. M. *J Am Chem Soc* **2010**, *132*, 17928.
- (27) Oh, K. T.; Bronich, T. K.; Kabanov, V. A.; Kabanov, A. V. *Biomacromolecules* **2007**, *8*, 490.
- (28) Guzman, J.; Iglesias, M. T.; Riande, E.; Compan, V.; Andrio, A. *Polymer* **1997**, *38*, 5227.

- (29) Rolland, J. P.; Maynor, B. W.; Euliss, L. E.; Exner, A. E.; Denison, G. M.; DeSimone, J. M. *J Am Chem Soc* **2005**, *127*, 10096.

Chapter 4

Cationic Microgel Particles for Identification of Cancer Biomarkers

4.1 Introduction to miRNA as Cancer Biomarkers

Taken together, all forms of cancer were projected to account for more than 1,500 deaths per day in the US in 2010¹. Although much progress has been made towards understanding cancer biology in the past decade, our progress towards early detection and screening for cancers has been considerably less successful². Early detection of cancer, an essential step towards improving treatment regimes, requires the discovery and development of sensitive and specific indicators, or biomarkers, of the disease. The recent discovery of cancer cell dysregulation of microRNAs (miRNAs) has pushed them forward as potential biomarker predictors of cancers, as well as therapeutic targets. These small (20-25 nucleotides), endogenous, non-coding RNAs discovered in 1993 negatively regulate gene expression and govern cellular processes. Aberrant expression of miRNA has been implicated in the pathogenesis of most human cancers². Several characteristics of miRNA point towards their use as tumor markers, including their stability, tissue specificity, and ease of detection. As such, miRNAs are obvious and promising candidates as diagnostic and predictive indicators for cancer.

Identification of miRNA may be complicated by the presence of ribonucleases in the blood which act to decrease the concentration of available miRNA biomarkers in the circulation, thereby reducing the sensitivity and prognostic efficacy of such an assay³. Complexation with, or encapsulation of, these oligomeric nucleic acids before they are degraded in the circulation by polymers should protect them from nuclease-based degradation, allowing for more sensitive detection^{4,5}. The formation of polyelectrolyte complexes with oligonucleotides has been shown to protect from nuclease-based degradation⁶. The capture and protection of miRNAs associated with cancers, followed by

recovery of these miRNAs for analysis, would be a compelling approach to the earlier, and less invasive, detection of miRNA associated cancers. A highly porous and deformable polycationic microgel should bind to and protect the negatively charged, and transiently available, miRNAs in the circulation. Upon recovery of these microgels from the blood they could be isolated from nuclease-containing blood components via cell lysis. Subsequent desorption of the bound miRNA should allow for identification of biomarkers at high sensitivity.

Here we present a strategy for the identification of transiently available miRNA biomarkers from the circulation for the purpose of identifying biomarkers of cancer. Cationic red blood cell-mimicking hydrogel PRINT particles (CRBCMs) with low modulus should have extended circulation times as a result of high deformability⁷. Surface modification of these CRBCMs via PEGylation with large (20 kDa) PEG yielded a core-shell structure with a slightly negative overall zeta potential and a highly porous, cationic core. These porous core particles demonstrated a generous capacity for binding to miRNAs and may be able to protect them from nuclease-based degradation. Such a strategy may be able to capture and protect transiently available miRNA biomarkers for cancers, potentially providing for the discovery of novel biomarkers and for increased sensitivity for the detection of known miRNA biomarkers, thus potentiating early detection of the disease.

4.2 Results and Discussion

4.2.1 Low Modulus Cationic Hydrogels

To test this theory, low modulus hydrogels were fabricated with the inclusion of 2-aminoethyl methacrylate (AEM) to provide the gels with a positive charge (**Table 4.1**). Bulk

samples of hydrogels composed primarily of 2-hydroxyethyl acrylate (HEA), with 5-20% AEM, 1% of DEAP photoinitiator, 0 or 10% of a nonreactive PEG porogen (PEG₅₅₀dimethyl ether) and 2-10% of PEG₄₀₀₀DA crosslinker were polymerized in a Teflon mold via UV light in a nitrogen-purged UV oven. The coupons were hydrated overnight in pH 7.4 PBS to mimic physiological conditions, and samples tested in an Instron tensometer with a strain rate of 5 mm/min to determine the Young's modulus of the hydrogels. Hydrogels containing 2-4% of PEG₄₀₀₀DA crosslinker and 20% of the cationic monomer (AEM) possessed the levels of elasticity similar to that of red blood cells (15-26 kPa)^{8,9}. This level of deformability has been shown to promote long circulation times through avoidance of physical filtration in the capillary beds and elsewhere in the body⁷. These studies suggest that it should be possible to tune the pore size through the addition of porogens or by alterations in the amount of crosslinker present in these gels. Further, by varying the amount of positively charged monomer (AEM) the binding strength and release profiles for bound RNA cargos can be adjusted.

PEG ₄₀₀₀ Diacrylate	10	5	5	5	4	2
2-aminoethyl methacrylate	10	5	20	20	20	20
2-hydroxyethyl acrylate	79	89	74	64	65	77
PEG ₅₅₀ DME	-	-	-	10	-	-
Young's modulus	55.3 ± 8.5	25.2 ± 6.4	33.6 ± 5.4	12.66 ± 4.5	15.6 ± 3.2	5.7 ± 2.7

Table 4.1. Young's modulus values for cationic hydrogels with varied crosslink density, charge density, and amount of porogen added.

4.2.2 Fabrication of Cationic Red Blood Cell Mimicking PRINT Particles

RBC shaped particles were fabricated with the 4% crosslinker hydrogel described in Table 5.1 using 2 µm diameter, discoid PRINT molds for hydrated particles with

approximately 6 μm diameters. The fabrication method was similar to that used in Chapter 2 for other HEA-based hydrogels, with chilled equipment mediating any monomer evaporation. The cationic red blood cell mimics (CRBCMs) were harvested from the mold by freezing into a layer of 0.1% 22 kDa poly(vinyl alcohol) (PVOH) in water. A high molecular weight stabilizer (PVOH) was used here to decrease penetration and binding of the PVOH to the particle interior. The hydrated particles had a diameter of 6.2 μm and a zeta potential of 13.1 ± 3.41 mV in 10 μM KCl. To give the particles a neutral or slightly negative charge while maintaining a cationic interior for binding to RNA, the CRBCMs were functionalized with PEG-NHS reagents of several lengths (**Table 4.2**). Neutral or negative zeta potentials have been shown to decrease the rate of particle uptake, extending the circulation times of particles *in vivo*¹⁰. Longer PEG chains may be better suited to shield the cationic charge of the hydrogel particles while allowing miRNA to diffuse to the particle interior. A 20 kDa PEG gave the most negative zeta potential, and was used for surface functionalization of CRBCMs in the following studies.

Surface Functionalization Reagent	Zeta Potential (mV)
None	13.10 ± 3.41
5,000 g/mol PEG-NHS	2.99 ± 4.55
20,000 g/mol PEG-NHS	-3.37 ± 3.51
30,000 g/mol PEG-NHS	-1.83 ± 4.03
35,000 g/mol PEG-NHS	0.74 ± 3.92

Table 4.2. Zeta potential of cationic red blood cell mimicking microgels with varying PEG chain length used for surface modification.

4.2.3 Binding Capacity

A DNA 20mer modified with a Cy3 dye (provided by the Sullenger lab, Duke University) was used as a model for miRNA in initial tests to determine the binding capacity

of CRBCMs. PEGylated CRBCMs were incubated at 37° C for 4 hours on 1 μ M Cy3 labeled DNA. After washing (3x in DI water), fluorescence microscopy revealed a significant amount of fluorescence present in the Cy3 channel associated with the particles implying binding of the dye labeled DNA (**Figure 4.1**). To determine the capacity of the CRBCMs to bind nucleic acids, ICP-MS was used to determine the amount of DNA by measuring the phosphorous present (from the DNA backbone) in a sample of particles. CRBCMs that were surface functionalized with 20 kDa PEG to a neutral zeta potential and which were composed of 20% AEM were found to have bound 0.28 mg of DNA/mg particles.

4.2.4 Binding and Release of miRNA from Cationic Microgels

As a first step in determining the capacity of the CRBCMs to bind to and protect miRNAs from ribonuclease (RNase) based degradation, we sought to bind miRNAs to the particles and affect their release via incubation with competing polyanions at high salt concentration. MicroRNAs associated with prostate cancer were purchased from Sigma; miRNA 96 was associated with cancer recurrence after radical prostatectomy in a study of 79 human patients¹¹ and miRNA 100 is overexpressed in several prostate cancer cell lines and is believed to play a role in metastasis of this cancer¹². CRBCMs that had been surface functionalized with 20 kDa PEG were incubated with either miRNA 96 or miRNA 100 to load them with the RNA. To release the bound miRNA, the CRBCMs were washed several times to remove unbound miRNA, then incubated at 37 °C for 1 hour with 5mg /mL sodium heparin (Sigma) in 0.5 M Tris buffer. The particles were spun down and the supernatant loaded onto a gel. To provide a negative signal, with degraded RNA, a sample of each RNA was incubated with RiboShredder RNase cocktail. The RNA was washed and resuspended in

loading buffer to run on the gel. The gel (**Figure 4.2**) shows no signal from degraded miRNA, and a broad band associated with the miRNA released from the CRBCMs. Band broadening is likely due to the high salt content remaining in solution from the desorption conditions. Future work will include an EtOH precipitation step to remove these salts before analysis. We were unable to visualize any of the degraded RNA with ethidium bromide, likely due to the efficacy of degradation resulting in the inability of the dye to bind to the RNA fragments for increased fluorescence.

4.3 Conclusions and Future Work

The above experiments represent a promising beginning to this work, though many questions remain unanswered at this time. Cationic hydrogels have been designed with a low modulus suitable for translation to long circulating microparticles. Cationic red blood cell mimicking PRINT particles with a surface coating of PEG have demonstrated the capacity for binding and triggered release of miRNAs. However, cross-link densities in CRBCMs may need to be adjusted to enable miRNAs to diffuse into and bind to the interior of the particles but still exclude the larger ribonucleases. Challenge experiments should be carried out by exposure of the miRNA-loaded CRBCMs to ribonucleases (RiboShredder) to optimize the crosslink density so that the miRNAs are bound with high efficiency but are not degraded. While ribonucleases may be small enzymes, they are larger than the short (20-25 nucleotides) miRNAs. RNase A, for example, consists of 124 amino acids with a weight of approximately 13.7 kDa; significantly larger than the short miRNAs. This point will be essential to the viability of CRBCMs for *in vivo* applications.

Identification and quantification of bound miRNAs will be essential for the discovery of novel biomarkers as well as in screening for known cancer-associated miRNAs. The identity of isolated miRNAs can be confirmed via a sequencing reaction^{13,14}. Commercial assays for quantitative reverse transcriptase polymerase chain reaction (qRT-PCR) should allow for the analysis of multiple miRNAs in small sample sizes¹⁵. It should be possible to sequester and identify miRNAs from increasingly complex biological samples; from mixtures of two or more miRNAs (miRNA-100 and miRNA-96) to incubation of CRBCMs with PC-3 (prostate cancer) cells, which are known to overexpress miRNA-100, among many others. The ultimate goal will be to inject CRBCMs into xenograft and GEM mouse models of cancers and to identify and quantify the bound nucleic acids to determine their utility as biomarkers for the associated cancers. Computational and experimental approaches indicate that many more miRNAs are likely to be identified¹⁶⁻¹⁸. By sequestering transiently available miRNA components of the secreted proteome of a cancer model, we may be able to identify biomarkers of disease with greater sensitivity or specificity than is currently possible.

The development of low modulus hydrogels with tunable properties opens the door on a number of possible therapeutic possibilities for deformable particles made from these gels. The cationic gels described above may have multiple applications with very little modification to the particle matrix. For example, such deformable particles may be capable of encapsulating a cationic drug for delivery to the spleen. Similarly, these particles may be capable of sequestering and clearing extracellular DNA to mediate inflammation¹⁹. Inclusion of a complementary RNA or DNA sequence to a crosslinking chain in similarly deformable particles could lead to highly specific screening methods for a single nucleic acid biomarker.

4.4 Materials and Methods

4.4.1 Materials

Photoinitiators 2,2-diethoxyacetophenone (DEAP), and 2-aminoethylmethacrylate hydrochloride salt (AEM) were purchased from Sigma and used as received. Poly(ethylene glycol) Diacrylate (4,000 g/mol) was purchased from Polysciences, Inc. Commercially available 2-hydroxyethylacrylate (HEA, 96%, Aldrich) contains impurities such as acrylic acid, ethylene glycol and ethyleneglycol diacrylate (EGDA), and was purified prior to use according to the procedure set forth by Elif, et al ²⁰, as described in Chapter 2 of this dissertation. The miRNAs (mir-100 AACCCGUAGAUCCGAACUUGUG, and mir- 96 UUUGGCACUAGCACAUUUUUGCU) were purchased from Sigma, with sequences identified with the miRBase database²¹. RiboShredder RNase cocktail (Epicentre Biotechnologies) was used according to the manufacturer's directions. All other reagents were purchased from Fisher Scientific and were used as received unless otherwise noted.

The PRINT molds used in the above studies were provided by Liquidia Technologies, and were fabricated using the master templates described in Chapter 2.

4.4.2 Modulus Testing

To measure the mechanical properties of crosslinked cationic hydrogels, macroscopic coupons of the prepolymer mixtures were polymerized via UV light in a Teflon mold. Approximately 650 μ L of freshly prepared prepolymer mixture was pipette into a 2.5 x 2.5 x 0.5 cm square mold. The mold was placed in a low-intensity UV oven, and nitrogen purged for 3 minutes prior to curing. The low intensity oven was used to minimize the heat generated from the UV light. The coupons were cured for 5 minutes, allowed to cool for 3

minutes, then cured for an additional 3 minutes. The cross-linked hydrogels were removed from the mold, weighed, and placed in pH 7.4 PBS buffer for 24 hours to fully hydrate. The coupons were patted dry with paper towels and weighed again prior to sectioning into approximately 10 mm wide strips with a razor blade for testing with an Instron 5556 Universal Testing Machine (Instron) with a strain rate of 5 mm/min. Young's modulus was determined from the initial slope of the resultant stress-strain curves.

4.4.2 Particle Fabrication

The fabrication and harvesting of particles followed the procedures outlined in Chapter 2 for the fabrication of HEA-based PRINT particles. Briefly, in low humidity (<30% relative humidity at 70 °F) the pre-polymer mixture was spread onto a mold which was taped to a silicon wafer and chilled to 2-5°C on a custom built laminator platform. The reduced temperature prevented evaporation of the pre-polymer solution prior to photo-curing. A PET sheet was laminated to the top of the mold and pre-polymer solution, wetting the total mold area. The sheet was peeled away at the nip point of the laminator, leaving the wells of the mold filled while wicking away excess solution. The filled mold was immediately transferred into a chilled (~5°C), nitrogen purged UV oven and cured with UV light ($\lambda=365\text{nm}$, 3 minutes, power ~ 20 mW/cm²). The particles were transferred from the mold by the process of ice harvesting (described in chapter 2). Briefly, the filled molds were placed face-down onto a thin layer of water with 0.1% PVOH on a sheet of PET. For the cationic particles, a 22 kDa PVOH was used (Sigma). This assembly was frozen on dry ice for 30 minutes, then the mold was peeled away rapidly, leaving the particles embedded in the ice layer. Particles were then collected with the bead harvester described in Chapter 3.

4.4.3 Particle Purification

The particles were pelleted via centrifugation at 4 °C (12,000 rpm, 4) and the supernatant removed carefully so as not to disturb the pellet. The pellet was resuspended in a solution of 0.1% PVOH (22kDa) in Dulbecco's pH 7.4 PBS buffer (Fisher Scientific) and this procedure was repeated 2-3 times to remove any soluble fraction or unreacted monomers. Particles prepared for binding efficiency studies via ICP/MS were washed with millipore water rather than the stabilized buffer. The concentration of particles in solution was obtained via thermogravimetric analysis using a Perkin Elmer Pyris 1 TGA.

4.4.4 Surface Modification

To modify the surface of amine-containing particles with PEG, the particles were suspended in pH 7.4 PBS buffer. N-hydroxy succinimidyl ether modified PEG was added in excess (~1.5 molar equivalents compared to the total amines in the particles). The mixture was incubated at room temperature for 4 hours with mixing on a shaker. The particles were then washed with PBS by centrifugation and resuspension (3 times). The PEGylation reaction was monitored by the change in zeta potential of the particles from positive to neutral or slightly negative.

The capacity of the CRBCMs to bind nucleic acids was quantified using a Varian 820 ICP-MS to determine the amount of phosphorous in the sample. Briefly, CRBCMs that were surface functionalized with 20 kDa PEG were incubated at 37°C with 100 µM Cy3 labeled DNA 20mer for 1 hour. The particles were washed with Millipore water (3x) via

centrifugation and resuspension. This solution was submitted to UNC's mass spec facility for analysis.

4.4.6 Binding and Release of miRNA

CRBCMs that had been surface functionalized with 20 kDa PEG were incubated with either miRNA 96 or miRNA 100 (300 ng) at 37°C for 1 hour then spun down and washed with DEPC water (2 times) to remove unassociated miRNA. The CRBCMs were incubated at 37 °C for 1 hour with 5mg /mL sodium heparin (Sigma) in 0.5 M Tris buffer to effect release of the bound RNA. Particles were spun down and the supernatant loaded onto a 2.5% agarose gel. A sample of each RNA was incubated with RiboShredder RNase cocktail for 10 minutes, then phenol/chloroform extracted to remove the enzymes, and EtOH precipitated to collect the degraded RNA. The RNA pellet was washed in 70% EtOH, repelleted and dried before resuspending in loading buffer to run on the gel.

4.5 Figures

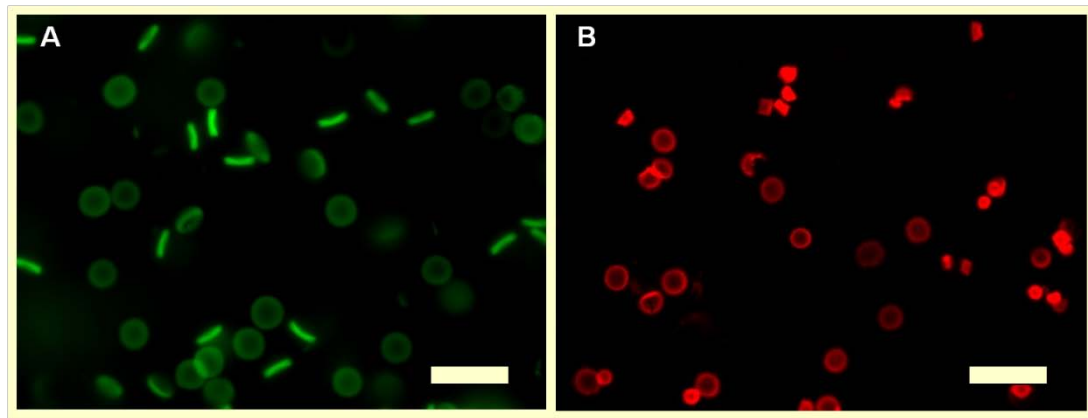


Figure 4.1. Cationic hydrogel particles (A) Particles fluoresce in the green channel due to matrix bound fluorescein dye. (B) Fluorescence in the red channel from adsorbed Cy3 dye-conjugated DNA 20mer. Particles were incubated at 37 °C for one hour with 1 μ M DNA, then washed 3 times to remove unassociated DNA. Scale bars are 20 μ m.

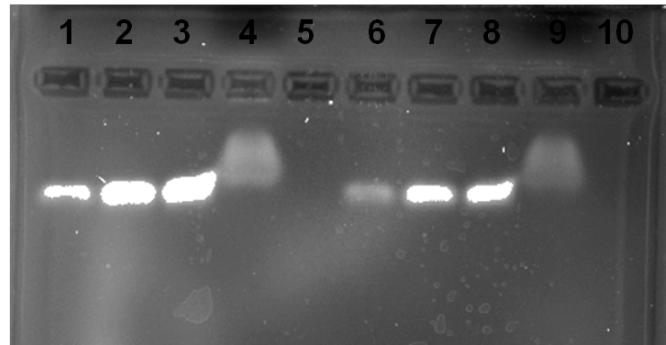


Figure 4.2. Analysis of miRNAs bound to and released from CRBCM particles. Lanes 1-3 are miRNA 96 in increasing amounts (100, 200 and 300 ng). Lane 4 is miRNA 96 desorbed from CRBCs in high salt concentration, causing band broadening. Lane 5 was loaded with miRNA 96 after degradation with and RNase cocktail. Ethidium bromide was not sufficient to stain the degraded RNA. Lanes 6-10 were identical to 1-5, respectively, but with miRNA 100 in place of miRNA 96.

4.6 References

- (1) Jemal, A.; Siegel, R.; Xu, J.; Ward, E. *CA Cancer J Clin* **2010**, *60*, 277.
- (2) Heneghan, H. M.; Miller, N.; Kerin, M. J. *Curr Opin Pharmacol* **2010**, *10*, 543.
- (3) Gary, D. J.; Puri, N.; Won, Y.-Y. *Journal of Controlled Release* **2007**, *121*, 64.
- (4) Fox, M. E.; Szoka, F. C.; Frechet, J. M. *Acc Chem Res* **2009**, *42*, 1141.
- (5) Hamidi, M.; Azadi, A.; Rafiei, P. *Adv Drug Deliv Rev* **2008**, *60*, 1638.
- (6) Zelphati, O.; Szoka, F. C., Jr. *Proc Natl Acad Sci U S A* **1996**, *93*, 11493.
- (7) Merkel, T. J.; Jones, S. W.; Herlihy, K. P.; Kersey, F. R.; Shields, A. R.; Napier, M.; Luft, J. C.; Wu, H.; Zamboni, W. C.; Wang, A. Z.; Bear, J. E.; DeSimone, J. M. *Proceedings of the National Academy of Sciences* **2011**, *108*, 586.
- (8) Doshi, N.; Zahr, A. S.; Bhaskar, S.; Lahann, J.; Mitragotri, S. *Proc Natl Acad Sci U S A* **2009**, *106*, 21495.
- (9) Shevkoplyas, S. S.; Yoshida, T.; Gifford, S. C.; Bitensky, M. W. *Lab Chip* **2006**, *6*, 914.
- (10) Gratton, S. E.; Ropp, P. A.; Pohlhaus, P. D.; Luft, J. C.; Madden, V. J.; Napier, M. E.; DeSimone, J. M. *Proc Natl Acad Sci U S A* **2008**, *105*, 11613.
- (11) Schaefer, A.; Jung, M.; Mollenkopf, H. J.; Wagner, I.; Stephan, C.; Jentzmik, F.; Miller, K.; Lein, M.; Kristiansen, G.; Jung, K. *Int J Cancer* **2010**, *126*, 1166.
- (12) Leite, K. R.; Sousa-Canavez, J. M.; Reis, S. T.; Tomiyama, A. H.; Camara-Lopes, L. H.; Sanudo, A.; Antunes, A. A.; Srougi, M. *Urol Oncol* **2009**.
- (13) Lagos-Quintana, M.; Rauhut, R.; Lendeckel, W.; Tuschl, T. *Science* **2001**, *294*, 853.
- (14) Lu, C.; Tej, S. S.; Luo, S.; Haudenschield, C. D.; Meyers, B. C.; Green, P. J. *Science* **2005**, *309*, 1567.

- (15) Tang, F.; Hajkova, P.; Barton, S. C.; O'Carroll, D.; Lee, C.; Lao, K.; Surani, M. A. *Nat Protoc* **2006**, *1*, 1154.
- (16) Bentwich, I.; Avniel, A.; Karov, Y.; Aharonov, R.; Gilad, S.; Barad, O.; Barzilai, A.; Einat, P.; Einav, U.; Meiri, E.; Sharon, E.; Spector, Y.; Bentwich, Z. *Nat Genet* **2005**, *37*, 766.
- (17) Berezikov, E.; Cuppen, E.; Plasterk, R. H. *Nat Genet* **2006**, *38 Suppl*, S2.
- (18) Sassen, S.; Miska, E. A.; Caldas, C. *Virchows Arch* **2008**, *452*, 1.
- (19) Lotze, M. T.; Deisseroth, A.; Rubartelli, A. *Clin Immunol* **2007**, *124*, 1.
- (20) Elif, V.; Ali, U. *J. Polym. Sci., Part A: Polym. Chem.* **2005**, *43*, 3957.
- (21) Griffiths-Jones, S.; Grocock, R. J.; van Dongen, S.; Bateman, A.; Enright, A. J. *Nucleic Acids Res* **2006**, *34*, D140.

Chapter 5

Summary and Future Directions

5.1 Summary

Establishing the dependency of particle behavior *in vivo* on the characteristic of deformability has relevance for many different medical research foci, including rational particle design for drug delivery, medical imaging, and synthetic blood, as well as furthering our understanding of cancer metastasis. Much attention has been directed towards the generation of particle design “maps” with the primary focus on the effect of changes in particle size and shape on their biodistribution *in vivo*, while particle modulus has largely been ignored. The particle replication in non-wetting templates (PRINT) technique allows for the fabrication of “calibration quality” particles through the tight control of particle size and shape afforded by the precision of the semiconductor industry-derived techniques used to fabricate PRINT master templates and molds. By allowing us to specifically change particle modulus, while size and shape remain constant, or to change particle shape with deformability unchanged, we have been able to probe the specific biological effect of these independent parameters. Having demonstrated the relevance of particle deformability, we have essentially added a novel parameter to the biodistribution maps sought by researchers in the above fields. In addition to particle shape, size, charge, and surface chemistry we now see that the stiffness of the particle can drastically change *in vivo* behavior.

Multiple applications for long-circulating particles which avoid liver uptake have been enabled by the unique circulation and biodistribution profile of deformable red blood cell mimicking microgel particles. In initial studies, cationic versions of these particles showed the ability to sequester negatively charged RNAs through electrostatic complexation. These particles may be useful for the detection and discovery of miRNA biomarkers of disease.

5.1.1 Mechano-biological Mimicry of Red Blood Cells

The addition of a non-functional monomer to hydrogel pre-particle formulations, such as an ether terminal short PEG chain, can increase hydrogel porosity while decreasing the stiffness. Our initial efforts towards this strategy taught us several valuable lessons with regards to translating increased particle flexibility to altered *in vivo* behavior. Simply increasing particle deformability did not guarantee measurable changes in biodistribution or clearance profiles. It was determined that more sophisticated methods for *in vitro* evaluation of particle deformability would be necessary to ensure biologically relevant levels of particle flexibility were achieved. We found that simple modifications to the commonly used PRINT particle formulations, consisting primarily of PEG triacrylates, yielded particles with poor properties for *in vivo* applications. The biodistribution of particles suggested that particle fragmentation occurred in the case of the most deformable particles made with these formulations – a clearly undesirable result. Analysis of bulk samples revealed that the elastic moduli of the materials used were on the order of 1 MPa and were somewhat brittle when hydrated. In fact, these measurements were difficult to obtain due to the brittle nature of these bulk samples; the samples broke with very slight bending, and tended to crumble when placed in the clamps of the tensometer if more than minimal pressure was applied to hold the samples. Further decreases in crosslink density for these, or similar, PEG di- or triacrylates, would yield a lower modulus material; however, a corresponding decrease in the material toughness would likely result in the advent of greater fragmentation.

Lightly crosslinked hydrogels composed primarily of 2-hydroxyethyl acrylate (HEA) were found to have mechanical properties which were desirable for translation to deformable PRINT particles. HEA hydrogels fabricated with 1-10% PEG₄₀₀₀DA were found to have

bulk elastic moduli on the order of tens of kPa, which was in the range of the modulus of red blood cells (RBCs) found in the literature (26 kPa)¹. Further, hydrated HEA hydrogels were quite elastic, with yield strain on the order of 100% for this range. A microfluidic system with constricted channels was designed to be a rigorous test of particle deformability for particles with size and shape reminiscent of RBCs. These devices served as a successful *in vitro* method for examining red blood cell mimic (RBCM) particle deformability, as more highly crosslinked RBCMs clogged in the entrance to the channels while the more deformable (lower % crosslinker) particles were better able to navigate them.

In the *in vivo* testing, the highly deformable 1% crosslinked RBCMs avoided filtration in the capillary beds in the lungs, leading to much slower clearance compared to particles which were stiffer. Elimination half-life of the 1% RBCMs lengthened by a factor of 30, to 3.8 days, as a result of an approximately 8 fold decrease in elastic modulus compared to the 10% crosslinked RBCMs. These results of the pharmacokinetic analysis from a fairly novel intravital microscopy method were confirmed via a more conventional blood-draw experiment. The intravital method used for tracking particle clearance from the peripheral vasculature was thereby determined to be valid for the estimation of particle pharmacokinetics. This intravital method should continue to be a crucial tool for future studies, as it significantly reduces the number of mice and amount of particles required for an initial examination of particle *in vivo* behavior.

5.1.2 Pharmacokinetics and Biodistribution of Low Modulus Hydrogel Particles

Efforts to continue to map out the role of particle deformability in particles of varied size proceeded with the synthesis of novel acrylic monomers which were well suited to the

PRINT process. We synthesized acrylates functionalized with hydroxyl terminal oligomeric PEG chains with 2, 3, and 4 repeat units. Hydrogels synthesized with these hydroxyPEG acrylates (HPAs) had properties similar to HEA based hydrogels, including low modulus. By increasing the molecular weight of the monomer via an increase in the side chain (PEG) length, the in-mold evaporation seen with the lower molecular weight HEA monomer was avoided. As surface PEGylation is in common use as a strategy to decrease particle opsonization, the increased PEG character of the hydrogel may make this monomer even more desirable for future particle studies *in vivo*. HPA based hydrogels are well suited for PRINT applications where extremely low modulus particles are desired.

Deformable HP₃A hydrogel particles were fabricated over a range of moduli by varying the amount of PEG₄₀₀₀DA crosslinker. Low modulus ($E=6.5$ kPa) RBC-like microparticles fabricated with HP₃A demonstrated long elimination half-lives similar to what was found with HEA based RBCMs of nearly identical modulus. Using this material, we were able to fabricate particles which were larger ($8.8\ \mu\text{m}$) and smaller ($3.8\ \mu\text{m}$) than RBCs, and saw evidence that particles of both sizes avoided physical sequestration as a result of their ability to deform.

5.1.3 Cationic Microgel Particles for Identification of Cancer Biomarkers

Cationic hydrogels with deformability similar to that of red blood cells were developed. Cationic red blood cell mimicking PRINT particles (CRBCMs) made from these deformable cationic polymers displayed the ability to bind to miRNAs in solution. Because the particles had been surface functionalized with a long chain PEG (20 kDa) to a negative overall zeta potential, it was clear that the miRNA had been internalized rather than surface

bound, potentially affording protection from endogenous nucleases. Initial tests using miRNAs associated with prostate cancer demonstrated the ability of the particles to tightly bind and responsively release the miRNAs. This strategy may enable the sequestration and identification of transiently available miRNA biomarkers of cancer.

5.2 Future Directions

5.2.1 Biodistribution Maps of Soft Particles

The discovery of deformability thresholds for RBC sized particles which allow for longer circulation times and altered biodistribution patterns opens up many opportunities for further study. With PRINT, we can fabricate monodisperse particle populations of any size and shape for which we can fabricate master templates with monodisperse features. Because master fabrication takes advantage of high-precision techniques first developed by the electronics and semi-conductor industries, an extremely high level of feature uniformity is possible for our master templates. As such, PRINT particles can be viewed as “calibration quality” when it comes to probing the interaction of particles with cells and other biological systems because of the uniformity of particle size and shape. Maps of biodistribution and pharmacokinetic behavior are highly desired for the field of nanomedicine, where rational particle design has the potential to greatly enhance the efficacy of a carried therapeutic.

With HP₃A hydrogels readily adaptable to smaller PRINT molds, an opportunity exists for plotting many points on these biodistribution maps with more highly deformable particles of different size and shape. The work carried out thus far has focused on low aspect ratio ($AR = 0.25-0.33$), deformable microparticles (**Figure 5.1**). However, these studies could readily extend to hydrogel PRINT particles on both the micro- and nanoscale

which are spherical analogs ($AR=1$) or high aspect ratio particles ($AR = 2 - 60$)²⁻⁵. Reduction of particle size to the typical range for nanoparticle therapeutics (100-200 nm) may be difficult due to the swelling of the hydrogels after molding, though master fabrication is constantly evolving and may produce a suitably small feature size in the future. Currently, PRINT templates with the smallest dimension of 80 nm are available with aspect ratios from about 1 to over 60⁵.

5.2.2 Methods for Determination of Particle Modulus

The moduli of deformable PRINT particles have, to this point, been inferred from the measured properties of bulk materials. Given that the bulk material has the same composition as particle, the mechanical properties should be very similar. However, properties of a bulk material may differ from those occurring at an interface, such as the interface of the material with air or with sides of the PRINT molds^{6,7}. While these surface effects are minimal for the case of a macroscopic sample where the vast majority of the material exists away from an interface, they may become significant on the particle size scale. The ratio of particle surface area to volume will increase as the size of the particle decreases, potentially making these surface effects relevant and changing the modulus of the particle with respect to that of the bulk material⁸.

Increasingly, attention has been given to the analysis of the mechanical properties of soft biological tissues, due in large part to the increase in the elasticity of cancer cells compared to benign cells⁹⁻¹¹. Significantly, metastatic cancer cells were found to be more than 70% softer than benign cells using AFM analysis, with elastic moduli on the order of 0.5 kPa⁹. Though a variety of methods exist for elastic analysis of cells¹⁰, atomic force

microscopy (AFM) may be the most readily accessible, most often used method, and most easily translatable to the analysis of particles. The elastic modulus of the cells is determined by pushing on the cell surface with the tip on the end of an AFM cantilever (**Figure 5.2**). The force applied is correlated with the movement of the cantilever during this interaction allowing for a calculation of the elastic (Young's) modulus of the cell¹². This method may be useful for the analysis of soft particles due to the precision with which low forces can be applied by AFM, and the wide availability of these instruments⁹.

The soft and slippery nature of hydrogels presents an area of possible difficulty in performing these measurements. The immobilization of cells or particles for measurement on a substrate is typically done through chemical bonding of the particle to the surface of a glass slide through chemical modification of the surface. Red blood cells, for example, can be attached to amine functionalized slides for AFM analysis by the application of glutaraldehyde solution which attaches the amines on the slide to amines on the membrane of the RBC¹. Similar methods for hydrogel particles may have the undesired side-effect of increasing the crosslink density of the hydrogel matrix on the surface, or in the bulk of the gel via diffusion of the reagent to the interior of the particle, thereby increasing the modulus of the particle. It may be possible to immobilize the hydrogel particles via electrostatic interaction with a charged surface, for example, a polylysine coated slide will be positively charged due to the amine residues, and may serve to immobilize acid-functional particles. An alternate strategy involves the use of track etched membranes affixed to a substrate with appropriately sized pores. Pores which are on the order of, or slightly larger than, the particles measured can serve to contain a hydrogel particle and keep it from moving while probing with the AFM cantilever¹³.

5.2.3 Hemoglobin Carriers for Oxygen Transport

5.2.3.1 Introduction to Blood Substitutes

The need for the development of a safe and efficacious substitute for donated blood has been well demonstrated. An ageing population and increase in the demand for selective surgery predicts a shortage of over four million units of donated blood by the year 2030¹⁴. Research and development into a blood substitute was underway as early as the 1930's, when Amberson *et al.* transfused animals with solutions of stroma free hemoglobin (Hb)¹⁵. While the unmodified Hb was found to be toxic, the modern search for a substitute for human blood was boosted by the outbreak of AIDS in the 1980's and the lack of the corresponding screening techniques which have since come into practice. Donated blood has a short shelf life (42 days) and requires cold storage, both factors that make stockpiling blood supplies impractical if not impossible. Concerns with storage, shelf-life, shortages, blood typing complications or delays, and infection by current and future pathogens are all motivations for the development of a safe and efficacious blood substitute.

5.2.3.2 Encapsulation of Hemoglobin for Oxygen Transport

While whole blood carries out many functions in the body, including gas transport, clotting action and immunological defense, blood substitutes are most commonly designed only to replace lost blood volume and for oxygen delivery. As such, "blood substitutes" are more properly called red cell substitutes or oxygen therapeutics. Modification of Hb, the protein responsible for oxygen transport in RBCs, is the most common strategy employed towards the fabrication of an oxygen transporter. Hb is a 68 kDa tetrameric protein with two

α and two β subunits, each with an iron containing heme, where each Hb tetramer is capable of binding four oxygen molecules. Inside the erythrocyte, 2,3-DPG binds to Hb, causing a conformational change which decreases the oxygen affinity and allows for more ready release of oxygen to tissue. Early isolations (1937) of Hb from human blood contained cytotoxin contaminated membrane stroma lipids which were found to have renal toxicity in animals ¹⁶. Highly purified stroma-free hemoglobin was prepared and used in trials, but remained toxic to the kidneys ¹⁷. Cell-free, the Hb tetramer degrades into $\alpha 1\beta 1$ and $\alpha 2\beta 2$ dimers which show renal toxicity upon their rapid clearance by, and accumulation in, the kidneys. These characteristics of renal toxicity and rapid splenic clearance of free Hb are the basis for the modification and encapsulation strategies employed by various proposed Hb based oxygen carriers (HBOCs) in the literature.

Strategies to avoid rapid clearance and toxic degradation products include modification of Hb by chemically crosslinking the subunits or tetramers^{14,18-22}, using recombinant DNA technology to fuse subunits together, conjugation of PEG or other polymers to the protein surface, encapsulation into liposomal carriers^{23,24} and embedding in polymeric particles^{25,26}. While the above modifications have proven sufficient to mediate the toxicity of the free tetramer, the modified Hb products still suffer from one or more problems which have kept them from obtaining regulatory approval²⁷.

The delicate nature of the PRINT process has allowed for the incorporation of sensitive biological cargos into PRINT particles, including RNA, pharmaceutical, and active proteins^{2,28}. To modify PRINT particles to carry and deliver oxygen, Hb and other allosteric effectors like 2,3-DPG and methemoglobin reductase can be included in the pre-particle formulation. The primary anticipated challenges include the possible denaturation of some

of the encapsulated Hb by the particle making process, difficulty in encapsulating erythrocyte like amounts of Hb (up to 33% by weight) while retaining hydrogel strength and deformability, and leakage of Hb from the particles leading to renal toxicity. While some amount of denaturation may be inevitable due to the UV curing process and the free radicals generated therein, the low temperature curing oven and laminator discussed in Chapter 2 may increase Hb stability. Cargo encapsulation at high weight percentages may significantly alter the physical properties of the particle matrix material, requiring reexamination of the relative component ratios to obtain suitable material properties.

Hemoglobin used for purposes of oxygen transport could be encapsulated inside of a hydrogel PRINT particle matrix. Via co-encapsulation of 2,3-DPG, and other enzymes such as catalase, superoxide dismutase, methemoglobin reductase and carbonic anhydrase the cooperative oxygen binding behavior of Hb in a native erythrocyte may be imitated. Enzymatic activity was retained with co-encapsulation of Hb with catalase and Hb with carbonic anhydrase inside synthetic membranes²⁹. The high surface area to volume ratio achieved through replication of the native RBC shape, and the inclusion of RBC enzymes should help to mimic the blood gas transport properties of RBCs. These properties can be evaluated by measuring the oxygen equilibrium curve (OEC), P_{50} and the cooperativity coefficient of the particles. These measurements can be obtained with the use of a Hemox analyzer (TCS Scientific Corp., New Hope, PA). The analyzer uses dual wavelength spectroscopy to measure the fraction of oxyhemoglobin and a Clark oxygen electrode to measure the partial pressure of oxygen. An oxyhemoglobin dissociation curve will be generated. The Adair equation, which models oxygen binding to the four binding sites of Hb, will be used to calculate the P_{50} and the cooperativity coefficient from the curve³⁰.

Due to the renal toxicity of free hemoglobin, assays to determine the encapsulation efficiency of Hb in the particles and to quantify any release of free Hb will be crucial in determining the viability of these particles.

5.2.4 Membranous Particles

5.2.4.1 Layer-by-layer Membranes

While the deformable hydrogel particles discussed in this dissertation demonstrated biologically relevant deformability, they are structurally quite different from the cells they are meant to mimic. Red blood cells are fluid-filled sacs contained by a complex membrane that has extreme flexibility originating from the membrane structure while our microgels are homogenous in structure. These two structures should behave quite differently in flow conditions, despite sharing similar mechanical properties^{31,32}. The use of layer-by-layer (LbL) assembly on a sacrificial template particle has the potential to reproduce a similar structure to the cell membrane. These hollow membranes, called LbL capsules, are formed by the deposition of complementary polymers in alternating layers onto colloidal particles, followed by removal of the original particle template³³. Complementary layers are most often formed from the sequential deposition of contrastingly charged polymers, with electrostatic forces driving the assembly, although hydrogen bonding, hydrophobic interactions and even DNA base pair hybridization have been used to drive the LbL assembly process³³. The properties of these capsules are considered to be readily tunable according to variations in the number of layers, the assembly conditions (such as pH or salt concentration) and the layer composition. Though little work has been done to maximize the elasticity of these capsules. Recently, Doshi et al. employed this strategy towards the fabrication of red

blood cell inspired microparticles using spherical polystyrene and PLGA templates and a variety of polyelectrolyte layers¹³. While these capsules were found to have a modulus an order of magnitude higher than that of red blood cells, dissolution of the template served to greatly reduce the modulus.

The use of PRINT particle templates for the fabrication of such LbL capsules represents a promising route to the development of monodisperse particle populations of deformable LbL capsules. Degradable or dissolvable materials such as PLGA³⁴, proteins²⁸ or degradable silyl-ether based monomers³⁵ are promising templates for these capsules which have been used previously in the PRINT process. A current effort in LbL assembly is directed towards the formation of colloidally stable LbL capsules with diameters of 500 nm or less³⁶. As much work has been done in fabrication 200 nm PRINT particles, this represents an appealing goal.

5.2.4.2 Hyaluronic Acid/Peptide Amphiphile Membranes

The self-assembly of small and large molecules into membranes with hierarchical order represents a more complex option that may also better mimic the actual structure of a cell membrane. Pioneered by the Stupp lab, hierarchically ordered membranes can form at an aqueous/aqueous interface with solutions of hyaluronic acid (HA) and positively charged peptide amphiphiles (PA)³⁷. Macroscopic sacs were formed from these solutions, with membrane formation forming several distinct, ordered domains. These sacs were mechanically robust and were able to “heal” when damaged. Additionally, it was found that they could be made permeable to proteins, which was novel for such robust membranes³⁷.

To replicate these self-assembled HA/PA membrane structures on the micron size-scale using PRINT, several strategies were employed. Initial attempts involved filling a PRINT mold with an aqueous solution of HA, then freezing the HA filled mold to a thick layer of PA solution (both components supplied by the Stupp lab). The peptide amphiphile used in these studies consisted of an alkyl tail of 16 carbons attached to the peptide sequence V₃A₃K₃. Procedures laid out by Capito et al. were followed in terms of HA and PA solution concentrations and pH³⁷, with membrane formation confirmed by the assembly of a macroscopic sac prior to application of the PRINT method. A small amount of fluorescein isothiocyanate labeled HA was included in the HA solution to facilitate imaging. The mold was peeled off the ice layer and the ice allowed to melt, with the intention of HA particles submerging into the melted PA to allow for membrane formation to succeed (**Figure 5.3**). This technique appeared promising initially, but closer inspection revealed the likely formation of unclosed sacs due to either evaporation of water from the HA solution or an incomplete submersion of the HA particles in the PA solution upon melting (**Figure 5.4**).

As a material for the fabrication of PRINT particles, HA is not ideal due to processing concerns. The HA solutions (96 kDa - 1.7 MDa) provided by the Stupp lab were quite viscous at concentrations higher than 5% for the lowest molecular weight, with the HA solution not completely de-wetting the mold surface (**Figure 5.5**). The aqueous solutions showed rapid evaporation of water at these low concentrations, despite the high viscosity, making mold-filling difficult, although the use of low temperature equipment and humidity control may serve to mediate such evaporation in future experiments. Attempts to lyophilize the HA-filled molds to yield porous HA scaffolds²⁸ was unsuccessful in producing such particles, likely due to the limited solubility of HA in water leading to insufficient solids

content to support such structures. Degrading before it melts, HA is not melt-processable³⁸ and could not be fabricated as solid particles.

Despite the difficulties in translating this technology to the PRINT technique, such assembled membranous structures remain a promising goal. The fabrication of such membranous particles may promote much more authentic, cell like *in vivo* behavior, enabling extremely long circulation times through improved avoidance of splenic accumulation. Such long circulating particles could have applications in drug delivery, for the slow release of drugs, thrombotic applications, or for carrying hemoglobin and delivering oxygen.

5.3 Figures

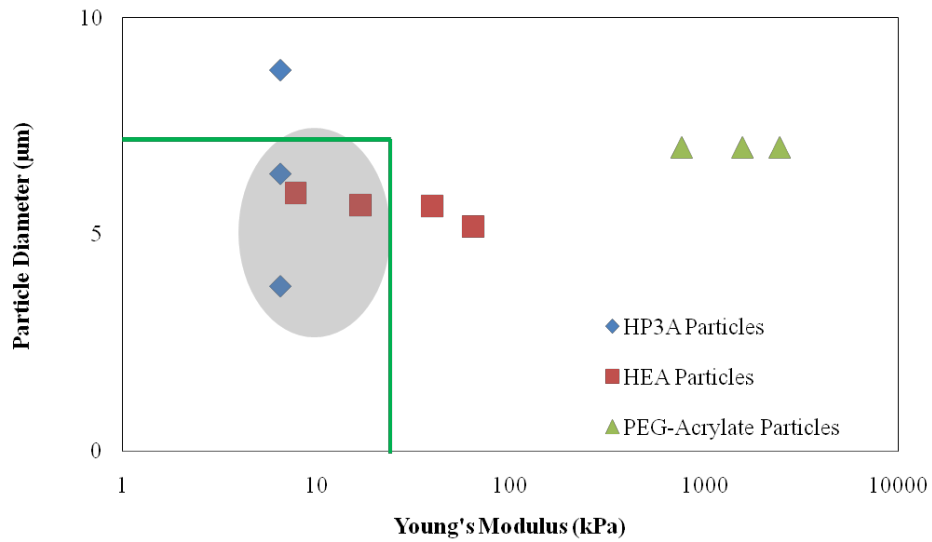


Figure 5.1. A plot showing the diameter and modulus of low aspect ratio particles examined in this dissertation. The grey oval indicates the particles which demonstrated longer circulation times as a result of avoidance of physical filtration mechanisms in the circulation. The green box indicates the combination of particle diameters and moduli which should be the target of future studies.

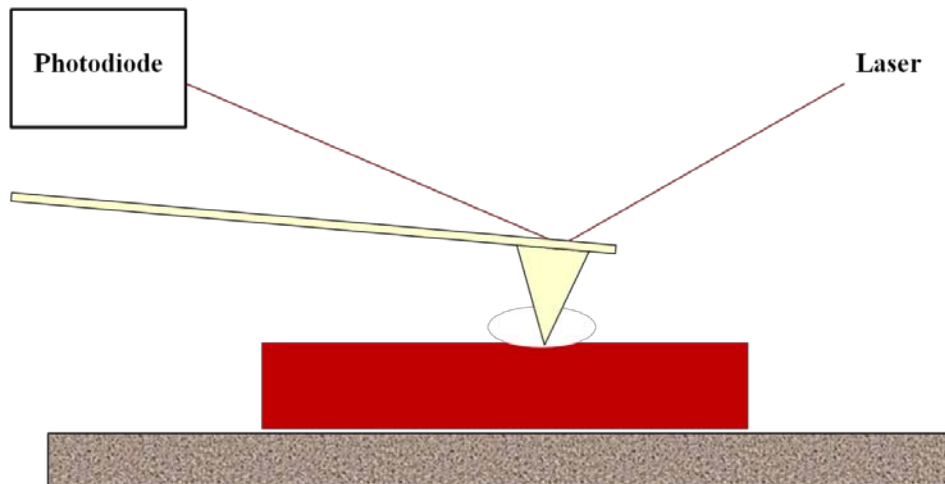


Figure 5.2. A schematic representation of atomic force microscopy (AFM) being used to probe the mechanical properties of a PRINT particle. A known force is applied by the AFM to the particle, causing a deformation in the particle. The movement of the cantilever is tracked by the movement of a laser on a photodiode detector as it reflects from the top of the cantilever. Deformations must be small relative to the thickness of the particle to avoid interference from the substrate.

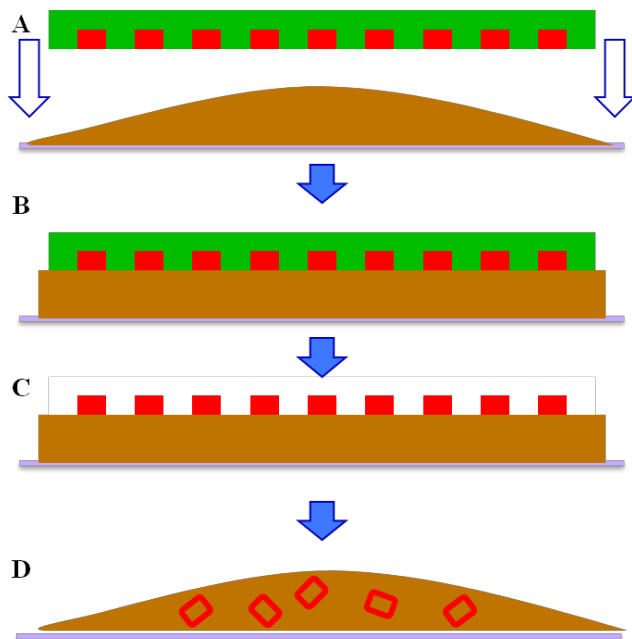


Figure 5.3. A schematic of the initial attempts at the fabrication of micron sized, self assembled HA/PA membranes. (A) A PRINT mold (green) is filled with HA solution (red) and frozen before bringing into contact with a layer of PA solution (brown). (B) The assembly is frozen on dry ice and, (C) the mold is peeled away, leaving the frozen HA particles on the PA ice surface. (D) The solutions thaw and the HA drops into the PA solution where membrane self-assembly occurs, yielding hollow sacs.

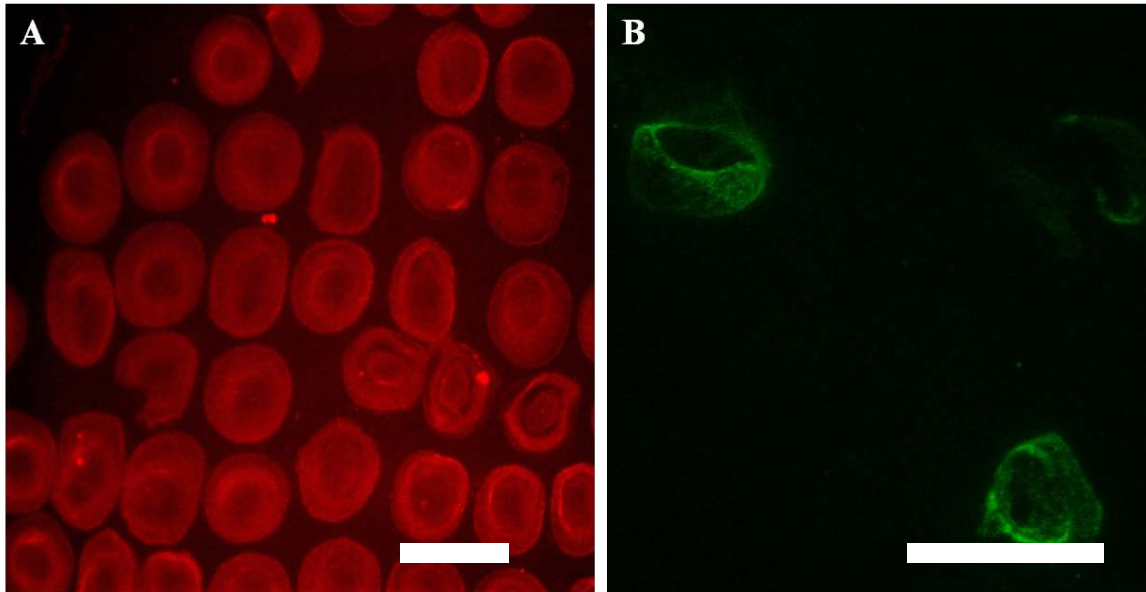


Figure 5.4. Membranes assembled from HA particles cast in $7 \times 7 \mu\text{m}$ cylinder PRINT molds and harvested to a solution of PA. (A) The particles appeared to assemble into fully formed sacs which were reminiscent of red blood cells. (B) Inspection with a confocal microscope showed that the sacs did not fully close, likely due to incomplete immersion of HA particles into the PA solution. Scale bars are $20 \mu\text{m}$.

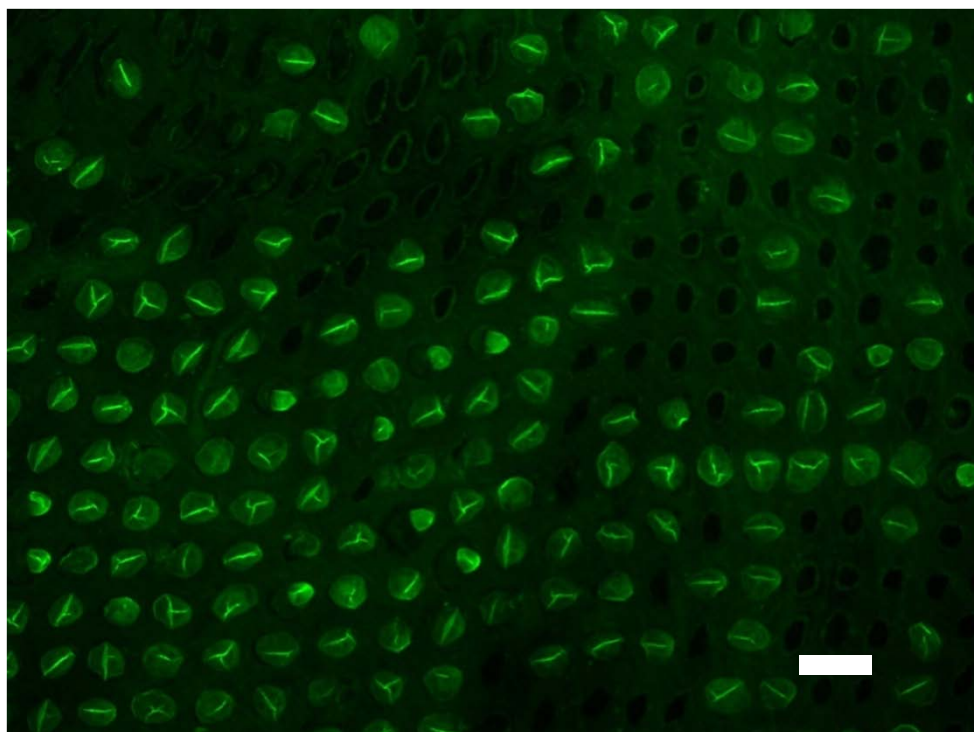


Figure 5.5. An image of sacs formed from assembly of HA and PA with a connecting scum layer resulting from incomplete de-wetting of the PRINT mold surface. The bottom left of the image contains collapsed sacs trapped in this scum layer, while the upper right side has more holes in this membrane. The scale bar represents 20 μm .

5.4 References

- (1) Dulinska, I.; Targosz, M.; Strojny, W.; Lekka, M.; Czuba, P.; Balwierz, W.; Szymonski, M. *J Biochem Biophys Methods* **2006**, *66*, 1.
- (2) Canelas, D. A.; Herlihy, K. P.; DeSimone, J. M. *Wiley Interdiscip Rev Nanomed Nanobiotechnol* **2009**, *1*, 391.
- (3) Gratton, S. E.; Pohlhaus, P. D.; Lee, J.; Guo, J.; Cho, M. J.; Desimone, J. M. *J Control Release* **2007**, *121*, 10.
- (4) Gratton, S. E.; Ropp, P. A.; Pohlhaus, P. D.; Luft, J. C.; Madden, V. J.; Napier, M. E.; DeSimone, J. M. *Proc Natl Acad Sci U S A* **2008**, *105*, 11613.
- (5) Merkel, T. J.; Herlihy, K. P.; Nunes, J.; Orgel, R. M.; Rolland, J. P.; DeSimone, J. M. *Langmuir* **2009**, *26*, 13086.
- (6) De Gennes, P. G. *Macromolecules* **1981**, *14*, 1637.
- (7) Chen, Z.; Shen, Y. R.; Somorja, G. A. *Annual Reviews of Physical Chemistry* **2002**, *53*, 437.
- (8) Kohane, D. S. *Biotechnol Bioeng* **2007**, *96*, 203.
- (9) Cross, S. E.; Jin, Y. S.; Rao, J.; Gimzewski, J. K. *Nat Nanotechnol* **2007**, *2*, 780.
- (10) Suresh, S. *Acta Biomater* **2007**, *3*, 413.
- (11) Suresh, S. *Nat Nanotechnol* **2007**, *2*, 748.
- (12) Butt, H.-J.; Cappella, B.; Kappl, M. *Surface Science Reports* **2005**, *59*, 1.
- (13) Doshi, N.; Zahr, A. S.; Bhaskar, S.; Lahann, J.; Mitragotri, S. *Proc Natl Acad Sci U S A* **2009**, *106*, 21495.
- (14) Arnoldo, B.; Minei, J. *Current Opinion in Critical Care* **2001**, *7*, 431.

- (15) Amberson, W. R., et al. *Journal of cellular and comparative physiology* **1934**, 5, 359.
- (16) Amberson, W. R. *Biological Reviews* **1937**, 12, 48.
- (17) Savitsky, J. P.; Doczi, J.; Black, J.; Arnold, J. D. *Clin Pharmacol Ther* **1978**, 23, 73.
- (18) *Blood Substitutes*; Winslow, R. M., Ed.; Elsevier: New York, 2006.
- (19) Henkel-Honke, T.; Oleck, M. *Aana J* **2007**, 75, 205.
- (20) Gould, S. A.; Moore, E. E.; Hoyt, D. B.; Ness, P. M.; Norris, E. J.; Carson, J. L.; Hides, G. A.; Freeman, I. H.; DeWoskin, R.; Moss, G. S. *J Am Coll Surg* **2002**, 195, 445.
- (21) Levy, J. H. *Expert Opin Biol Ther* **2003**, 3, 509.
- (22) Sprung, J.; Kindscher, J. D.; Wahr, J. A.; Levy, J. H.; Monk, T. G.; Moritz, M. W.; O'Hara, P. J. *Anesth Analg* **2002**, 94, 799.
- (23) Chauvierre, C.; Marden, M. C.; Vauthier, C.; Labarre, D.; Couvreur, P.; Leclerc, L. *Biomaterials* **2004**, 25, 3081.
- (24) Li, S.; Nickels, J.; Palmer, A. F. *Biomaterials* **2005**, 26, 3759.
- (25) Patton, J. N.; Palmer, A. F. *Biomacromolecules* **2005**, 6, 2204.
- (26) Patton, J. N.; Palmer, A. F. *Biomacromolecules* **2005**, 6, 414.
- (27) Alayash, A. I. *Clinics in laboratory medicine* **2010**, 30, 381.
- (28) Kelly, J. Y.; DeSimone, J. M. *J Am Chem Soc* **2008**, 130, 5438.
- (29) Chang, T. M. *J Intern Med* **2003**, 253, 527.
- (30) Voet, D. V., J.G. *Biochemistry, 2nd ed.* ; John Wiley & Sons: New York, 1995.

- (31) Haghgooie, R.; Toner, M.; Doyle, P. S. *Macromol. Rapid Commun.* **2009**, *31*, 128.
- (32) Li, J.; Lykotrafitis, G.; Dao, M.; Suresh, S. *Proc Natl Acad Sci U S A* **2007**, *104*, 4937.
- (33) Johnston, A. P. R.; Cortez, C.; Angelatos, A. S.; Caruso, F. *Current Opinion in Colloid & Interface Science* **2006**, *11*, 203.
- (34) Enlow, E. M.; Luft, J. C.; Napier, M. E.; DeSimone, J. M. *Nano Lett* **2011**, *11*, 808.
- (35) Parrott, M. C.; Luft, J. C.; Byrne, J. D.; Fain, J. H.; Napier, M. E.; Desimone, J. M. *J Am Chem Soc* **2010**, *132*, 17928.
- (36) Johnston, A. P. R.; Such, G. K.; Ng, S. L.; Caruso, F. *Current Opinion in Colloid & Interface Science, In Press, Corrected Proof*.
- (37) Capito, R. M.; Azevedo, H. S.; Velichko, Y. S.; Mata, A.; Stupp, S. I. *Science* **2008**, *319*, 1812.
- (38) Zhang, M.; James, S. P. *J Mater Sci Mater Med* **2005**, *16*, 587.